Technology Forces

Journal of Engineering and Sciences

ISSN 1994-862X (Print)
ISSN 2790-0053 (Electronic)

Volume 4 - Issue 1 | January - June 2022




KIET Research Projects

Karachi Institute of Economics & Technology

Technology Forces

Journal of Engineering and Sciences

College of Engineering

Karachi Institute of Economics & Technology

For queries on submissions, please send an email to mazher.iqbal@kiet.edu.pk

COLLEGE OF ENGINEERING

Vision

"To impart highest quality engineering education with an aim to produce proficient, creative and ethical electrical engineers who can take the role of visionary leaders, entrepreneurs and researchers at national and global levels".

Mission

"To educate students through highly qualified faculty to have strong theoretical and practical expertise, team-work, leadership qualities, ethical values and entrepreneurship skills. Establish and maintain state-of-the-art laboratories, latest curriculum and industrial linkages. Prepare graduates to pursue higher studies and undertake research at national and global levels".

AIMS AND SCOPE

Technology Forces Journal is a peer-reviewed journal that aims at the publication and dissemination of original research articles on the latest developments in all fields of engineering, science and technology. The journal publishes original papers in English which contribute to the understanding of engineering science and improvement of the engineering technology and education. Papers may be theoretical (including computational), experimental or both. The contribution should be unpublished before and not under consideration for publication elsewhere. Technology Forces Journal maintains a standard double-blind peer review process. The double-blind process means that the identity of the author and the reviewer are not known to each other.

Focused areas for publication include; but not limited to:

- Signal Processing
- Data Mining and Visual Analytics
- Software Engineering & Future Generation Computing
- Embedded Systems
- Smart Networks
- Molecular and Nanoelectronics
- Applied Controls and Power

OPEN ACCESS POLICY

For the benefit of authors and research community, this journal adopts open access policy, which means that the authors can self-archive their published articles on their own website or their institutional repositories. The readers can download or reuse any article free of charge for research, further study or any other non-profitable academic activity.

PEER REVIEW POLICY

Peer review is the process to uphold the quality and validity of the published articles. Technology Forces Journal uses double-blind peer review policy to ensure only high-quality publications are selected for the journal. Papers are referred to at least two experts as suggested by the editorial board. All publication decisions are made by the journal's Editors-in-Chief on the basis of the referees' reports. We expect our board of reviewing editors and reviewers to treat manuscripts as confidential material. The identities of the authors and reviewers remain confidential throughout the process.

COPYRIGHT

DISCLAIMER

The opinions expressed in **Technology Forces Journal** are those of the authors and contributors, and do not necessarily reflect those of the journal management, advisory board and the editorial board. Papers published in Technology Forces Journal are processed through double blind peer-review by subject specialists and language experts. Neither the **College of Engineering** and nor the editors of **Technology Forces Journal** can be held responsible for errors or any consequences arising from the use of information contained in this journal, instead; errors should be reported directly to the corresponding authors of the articles.

Table of Contents

MECHANICAL STRUCTURE OF AUTONOMOUS DELIVERY DRONE

Authors: Fahad Munib Khan[1], Saim Ahmed[1], Muhammad Ismail Mansoor[1], Muhammad Anas Bilal[1], Kazim Ali Sabzwari[1]
[1]Department of Mechatronics, SZABIST Karachi, Pakistan
Email: dr.saim@szabist.edu.pk (Saim Ahmed), fahadmunibkhan@gmail.com (Fahad Munib)

Received: 27-April-2021 / Revised: 14-June-2022 / Accepted: 17-June-2022
Karachi Institute of Economics and Technology || Technology Forces Journal, Volume 4, Issue 1, 2022

ABSTRACT

In this paper, the objective is to design a mechanical structure of drone (quadcopter) capable of carrying a 2-3 kg load in a 2-3 km radius around the pickup point and deliver it autonomously. Therefore, for designing the quadcopter, aerodynamics, stress and strain analyses have been considered in simulations and then hardware has been designed accordingly. This paper focuses in particular on the mechanical design of quadcopter using SolidWorks and the components required for this concept to be brought into reality.

Keywords: Drone, Autonomous delivery, Solid Works.

1. INTRODUCTION

Unmanned aerial vehicle (UAV) known as drone [1], drones around the world are symbolized as the future of all forms of technology, whether it is used as a means of transport for goods or people [2] or by the military to carry out strikes and reconnaissance [3]. The sheer control that we possess over the drones allows us to save key resources such as fossil fuels and human lives that can be utilized to make the world a better place.

Various companies across the world have made drones that can be set to follow a target while responding to their surroundings, gesture control drones for theatrics, autonomous delivery drones such as the ones brought into use by only amazon so far, drones ranging from the size of 10-year old's palm to bigger than a Toyota than people can mount and ride[4]. Moreover, several companies have taking initiative to create racing first-person view (FPV) [5] drones and made a sport out of it, racing drones in patterns and through obstacles.

Drone technology is often classified by generations, the first generation being basic manual control and each generation improving on the previous, adding imaging/video taking, more aerodynamic designs, autonomous flight, safety features and spatial sensors. The continuous growth in this technology will make it safer to use in public areas and push it further into mass production. Drone laws in some countries are quite strict, but as safety features improve, we should see some relaxation on that front as well [6].

The use of drones in autonomous deliveries is of particular interest to us as we see it as the ideal form of item delivery in the future, as it should be able to reduce energy wastage and unnecessary human labour which could be directed elsewhere to improve efficiency and environmental friendliness [7]. The drone we intend to fabricate will deliver items within a limited area, but the technology can be applied to drones with larger fuel capacities for longer distances. Alternatively, if it were possible to set up several recharge points in strategic locations, the range of deliveries can be improved. The uses of these sorts of drones include healthcare emergency drones carrying vital first aid equipment, improving economies through the 'last mile' (last stretch of a journey a product makes) and reducing pollution, since drones can be powered by green technology [8].

In order to maximise efficiency, it is necessary for drones to have minimal mass while maintaining structural strength, so they are often made using carbon fibre and light metals like aluminium, therefore similar materials have been used for the proposed design. The proposed design is used with the base and arms cut from carbon fibre and the connections made with aluminium to increase joint strength. The testing of the proposed model is performed in the 3D modelling software SolidWorks to find weak points and make sure nothing is above the yield strength of the material for each part.

The main contributions are as follows:

- Optimized mechanical design of delivery drone (quadcopter).
- Aerodynamics, stress and strain analyses have been done in SolidWorks.
- The proposed structure is capable of carrying 2-3kg with a servo-controlled claw.

1.1 Literature Review

Drones, particularly autonomous drones initially designed for military use [9] and gradually adapted toward private and consumer needs [10]. Nowadays they are mainly used in every aspect of life ranging from catastrophe situations [11] to recreational purposes [12], in the agriculture sector for monitoring crop's health [13], in an inspection of building rooftops or bridges [14] saving both human effort and time. Use of this equipment can also be included in the transportation of goods or items delivery [15] considering its potential to save fuel and manual labor that can be spent more efficiently to improve industries output. Additionally, low altitude air traffic is not currently a problem, making it ideal for quick transport. One issue that can arise from this, is to have multiple charging points across the city instead of expanding battery sizes. Since having a greater battery size will increase costs and weight. By using an automatic charging station, drone technology can overcome limitations like long distances easily.

Most of the existing research, explored in this paper, revolves around the chassis of the drone where different anomalous shapes were configured and tested in hexacopter or quadcopter variations. Some studies concluded that if a drone is to carry an extra object, it must be aerodynamically efficient to minimize air-wash under the drone chassis and the landing procedure for an autonomous drone shouldn't be dependent on one response system, e.g., just telemetry, instead, it should encompass telemetry, optical feedback [16], laser guidance and a gyro for precision as it operates depends on three axes [17].

In [18], the author explores the special stabilization and autonomous landing of a drone using vision-based landing pad recognition. For this purpose, a method was developed which allows a drone to estimate its relative position and orientation through computer vision, after placing a predefined marker/set of markers on the landing area. This paper was limited by physical hardware, as the experiments were performed in a controlled ROS simulation, and thus do not account for random errors such as wind and limited lighting.

C. Rajukar et al. [19] attempt to solve the problem of package security, suggesting two-way communication with the drone along with a GPS to allow it to change its drop-off point in case of unforeseen changes, and a servo-operated combination lock to guarantee that the package can only be opened by the intended recipient. A mobile app to control the drop-off point is proposed as well. The primary issue explored was the lack of security in the current drone delivery systems, specifically how packages are dropped without confirming the presence of the customer, the lack of an option to change the drop-off point, and the lack of measures to prevent against people who are not the customer picking up the package. The researchers were limited by 2D GPS as it does not take into account building heights – using 3D GPS would allow for much more efficient flight path planning. The second limitation was the size and weight of the goods.

An article by Kornatowski et al. [20], describes a drone design that could improve drone flight safety for humans and other animals. Instead of using low-density blade covers which tend to have large holes that humans' extremities may slip through, they suggest making a cage with a tennis racket-like net and having the propellers shrink into it when near humans. They also take into account the increasing global interest in drones as a form of quick, cheap, and efficient transport that can access otherwise difficult-to-reach locations. According to the authors, most contemporary alternatives are limited by the requirements of flat, empty landing areas and landing pads, but the new morphing drone design should be able to deliver in populated areas with fewer requirements of the surroundings. The authors were limited by the production cost and materials available to them. They suggested strengthening the enclosure frames using carbon, aluminum, or titanium alloys, and reducing the frame weight by replacing the plastic grids with larger modules.

The work presented by Abhinav Ajay et al. [21] explores a method of improving drone safety using a transforming frame, this time looking to aspects of Japanese origami for inspiration. Origami is known to be capable of creating shapes that have considerable strength when folded in particular ways, which can be very useful in many fields. The author mainly wanted to discuss issues of safety when flying multirotor drones in populated environments. They recognize the importance of drones in the modern e-commerce and emergency supply industry and desire to give their input on how to improve them in terms of cargo drones. The author designed and made an origami cage for his drone, and tested it in normal flight conditions. They also designed a servo-based dropping mechanism for the package that is activated through an OTP-based system.

K. Nonami [22] in his work proposed guidance, navigation, and control (GNC) of the current standard drone and how it can be improved for beyond visual line of sight (BVLOS) flight. The author deemed that BVLOS technology could revolutionize the logistics industry as well as support disaster relief societies. The limitations of their research included the government's laws on the autonomous flight, such as an autonomous drone having to be below a specific weight to be able to fly in a metropole city, and a license being required to operate such a vehicle.

2. METHODOLOGY

This section presents the mechanical structure, flow chart, and calculations of the proposed design.

2.1 Mechanical Structure

The drone parts were designed and tested in Solidworks. Carbon fibre and fibre glass is selected to use for the arms and base plate, because they are one of the best materials available for flying vehicles, able to withstand high stresses while being very lightweight. They are also relatively easily available in our region, and viable in terms of costs for a one-off project [23]. The air flow analysis around propeller, initial structure and final prototype design are given in Fig. 1-3, respectively.

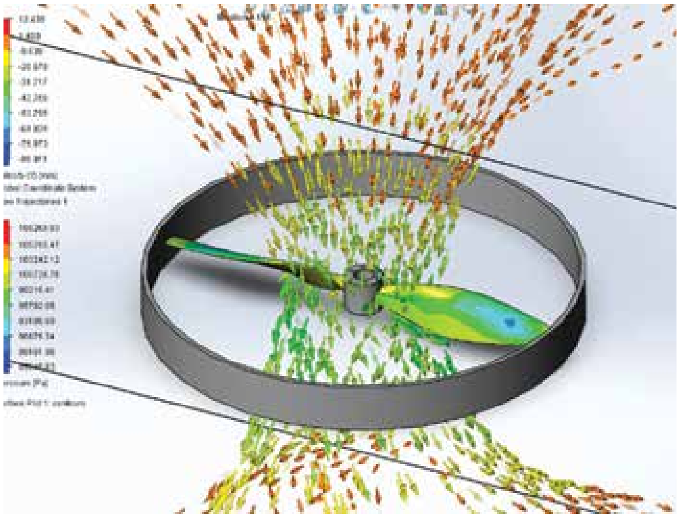

Figure 1: Air flow around propeller

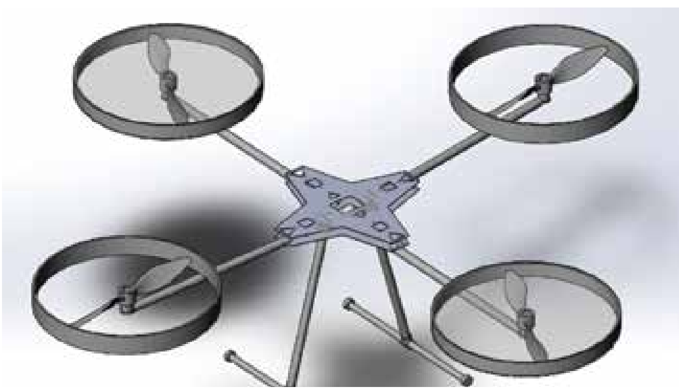

Figure 2: Initial drone design

Figure 3: Final drone design

2.2 Flight Calculations (Prototype)

1045 props, 3S LiPo 3200 mAh
maximum thrust, flight time:

$$F = Pull * g = 0.642 * 9.8 = 6.2916\ N\ per\ motor$$

$$Q = i * t$$

$$t = \frac{Q}{i} = \frac{3.2Ah}{9.5 * 4A} * 60 = 5.0526\ minutes$$

$$F\_total = 6.3 * 4 = 25.2N$$

$$Prototype\ weight\ \approx 1.42 * 9.81 \approx 13.93N$$

2.3 Flight Calculations (Consummate):

Drone mass≈8.5kg;

Motor Thrust $= 2 * Load = 2 * \frac{8.5}{4} = 4.25kg$

ESC Current Rating $= \frac{P_{motor}}{V} = \frac{1750}{22.2} = 78.83A$

∴ 80A is sufficient

Prop rating: 18x6 (experimentally found)

2.4 Battery Calculations (Consummate):

$$\frac{1750W}{22.2V} = 78.8288A$$

$$15\ minutes = 0.25h$$

$$78.8288A * 0.25h = 19.7072Ah$$

$$78.8288A * 4 = 315.3152A\ total$$

$$22000mAh\ available$$

$$\frac{315.3152A}{22Ah} = 14.3325\ h^{-1}\ minimum$$

2.5 Flow chart

The basic flight control of the proposed method has been given in Fig. 4.

Nonlinear Dynamic models and control systems have been developed and reviewed by many researchers [24-25], with altitude control being possible with a simple PID controller [26]. Flight control software has been used and adding to it for our purposes, including the addition of control for a claw to hold a box containing the package to be delivered.

According to the sources, 6-12s batteries would be ideal for proposed design, with matching speed controllers and motors that can withstand high voltages, to reduce wire currents. Lower currents reduce losses due to heat and allow us to use thinner wires, which also helps reduce weight, along with heating losses.

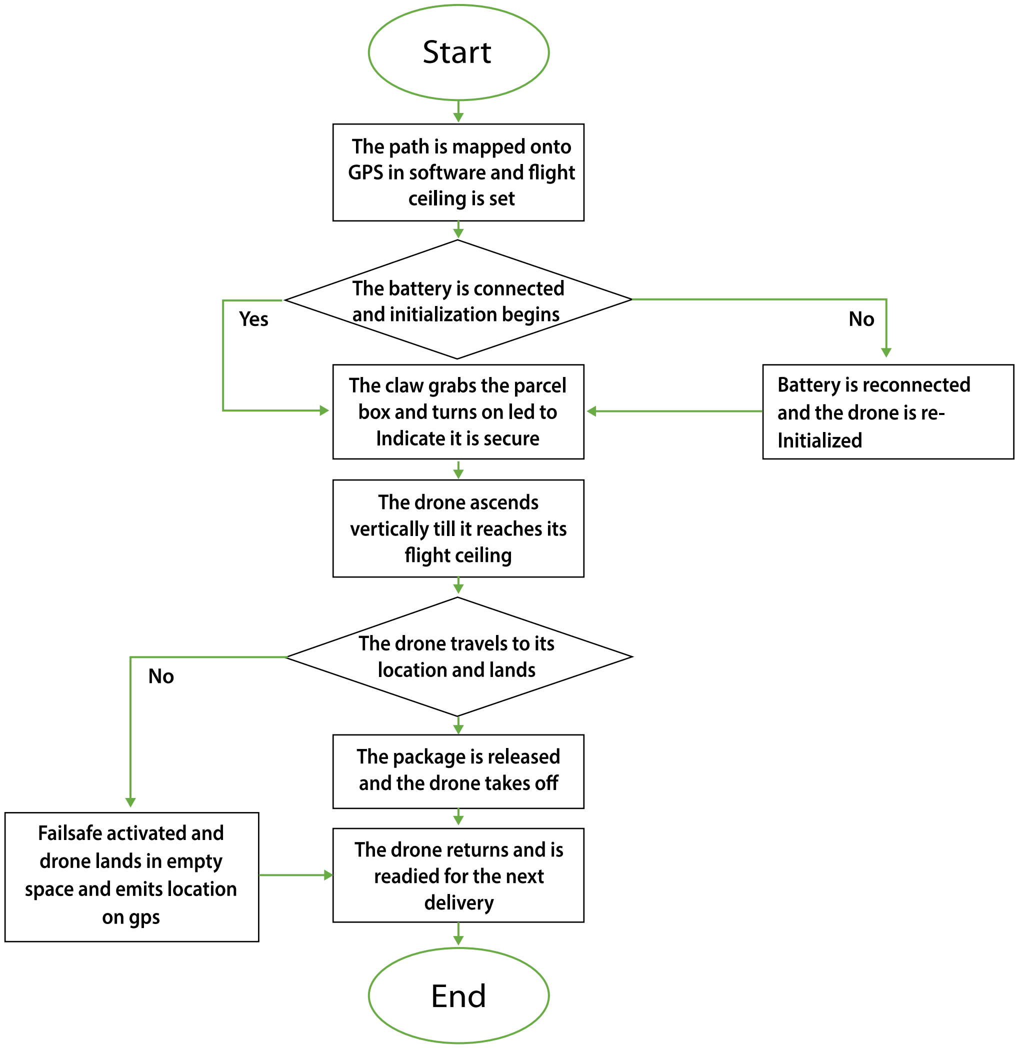

Figure 4: Flow chart of proposed model

3. RESULTS

In this section, stress and strain analyses of the proposed design are shown using Soliworks. The results of the stress analyses showed no issues with the parts at the specified loading conditions (total drone + package mass: 8.5kg). Maximum stress in the arms and base plate are a large margin below yield strengths of the materials. The stress and strain analyses are shown in Fig. 5-7.

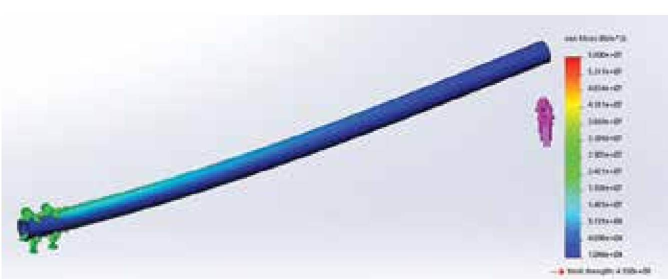

Figure 5: Stress test of arm

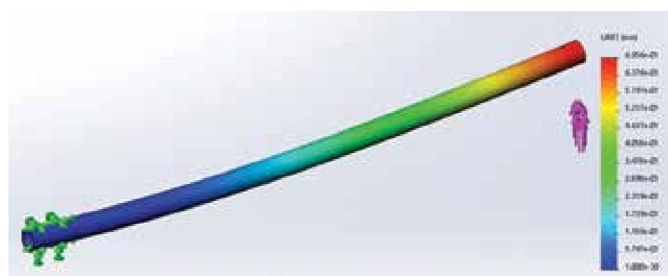

Figure 6: Strain test of arm

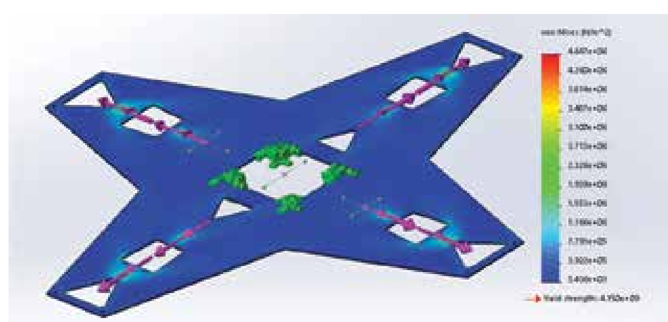

Figure 7: Stress test of base plate

Now, the different claw designs are tested to hold the package are shown in Fig. 8-10.

Figure 8: Claw design 1

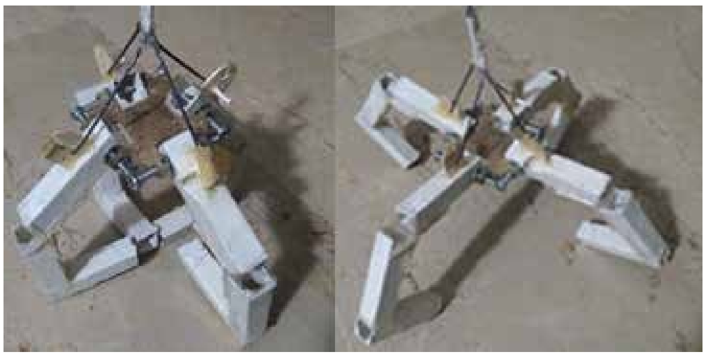

Figure 9: Claw design 2

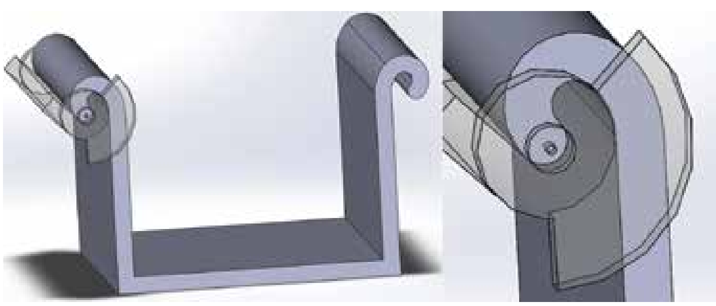

Figure 10: Claw design 3

Above are three conceptual ideas for mechanical claws to hold the package in place. Design 1 is made using sticks and it is the basic design to check the stability, Design 2 has the largest range of motion which makes it easier to implement but less stable due to the long, thin parts. Design 3 attempts to simplify the task to two servo motors and reduce the movement range, while preventing the box from moving from side to side.

The final design will be a combination of Claw Design 2 and Claw Design 3, with further improvements that make it more suitable for a specific box size and more stable during flight.

4. CONCLUSION

In this paper, we designed a quadrotor UAV for package delivery purposes. Our drone's mechanical design performed very well in simulations; however, it may be possible to optimise it for better aerodynamics, and the consummate drone with high-power electronics has yet to see in-flight testing

As the world continues to make progress in this field and computer engineering therefore the foreseeable future of drones is filled with artificial intelligence and more size and battery efficiency. An Unmanned Aerial Vehicle will be used in all fields of life from emergency services to military utilisation and more civil employment, we plan to continue down the same path and use image feedback as a form of input to the FLC, along with integrating SMC (slide mode control) into the FLC which will allow the drone to manoeuvre to a safe position in case a sensor or actuator fails. SMC allows the FLC to input pulses to the motor which causes them to work in short bursts allowing the drone to bounce across the air, in a manner referred to as 'sliding' in one direction on any two axes. We plan to incorporate a lighter and smaller claw improving the overall efficiency of the drone and allowing more weight to be transported.

REFERENCES

[1] H. Yao, R. Qin, and X. Chen, “Unmanned aerial vehicle for remote sensing applications—A review,” Remote Sens., vol. 11, no. 12, p. 1443, 2019.

[2] F. Outay, H. A. Mengash, and M. Adnan, “Applications of unmanned aerial vehicle (UAV) in road safety, traffic and highway infrastructure management: Recent advances and challenges,” Transp. Res. part A policy Pract., vol. 141, pp. 116–129, 2020.

[3] N. Sharkey, “The automation and proliferation of military drones and the protection of civilians,” Law, Innov. Technol., vol. 3, no. 2, pp. 229–240, 2011.

[4] “Amazon.com:” https://www.amazon.com/Amazon-Prime-Air/b?ie=UTF8&node=8037720011 (accessed Jun. 10, 2022).

[5] J. Delmerico, T. Cieslewski, H. Rebecq, M. Faessler, and D. Scaramuzza, “Are we ready for autonomous drone racing? the UZH-FPV drone racing dataset,” International Conference on Robotics and Automation (ICRA), 2019, pp. 6713–6719.

[6] “Future of Drones: Applications & Uses of Drone Technology in 2021.” https://www.businessinsider.com/drone-technology-uses-applications (accessed Jun. 10, 2022).

[7] “Daily Drone Deliveries Surpass 2,000 Globally - Practical Ecommerce.” https://www.practicalecommerce.com/daily-drone-deliveries-surpass-2000-globally (accessed Jun. 10, 2022).

[8] “The Current State of Drone Delivery Worldwide.” https://mydroneauthority.com/industry/drone-delivery/ (accessed Jun. 10, 2022).

[9] S. Chaudhary, A. Prava, N. Nidhi, and V. Nath, “Design of all-terrain rover quadcopter for military engineering services,” in Nanoelectronics, Circuits and Communication Systems, Springer, 2019, pp. 507–513.

[10] R. A. Krishnan, V. R. Jisha, and K. Gokulnath, “Path planning of an autonomous quadcopter based delivery system,” International Conference on Emerging Trends and Innovations In Engineering And Technological Research, 2018, pp. 1–5.

[11] A. Asaduzzaman, A. Telakapalli, and F. N. Sibai, “Smart Disaster Management Using Software-Defined Unmanned Aerial Systems,” Annual Consumer Communications & Networking Conference (CCNC), 2021, pp. 1–2.

[12] S. J. Kim, Y. Jeong, S. Park, K. Ryu, and G. Oh, “A survey of drone use for entertainment and AVR (augmented and virtual reality),” in Augmented reality and virtual reality, Springer, 2018, pp. 339–352.

[13] S. Ahirwar, R. Swarnkar, S. Bhukya, and G. Namwade, “Application of drone in agriculture,” Int. J. Curr. Microbiol. Appl. Sci., vol. 8, no. 01, pp. 2500–2505, 2019.

[14] J. A. Besada et al., “Drone mission definition and implementation for automated infrastructure inspection using airborne sensors,” Sensors, vol. 18, no. 4, p. 1170, 2018.

[15] F. Li, Y. Zhong, L. I. Zhixiong, J. Zhu, and C. Qian, “A Design of Autonomous Goods Transport System Based on Quadcopter,” Conference on Electrical, Computer Engineering and Electronics, 2015, pp. 1601–1609.

[16] S. Ahmed, I. Mansoor, "H_infinity Model Reference Adaptive Control for Robot Manipulators". Technology Forces Journal of Engineering and Sciences, 2021, 3(2), pp. 44-52.

[17] M. I. Mansoor and M. B. Kadri, “Evaluating different Kinematic Models of Mobile robots using Linear and Non-linear controls,” Int. Bhurban Conf. Appl. Sci. Technol. IBCAST 2021, pp. 560–567, 2021, doi: 10.1109/IBCAST51254.2021.9393242.

[18] T. G. Carreira, “Quadcopter automatic landing on a docking station,” Inst. Super. Técnico, 2013.

[19] C. Rajurkar, “‘ Unmanned Secured Delivery System ’ International Journal on recent,” vol. 4, no. 9, 2016.

[20] P. M. Kornatowski, M. Feroskhan, W. J. Stewart, and D. Floreano, “A morphing cargo drone for safe flight in proximity of humans,” IEEE Robot. Autom. Lett., vol. 5, no. 3, pp. 4233–4240, 2020.

[21] A. Ajay, J. Amal Prakash, S. Gokul, S. Aji, and P. R. Prabhu, “Origami Based Cargo Drone,” J. Electron. Des. Eng., vol. 5, no. 3.

[22] K. Nonami, “Present state and future prospect of autonomous control technology for industrial drones,” IEEJ Trans. Electr. Electron. Eng., vol. 15, no. 1, pp. 6–11, 2020.

[23] N. K. Pradhan, R. Nehra, and others, “Challenge and advantage of materials in design and fabrication of composite UAV,” in IOP Conference Series: Materials Science and Engineering, 2018, vol. 455, no. 1, p. 12005.

[24] Ahmed, S., Wang, H., & Tian, Y. "Fault tolerant control using fractional-order terminal sliding mode control for robotic manipulators". Studies in Informatics and Control, 2018, 27(1), 55-64.

[25] S. Ahmed, H. Wang, Y. Tian, , July. Modification to model reference adaptive control of 5-link exoskeleton with gravity compensation. Chinese Control Conference, 2016, pp: 6115-6120.

[26] M. Z. Mustapa, “Altitude controller design for quadcopter UAV,” J. Teknol., vol. 74, no. 1, 2015.

MAGNETOIMPEDANCE HYSTERESIS EFFECTS IN AMORPHOUS GLASS-COATED MICROWIRES FOR EMBEDDED SENSING APPLICATIONS

Authors: Azim Uddin[1] , Maqsud Nematov[2] and Mohamed Salem[3]
[1]Institute for Composites Science Innovation (InCSI), School of Materials Science and Engineering, Zhejiang University, 38 Zheda Road, Hangzhou, 310027, PR. China
[2]National University of Science and Technology MISiS, Leninskii pr. 4, Moscow, 119049 Russia
[3]Physics Department, Faculty of Science, Tanta University, Tanta 31527, Egypt

Received: 11-May-2022 / Revised: 14-June-2022 / Accepted: 30-June-2022
Karachi Institute of Economics and Technology || Technology Forces Journal, Volume 4, Issue 1, 2022

ABSTRACT

During the last two decades, ferromagnetic materials have appealed much attention due to their lenient magnetic properties and enhanced electrical resistivity, which is helpful to implement in various industrial sensing applications. Recently, amorphous glass-coated microwires have become available, combining mild magnetic properties with specific magnetic anisotropy. The magnetic hysteresis loops and magnetoimpedance effects in C-rich microwires covered with glass have been investigated in the present work. This largely depends on the sign of the magnetostriction saturation. Such behaviors were demonstrated in wires of the identical composition Co71Fe5B11Si10Cr3 but with dissimilar geometric properties. Depending on the easy anisotropy direction, the wire can exhibit such unique properties as magnetic bistability (magnetization changes abruptly between the two stable states), wall propagation, and giant magnetoimpedance. Furthermore, the wires can be further subjected to internal tensile stress to realize stress-sensitive magnetostriction, which can be proposed in embedded sensing sensors.

Keywords: Ferromagnetic microwires; Taylor-Ulitovsky method; Magnetoimpedance effects; Embedded stress sensors.

1. INTRODUCTION

Over the past few decades, the field of magnetism has changed our understanding tremendously due to its remarkable properties. Previously, scientists used to study and characterize soft magnetic materials to adjust the effectiveness of their magnetic attributes and the cost. However, the modern society of soft magnetic materials has recently taken us in a new direction towards the advancement in the field of applied physics, technologies, material sciences, and much more [1-4]. Therefore, thin wires from modern magnetic materials have received all the attention, and amorphous ferro-magnetic type glass-coated microwires are one of them. These microwires got more attention because of their reduced geometrical dimensions, enhanced soft magnetic properties, giant magneto-impedance (GMI) impact, Barkhausen impact (LBE), and other excellent properties [5-6]. Previously, ferromagnetic microwires were prepared by various methods. For example, I.S. Miroshnitchenko accompanying I.V. Salli produced the first metallic glass nearly 50 years ago by swift stimulating from the liquid state and later by P. Duwez et al. [1], [7]. But amorphous glass-coated microwires have a unique place in the modern world. The Amorphous glass-coated microwires are obtained by the Tailor-Ulitovsky procedure available in a range of metallic diameters from 1- 20 mm, which cannot be obtained using the old quenching method due to the high surface energy of the liquid metal [8-9]. In the Taylor technique, latterly known as the microwire process or Taylor-wire, different metals and alloys have been used to produce a variety of microwires with core diameters for various applications. This technique is relatively inexpensive compared with other old methods, therefore, it received more attention in making these wires.

Especially in-embedded sensing procedure/method, some special fillers are required, which can behave as mediators between the internal factors/parameters of the given medium as well as a readout device. Based on the physical attributes of this transitional function, different quantities, physically, can be achieved as the measurement factors, which include: complex permittivity, voltage, impedance, current, and resistance and electric-magnetic fields [10-12]. Therefore, conducting a comparative analysis of microwires' magnetic properties and MI effects with different geometrical configurations would be beneficial and can be used in embedded sensing applications.

Developing wireless magnetic sensing materials with small size and improved performance are progressively critical for several applications, especially embedded sensors. Therefore, we need to investigate of magnetic properties of micron-sized amorphous ferromagnetic wires to tackle this problem. The present work studies the magnetic hysteresis (M-H) loops and magnetoimpedance (MI) effects of the same chemical composition alloy glass-coated microwires. Particular prominence is given to seeing the impact of dissimilar geometrical configurations on their properties. Furthermore, the correlation between magnetic hysteresis (M-H) loops and magnetoimpedance (MI) results is discussed. The wire sample composition is taken as Co71Fe5B11Si10Cr3 with two different geometries having total wire diameters of sample No. (1): 41.5 microns and sample No. (2): 29.5 microns ensuring small and positive magnetostriction. Our conducted experiments are premeditated not only to determine the effect of the physical properties of microwires but also to address the direct relation of wires' geometrical relationship with the sensitivity that is related to the embedded sensors.

2. MATERIALS AND EXPERIMENTAL DETAILS

2.1 Fabrication of Amorphous Glass-coated Microwires

The most recent fabrication procedure to fabricate glass-coated microwires is the Modern Taylor-Ulitovsky method [13-14]. The wires made by this technique usually have a uniform coating of insulating glass attached closely to the metallic core [7]. The good thing about this technique is that it allows controlling the microstructure and the geometrical structure of the wires. Through this, according to required applications, we can easily regulate the size, such as the nucleus diameter and/or the glass coating thickness.

In the present investigation, the amorphous glass-coated microwires are manufactured through a modern Taylor–Ulitovsky method [13]. This technique is based on the direct casting of wires from the melting of alloy, as schematically shown in Figure 1. First, a limited grams of quantity for master alloy with the anticipated composition, i.e., $Co_{71}Fe_5B_{11}Si_{10}Cr_3$ are placed into a Pyrex-like glass tube and located within a high-frequency inductor heater. Next, the alloy is heated up to its melting point to let it form a droplet. While the metal melts forcing the portion of the glass tube which is adjacent to the melting metal, to soften, enveloping the metal droplet. Finally, a glass capillary is drawn carefully from the softened glass portion and wound on a rotating coil, as shown in Fig. 1. At appropriate drawing conditions, a microwire is thus formed where a glass shell completely coats the metal core. Thus, microwires with two different diameters were fabricated and their detailed configurations are provided in Table 1.

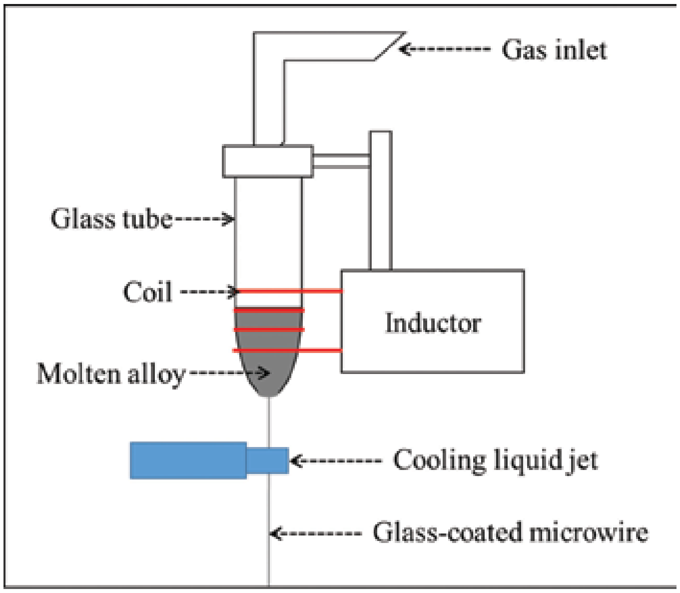

Figure 1: Schematic diagram of fabrication of glass-coated microwires by Taylor-Ulitovsky method.

However, in the production methodology of these wires, some components are often generated, such as internal stress with radial, axial or circular [2], [15], [16]. This is because they are developed inside the metallic part of the wire, and these factors arose due to the different quenching rates. These rates lie between the microwires' central region and the upper surface layer. Moreover, the induced stress in the prepared microwires is generated due to the alteration in their thermal expansion coefficients, which can be either due to the metallic nucleus or the glass layer. This effect plays a vital role in microwires [1], [17].

2.2 Characterizations

A field emanation scanning electron microscope (SEM, Hitachi) was employed to observe the morphologies of the as-prepared microwires. Amorphous ferromagnetic microwires are generally influenced by the magnetostriction coefficient, s, and by the strength of internal stress, ρ, which are generated by glass-coating influenced by the ρ -ratio of the diameter of the metallic core, d, to the total diameter of microwire, D ($\rho = d/D$). The experimental magnetization arcs were obtained by an inductive methodology with a set of two differential coils. The magnetization coils were agitated by a current of 500 Hz producing a magnetizing field having an amplitude of 1000 A/m. The persuaded voltage vs time was alphanumerically integrated to acquire a hysteresis loop. The short-cut wire was then inserted into a slender detection coil with an internal diameter of 3 mm and a span of 5 mm.

The magnetoimpedance effects in the wires are demonstrated with the help of Vector Network Analyzer (Model: Hewlett-Packard 8753E) for frequencies ranging from 1-100 MHz by measuring the S21/S12-parameters having forward transmission coefficient for specially designed microwave stripe-cell with a microwire. First, we placed a single piece of microwire having a length of 6 mm in a specially developed microstrip sample holder, which is placed within an extended solenoid that produces a homogeneous magnetic field to the range up to 15 KA/m alongside the micro-wire axis. Then, we determined the longitudinal impedance $Z_{\phi z}$ using VNA from the reflection transmission coefficient S22/S11 measurement, and the off-diagonal impedance dignified from the S12/S21 as a voltage is induced in a pick-up coil of 2 mm long wounded over a microwire.

3. RESULTS AND DISCUSSION

3.1 Morphology, Compositional Characteristics of Microwire Samples

The particulars of the chemical composition and geometric dimensions of the premeditated microwires are offered in Table 1. Two different types are used to study their magnetic and MI properties.

Table 1: The as-prepared microwire's composition with their inner and outer diameters.

Alloy Composition	Inner Diameter (µm)	Outer Diameter (µm)
$Co_{71}Fe_5B_{11}Si_{10}Cr_3$	36.5 microns	41.5 microns
$Co_{71}Fe_5B_{11}Si_{10}Cr_3$	23.9 microns	29.5 microns

To examine the surface morphologies of the as-prepared microwires, the wires were subjected to chemical etching by the diluted hydrofluoric (HF) acid solution to dissolve the glass layer. As a result, the surface of the as-prepared wires (Fig. 2(a-d)) exhibits some in-homogeneities instigated by the interaction between the metallic nucleus and glass layer throughout the casting process [18-19]. In addition, thermally induced surface defects for both wire samples can be observed probably due to heating inhomogeneity during the casting process. However, microwires, in general, recollect their integrity after fabricating. The hysteresis loops

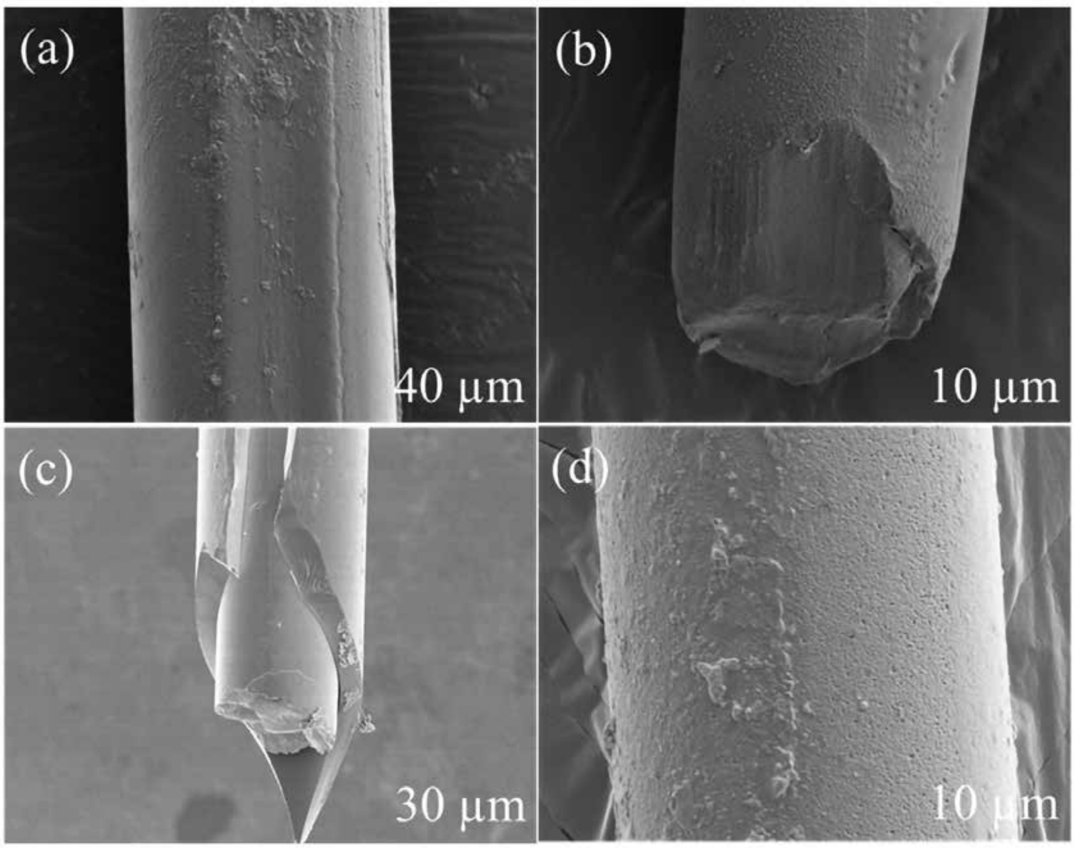

Figure 2: SEM images of the Co71Fe5B11Si10Cr3 microwires with different inner and outer diameters, i.e., (a, b) 36.5 microns and 41.5 microns; and (c, d) 23.9 microns and 29.5 microns, respectively.

3.2 Hysteresis Loop of as-prepared Wires

Amorphous glass-coated microwires of $Co_{71}Fe_5B_{11}Si_{10}Cr_3$ chemical composition with a slight positive magnetostriction constant of the order of 10-7 have been studied. Two types of wires with different structural geometrical parameters were used, labeled as sample No. (1) and Samples No. (2), as discussed in detail in Table 1.

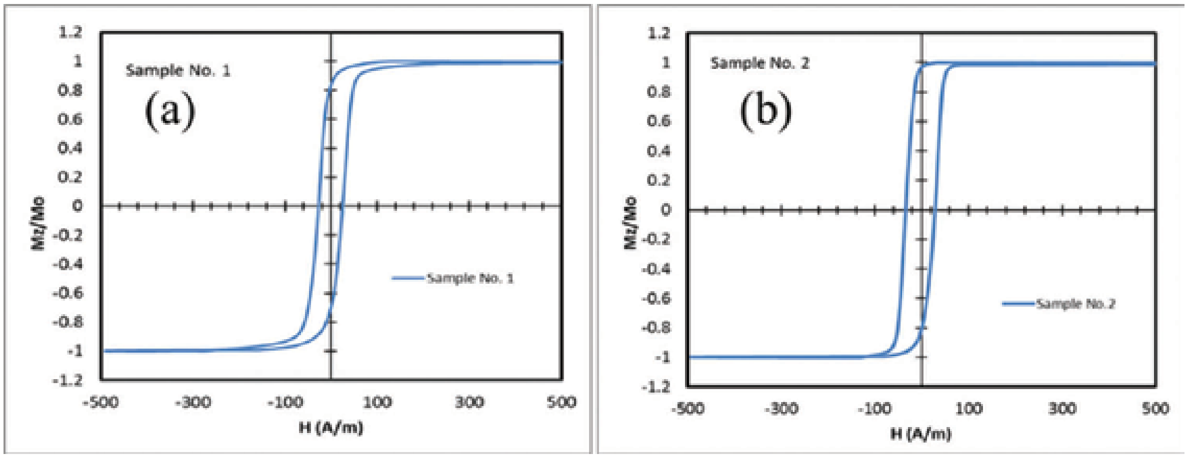

Figure 3: Experimental hysteresis loops for $Co_{71}Fe_5B_{11}Si_{10}Cr_3$ microwires with different diameters i.e., (a) 41.5 μm and (b) 29.5 μm, respectively.

are almost identical for both types of wires, with a small coercitivity of about 25 A/m, as shown in Fig. 3(a, b). However, the hysteresis loop for the wire with a smaller diameter (Sample No. (2)) has a more pronounced bi-stable behavior. In addition, the remanence value close to the saturation also confirms the existence of the axial anisotropy almost in the entire wire.

3.3 Magneto-impedance (MI) effect behavior of as-prepared Microwires

Comparing the behavior of MI in both types of wire samples is interesting since this can give a complete view of the characteristics of changing the anisotropy. Fig. 4(a, b) demonstrate that the MI effect is consistent with the impedance plots, which have a single maximum at zero external fields. Such behavior of MI is typical of materials with an easy anisotropy axis parallel to the magnetic field and excitation current [20]. Furthermore, both wire samples have MI characteristics with one central peak, as shown in Fig. 4(a, b), which also indicates the presence of an axial magnetic field [21-23]. However, the sample of a smaller diameter, i.e., Sample No. (2), has a more sensitive MI with a sensitivity of about 4.5 % per A/m at 100 MHz. In contrast, the MI sensitivity in the second wire is 1.7% per A/m.

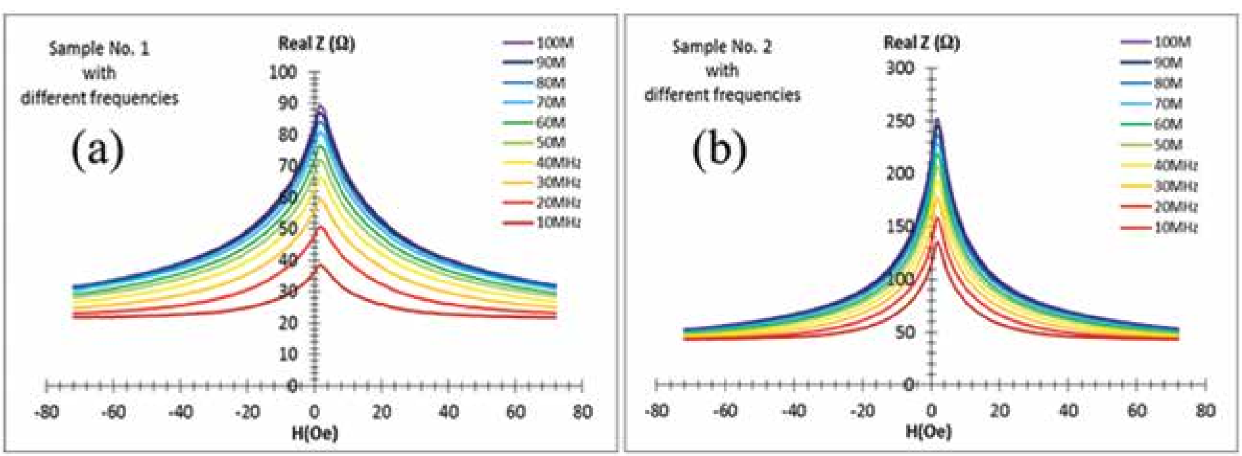

Figure 4: Real part of impedance vs. magnetic field at different frequencies for as-prepared wires with different diameters, i.e., (a) 41.5 μm and (b) 29.5 μm, respectively.

This property resembles the giant magnetoresistance (GMR). It is used for designing sensitive magnetic sensors for shallow magnetic field detection and can be used as embedded sensors, which operate at GHz frequencies [10]. In this case, the primary factor determining the sensitivity is related to the interplay of the wire's dimensions, the chemical composition, and reduced anisotropy [20], [24]. Therefore, the effects in wires observed can be promising for designing miniature built-in embedded sensors.

4. CONCLUSION

In this work, we fabricate the slightly positive magnetostrictive amorphous glass-coated microwires for stress-sensitive embedded sensor applications. We investigated the magnetic hysteresis loops and magnetoimpedance processes in two different types of wires of the same composition $Co_{71}Fe_5B_{11}Si_{10}Cr_3$, with different geometries. We demonstrated that sample No. (2) has a more sensitive MI with a sensitivity of about 4.5 % per A/m at 100 MHz, whereas the MI sensitivity in sample No. (1) is 1.7% per A/m. The sensitivity of the MI effect due to the difference in geometries is proposed to utilize in embedded sensors. Thus, Samples No. (2) can be used in sensing applications. Furthermore, the stress sensitivity of the ratio of harmonics amplitude could also be proposed for practical use to avoid the need for calibration. However, further investigations are carried out to explore new innovative lines for amorphous glass-coated microwires.

ACKNOWLEDGMENTS

The authors also thank Dr. V. Larin, MFTI Ltd (http://www.microwires.com) for donating the wire samples.

REFERENCES

[1] A. Zhukov, "Novel Functional Magnetic Materials," Springer Ser. Mater. Sci., vol. 231, pp. 1–446, 2017.

[2] M. Vázquez and A. Hernando, “A soft magnetic wire for sensor applications,” J. Phys. D. Appl. Phys., vol. 29, no. 4, pp. 939–949, 1996.

[3] H. García-Miquel, M. J. Esbrí, J. M. Andreés, J. M. García, J. M. García-Beneytez, and M. Vázquez, “Power absorption and ferromagnetic resonance in Co-rich metallic glasses,” IEEE Trans. Magn., vol. 37, no. 1, pp. 561–564, 2001.

[4] J. B. Pendry, A. J. Holden, D. J. Robbins, and W. J. Stewart, "Magnetism from conductors and enhanced nonlinear phenomena," IEEE Trans. Microw. Theory Tech., vol. 47, no. 11, pp. 2075–2084, 1999.

[5] X. Wang, R.-W. Li, C. Chang, A. He, Q. Man, and D. Estévez, “Magnetoinductance and magnetoimpedance response of Co-based multi-wire arrays,” J. Magn. Magn. Mater., vol. 393, pp. 278–283, 2015.

[6] V. Zhukova, M. Ipatov, J. González, J. M. Blanco, and A. P. Zhukov, "Development of thin microwires with enhanced magnetic softness and GMI," IEEE Trans. Magn., vol. 44, no. 11 PART 2, pp. 3958–3961, 2008.

[7] H. Chiriac and T. A. Óvári, Amorphous glass-covered magnetic wires: Preparation, properties, applications, vol. 40, no. 5. Progress in Materials Science, 1996.

[8] A. Zhukov et al., "Correlation of crystalline structure with magnetic and transport properties of glass-coated microwires," Crystals, vol. 7, no. 2, 2017.

[9] V. Zhukova, J. M. Blanco, M. Ipatov, M. Churyukanova, S. Taskaev, and A. Zhukov, "Tailoring of magnetoimpedance effect and magnetic softness of Fe-rich glass-coated microwires by stress-annealing," Sci. Rep., vol. 8, no. 1, pp. 1–14, 2018.

[10] D. Makhnovskiy, V. Zamorovskii, and J. Summerscales, "Embedded ferromagnetic microwires for monitoring tensile stress in polymeric materials," Compos. Part A Appl. Sci. Manuf., vol. 61, pp. 216–223, 2014.

[11] J. Olivera, M. González, J. V. Fuente, R. Varga, A. Zhukov, and J. J. Anaya, "An embedded stress sensor for concrete SHM based on amorphous ferromagnetic microwires," Sensors (Switzerland), vol. 14, no. 11, pp. 19963–19978, 2014.

[12] A. Allue et al., "Smart composites with embedded magnetic microwire inclusions allowing non-contact stresses and temperature monitoring," Compos. Part A Appl. Sci. Manuf., vol. 120, no. January, pp. 12–20, 2019.

[13] V. S. Larin, A. V Torcunov, A. Zhukov, M. Vazquez, and L. Panina, "Preparation and properties of glass-coated microwires," J. Magn. Magn. Mater., vol. 249, pp. 39–45, 2002.

[14] H. Chiriac, "Preparation and characterization of glass covered magnetic wires," Mater. Sci. Eng. A, vol. 304–306, no. 1–2, pp. 166–171, May 2001.

[15] P. Klein, R. Varga, G. Infante, and M. Vázquez, "Ferromagnetic resonance study of FeCoMoB microwires during devitrification process," J. Appl. Phys., vol. 111, no. 5, 2012.

[16] M. G. Nematov et al., "Effect of Mechanical Stresses and Annealing on the Magnetic Structure and the Magnetic Impedance of Amorphous CoFeSiBCr Microwires," Phys. Solid State, vol. 60, no. 2, pp. 328–333, 2018.

[17] I. Liberal, I. S. Nefedov, I. Ederra, R. Gonzalo, and S. A. Tretyakov, "Electromagnetic response and homogenization of grids of ferromagnetic microwires," J. Appl. Phys., vol. 110, no. 064909, pp. 1–8, 2011.

[18] M. Vázquez, H. Chiriac, A. Zhukov, L. Panina, and T. Uchiyama, "On the state-of-the-art in magnetic microwires and expected trends for scientific and technological studies," Phys. Status Solidi Appl. Mater. Sci., vol. 208, no. 3, pp. 493–501, 2011.

[19] H. Lu, V. Zhukova, M. Ipatov, A. Zhukov, W. Wan, and Y. Shen, "Surface defect detection of magnetic microwires by miniature rotatable robot inside SEM," AIP Adv., vol. 6, no. 9, p. 095309, 2016.

[20] A. Uddin et al., "Temperature Effects on the Magnetization and Magnetoimpedance in Ferromagnetic Glass-Covered microwires," in Journal of Physics: Conference Series, 2017, pp. 1–5.

[21] L. Li, M. Zhang, Q. Liao, W. Xia, and X. Ding, "Smart Composites With Short Ferromagnetic Microwires for Microwave Applications Composites With Short Ferromagnetic Microwires for Microwave Applications," IEEE Trans. Magn., vol. 531, no. 10, pp. 18–22, 2012.

[22] L. V. Panina, M. Ipatov, V. Zhukova, A. Zhukov, and J. Gonzalez, "Magnetic field effects in artificial dielectrics with arrays of magnetic wires at microwaves," J. Appl. Phys., vol. 109, no. 5, 2011.

[23] M. M. Salem, M. G. Nematov, A. Uddin, L. V. Panina, M. N. Churyukanova, and A. T. Marchenko, "CoFe-microwires with stress-dependent magnetostriction as embedded sensing elements," J. Phys. Conf. Ser., vol. 903, no. 1, pp. 1–4, 2017.

[24] M. H. Phan and H. X. Peng, "Giant magnetoimpedance materials: Fundamentals and applications," Prog. Mater. Sci., vol. 53, no. 2, pp. 323–420, 2008.

FUZZY COOPERATIVE CONTROL FOR MULTIPLE MOBILE ROBOTS

Authors: Salman Zaffar[1], Hussain Aftab[1]

[1]DHA Suffa University
Karachi, Pakistan, salmanfar@gmail.com (Salman Zaffar), hussain.aftab@gmail.com (Hussain Aftab),

Received: 22-June-2022 / Revised: 05-July-2022 / Accepted: 05-July-2022
Karachi Institute of Economics and Technology || Technology Forces Journal, Volume 4, Issue 1, 2022

ABSTRACT

This work focuses on the formation control for a team of mobile robots. Path following and cooperation seems an easy task from a human point of view, however for a robot it requires complex control algorithms. Therefore to mimic the human way of thinking, the proposed control algorithm is based on fuzzy logic which closely matches the human thought process. Hierarchal control architecture is used with two levels of controllers which are fuzzy and proportional integral and derivative (PID) based controllers. Fuzzy controller is the high level controller and it perform two tasks, path following and cooperation between robots, whereas the PID controller is responsible for the accurate tracking of speed for the robot wheel motors. Every robot has its own path that is pre-determined by the trajectory planner, as the robot move along their respective path the control algorithm adjust their linear and angular velocities such that they move in formation and reach their destinations at same time regardless of the length and curvature of path. The proposed control scheme is implemented on simulation and the results are obtained.

Keywords: Fuzzy Cooperative Control, Mobile Robots.

1. INTRODUCTION

Formation control of multi mobile robots has been a topic of interest for past several years. A lot of research is being done on how to effectively control multiple mobile robots (MMR) to perform a collective task. The idea of formation control is universal and applies to almost all kinds of robots. For example, a fleet of autonomous air vehicles use the formation control algorithms to test the aerodynamics of such vehicles. Control of Multi mobile robots have a vast range of applications such as unmanned air vehicles [1 –3], autonomous ground vehicles [4-5], mine sweepers [6] etc.

The primary motivation of using multi mobile robots is to improve the overall effectiveness of the system. MMRs can easily perform difficult task which a single robot or a team of independent (Non – Cooperative) robots cannot perform such as to carry a heavy object. Furthermore, MMRs are cost effective in comparison of building one powerful robot several; identical small robots are much more cost effective and efficient.

Cooperative control of mobile robot is a challenging task, in this problem the robots are subjected to both path following and formation maintaining constraints. The idea of real time path following and formation control seems easy for humans, but for a robot it is a difficult task specially to decide between the individual and group goals.

The idea is to make such a model which can perform individual robot path following simultaneously maintaining an inter robot formation. The objective is that the robots should be able to follow their respective paths as well as maintain an inter robot formation. The robots may have different paths with different lengths and curvatures still the robots should track their path, maintain formation and reach the target at the same time regardless of the path length and their initial position.

The goal was to make use of the human thought process for the cooperative behavior for this purpose several things needs to be considered. The robot should be able to track the path and send its location to the controller; therefore the robot must have localized feedback. Several approaches are being used for localization of a robot in its environment [7-9].

To achieve cooperation between robots three different models were studied to test their performance and applications.

- Behavior based model
- Leader follower method
- Virtual structure

In behavior based model the robot consist of several behaviors, each of which is responsible for a specific situation [10-12]. The problem with this type of model is that it does not support decomposition of task or the modeling of sub task. Furthermore it difficult to achieve precise cooperative control as it is mathematical analysis is difficult.

In the leader follower method one of the robots is the leader and the others are the followers [13]. In this scheme the leader is the one which responsible for the formation, all other robots are supposed to follow the leader and maintain a certain distance (relative position) from the leader. The disadvantage of this scheme is that there is no feedback available from the follower robots and hence if anyone of them encounters an obstacle then it is difficult to keep up with the formation.

In virtual structure approach the system consider the team of mobile robots as a rigid structure (virtual structure) [14-15]. This approach is easier to implement as it all the robots are part of virtual structure hence the cooperation is easier, but it can be also a point of failure.

Due to its simplicity and ease of implementation the virtual structure approach was selected. However, to compensate for the weakness of this method a more streamlined control architecture was required.

Background research for the control algorithm reveals that the control algorithm used for cooperative control of mobile robots are based on Nonlinear Control techniques which often require complex mathematical equations to be implemented, which are difficult to be realized in a microcontroller environment, therefore Fuzzy control was selected as it mimics human logic and it is easier to implement and it has fast decision making process which makes it an ideal candidate for multiple mobile robots scenario.

The model used in this thesis is based on the virtual structure with a fuzzy controller. There has been a lot of work being done artificial intelligence for path following of mobile robots. The fore study of path following techniques tells that Neural Network and Fuzzy Logic Controllers are commonly used for path following of mobile robots for both “Known” and “unknown” environments [16-19]. There are researches which exploited both these techniques also known as neurofuzzy controllers [20-21]. However, most of these researches were carried out on single mobile robots but with a little modification these can be implemented in a cooperative control environment.

It was decided to implement a Hierarchal Control structure in which there are two different hierarchies namely High level Fuzzy Controller and Low Level PID controller. The Fuzzy Controller is the main controller which is responsible for the cooperation, path following and localization of robots. While Low level controller is a PID controller which is responsible for the speed tracking for each of the robot's wheel motor.

The organization of this paper is as follows, section 2 presents the modeling of a differential drive robot along with the system constraints. Section 3 presents the control architecture, defines the cooperative control problem and discuss in detail the fuzzy cooperative controller. In section 4 simulation results are presented and section 5 concludes the paper.

2. MODELING OF DIFFERENTIAL DRIVE ROBOT

The kinematic model of a differential drive robot is given in(1). Where $v(t)$ is the linear velocity and $\omega(t)$ is the angular velocity of the robot while $\varphi(t)$ is the orientation of the robot.$v(t)$ and $\omega(t)$ are the control variables.

$$\begin{cases} \dot{x}(t) = v(t)\cos\varphi(t) \\ \dot{y}(t) = v(t)\sin\varphi(t) \\ \dot{\varphi}(t) = \omega(t) \end{cases} \qquad (1)$$

Fig. 1 shows a differential drive robot with two wheels mounted on a common axis. If the wheels are rotating considering there is no lateral slip then there exist a point ICC (instantaneous center of curvature) provided that ($v_r \neq v_l$). Where v_r and v_l are the linear velocities of the right and left wheels respectively. By varying v_r and v_l we can change the ICC and hence we can control the movement of the robot. R is the distance from the ICC to the center of the two wheels which is also considered as the center of the robot. L is the distance between the two wheels. And θ is the orientation of the robot from x axis.

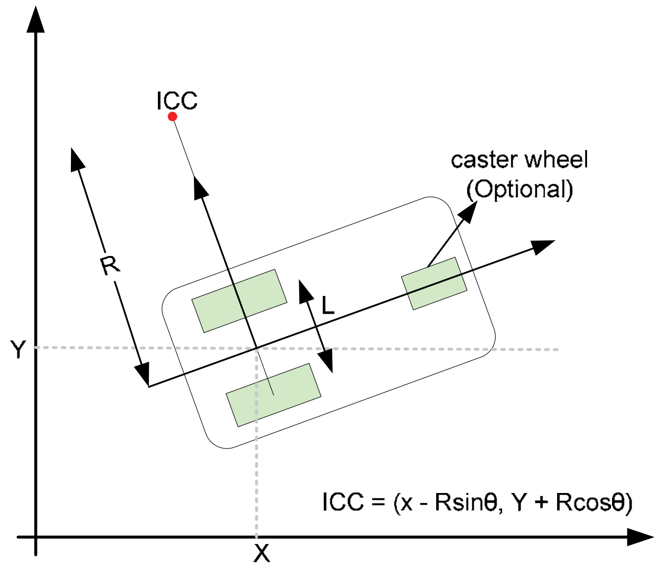

Figure 1: Differential drive mobile robot

We can write the equation for v_r and v_l using the relationship $v = R\omega$.

$$v_r = (R + \tfrac{L}{2})\omega$$
$$v_l = (R - \tfrac{L}{2})\omega \qquad (2)$$

Solving (2) for R and ω and using the relation $v = R\omega$ we get the following relations.

$$\omega = \frac{(v_r - v_l)}{L}$$
$$v = \frac{(v_r + v_l)}{2} \qquad (3)$$

To obtain v_r and v_l in terms of v and ω we can rewrite (3) as follows.

$$v_r = \frac{(2v + \omega L)}{2}$$
$$v_l = \frac{(2v - \omega L)}{2} \qquad (4)$$

Thus the mathematical model of the differential drive robot can be implemented by using(1), (3) and(4).

The differential drive robot is subject to nonholonomic constraints such as it cannot move lateral along is axel. This can be mathematically written as.

$$\dot{x}\sin\theta - \dot{y}\cos\theta = 0 \qquad (5)$$

Similarly the robot's linear and angular velocities are also bounded by the following constraints.

$$|v(t)| \leq v_{\max} \qquad |\omega(t)| \leq \omega_{\max}$$
$$|\dot{v}(t)| \leq \dot{v}_{\max} \qquad |\dot{\omega}(t)| \leq \dot{\omega}_{\max} \qquad (6)$$

3. COOPERATIVE CONTROL STRUCTURE

Fig. 2 shows the control structure. The proposed scheme comprises of two level of control namely.

- High level fuzzy cooperative controller
- Low level PID controller

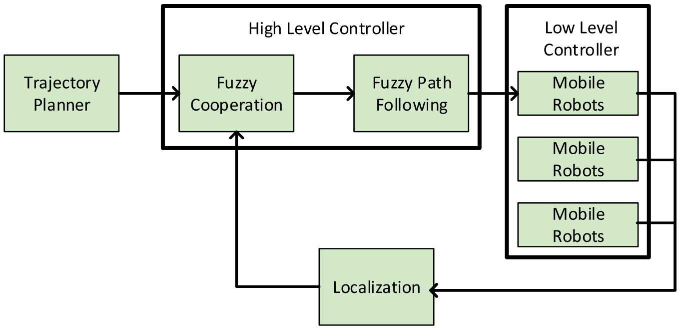

Figure 2: Control structure

The trajectory generator is responsible for generating paths for the robots, which is the reference for fuzzy controller. The output of fuzzy controller is used as a reference for low level PID controller. The low level controller is responsible for accurate tracking of robot's left and right wheel motors whereas fuzzy controller is responsible for path following of individual robot as well as cooperation between robots. Feedback is collected from robot's wheel motors in the form of speed and then a localization algorithm is used to locate each robot's position and orientation which is then sent back to fuzzy controller.

3.1 High Level Fuzzy Control

The High Level Fuzzy Controller is a Takagi sugeno type fuzzy controller which is responsible for path following of individual mobile robots as well as group cooperation between robots. The defuzzification scheme used in the fuzzy controller is weighted average. Fig. 3 shows the Fuzzy Control structure.

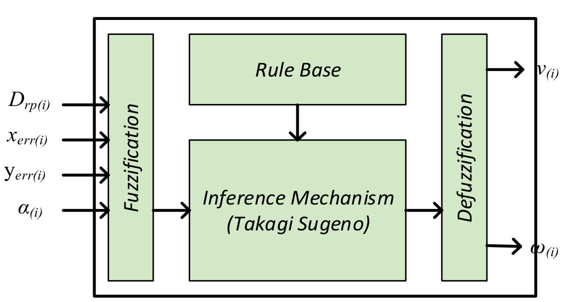

Figure 3: Fuzzy control structure

Refer to Fig. 4: $i = 1, \dots, k$ is the robot number. The position and orientation of the robot can be described by the vector $P_i = [x_i, y_i, \varphi_i]^T$.The path to be followed by robots is divided into n discrete set of points, where $n = 0, \dots, f$. Each point on the path can be described by the vector $Q_{di(n)} = [x_{di(n)}, y_{di(n)}, \xi_{di(n)}]^T$. Where $Q_{di(0)}$ being starting point of the path and $Q_{di(f)}$ being the final point. Whereas $Q_{di(n)}$ represent the nth sample point on the path.

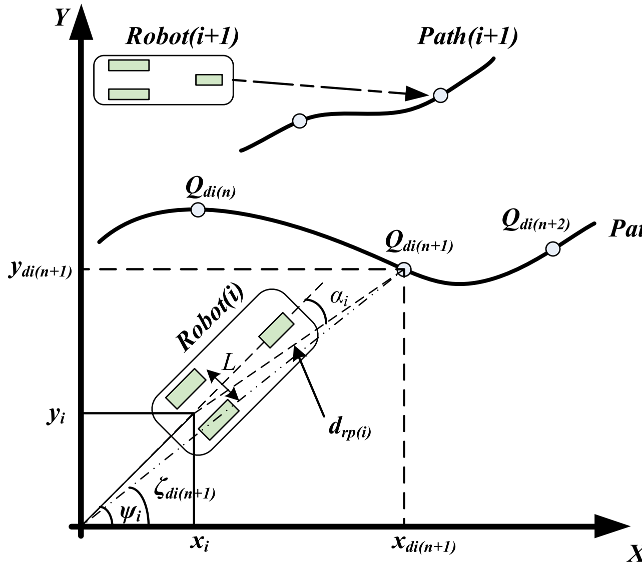

Figure 4: Robot path following parameter

The Inputs to the Fuzzy Controller are $D_{rp(i)}$, $x_{err(i)}$, $y_{err(i)}$ and $\alpha_{(i)}$. Where

- ☐ $D_{rp(i)}$ is the distance of the actual position of the ith robot from its next desired point on the path.
- ☐ $x_{err(i)}$ is the error of the ith robot's position the X direction.
- ☐ $y_{err(i)}$ is the error of the ith robot's position in the Y direction.
- ☐ $\alpha_{(i)}$ is the error in orientation of ith robot from the next desired point.

$D_{rp(i)}$ is calculated using the distance formula as shown in the following equation.

$$D_{rp(i)} = \sqrt{(x_{di} - x_i)^2 + (y_{di} - y_i)^2} \qquad (7)$$

Where x_{di}, y_{di} are the coordinates of the next desired point on the path while x_i, y_i are the coordinates of the actual position of the robot.

$x_{err(i)}, y_{err(i)}$ and $\alpha_{(i)}$ are in the robot's reference frame and are calculated from the following equation.

$$\begin{bmatrix} x_{err(i)} \\ y_{err(i)} \\ \alpha_{(i)} \end{bmatrix} = \begin{bmatrix} \cos\varphi_{(i)} & \sin\varphi_{(i)} & 0 \\ -\sin\varphi_{(i)} & \cos\varphi_{(i)} & 0 \\ 0 & 0 & 1 \end{bmatrix} \begin{bmatrix} x_{di} - x_i \\ y_{di} - y_i \\ \zeta_{di} - \varphi_i \end{bmatrix} \quad (8)$$

Where φ_i is the robots orientation which is adjusted to $\pm\pi$ radians. ζ_{di} is the orientation of the next desired point which can be calculated via using the following equation.

$$\zeta_{di} = tan^{-1}\left(\frac{y_{di}-y_i}{x_{di}-x_i}\right) \quad (9)$$

The Fuzzy controller generates the required linear and angular velocities v_i, ω_i of the robot. The output of the fuzzy controller is used as a set point the low level PID controller.

3.2 Low Level PID Control

The Low level control is a PID controller which is responsible for the accurate tracking of the Left and right wheel motors velocities $\omega_{r(i)}, \omega_{l(i)}$. Fig. 5 shows the structure of the low level PID controller.

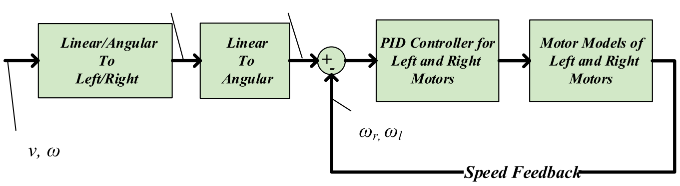

Figure 5: Low level PID

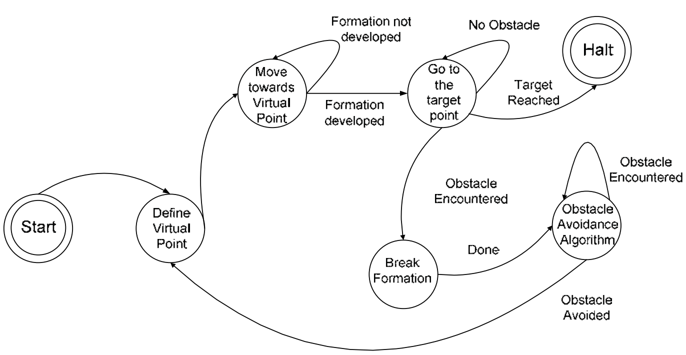

Figure 6: Finite state machine

The Output from the Fuzzy Controller is in the form of Linear and Angular velocities v_i, ω_i of Robot therefore the velocities must first be converted to Left and Right wheel motor velocities $v_{r(i)}, v_{l(i)}$. This conversion is carried out using (4)

The above conversion gives the linear velocities of the left and right wheel but the PID controller needs the angular velocity as reference. Therefore the angular velocities $\omega_{r(i)}, \omega_{l(i)}$ of the right and left motors can be obtained using the relation $v = r\omega$ where r is radius of the wheel.

The velocities $\omega_{r(i)}, \omega_{l(i)}$ are given to the PID controller as reference signal. The PID controller tracks these velocity references with desired accuracy and within certain time limits. The complete functionality of the High Level Fuzzy Cooperative Control is dependent on the assumption that the inner PID controller accurately tracks these velocity references.

3.3 Problem Description

The two main tasks of the robot is to follow a desired path as well as maintain a formation with other robots along the journey. The main idea behind the robot following a continuous path is to analyze the path in a set of discrete points. Each point serves as an intermediate destination to the robot, tracking each point will make the robot appear to be moving smoothly in a continuous path. The paths are being generated by the trajectory generator, the paths are modeled using a fifth order polynomial to generate reasonably difficult curved paths for the robots to follow.

The task of the robot is to move smoothly in a continuous path with best precision possible, passing through every point is not necessary but the robot should pass within the vicinity of a sampling point. The path following is divided into two categories.

1. When the robot is initially placed on the predefined path it then follows the path.
2. When the robot is initially placed away from the predefined path, it then moves forward to reach the path and track it.

As mentioned previously P_i being the Robot's position and Q_{di} being the next desired point we have considered v_i and ω_i as robot's linear and angular velocities. The objective of the path following controller is to generate an output such that the robots velocity $u_i = [v_i, \omega_i]^T$ tracks the desired reference velocity $u_{di} = [v_{di}, \omega_{di}]^T$. As the robot's velocity u_i tracks the desired reference velocity u_{di} the error minimizes i.e. $\|u_i - u_{di}\| \to 0$ which will eventually make $\|P_i - Q_{di}\| \to 0$

Now consider a team of mobile robots each of which having its own path following controller like the one described above, hence every individual robot will follow its desired path. For the cooperation problem every robot must follow their respective path in such a way that they maintain an inter robot formation along their journey as well as they must reach their final goal at the same time regardless of their path lengths.

3.4 Fuzzy Cooperative Controller

The Fuzzy Controller of Fig. 3 is responsible for the path following and cooperation of multiple mobile robots have two outputs v_i being the linear velocity and ω_i being the angular velocity for the robot to track. The fuzzy controller is based on Takagi - Sugeno Fuzzy Model. The control law equations are of the form.

$$\begin{bmatrix} v_i \\ \omega_i \end{bmatrix} = \begin{bmatrix} f_1(D_{rp(i)}, x_{err(i)}, y_{err(i)}, \alpha_{(i)}) \\ f_2(D_{rp(i)}, x_{err(i)}, y_{err(i)}, \alpha_{(i)}) \end{bmatrix} \quad (10)$$

As mentioned previously, the task of the fuzzy controller is to make the robot pass within the vicinity of the desired sampling point if not through it. The controller is designed such that if the sampling points are placed close to each other, then the robot will move at a slower speed but with higher precision. However if the sampling points are placed far from each other, then the robot movement will be less precise but with higher speed.

The membership function of the input $D_{rp(i)}$ is shown in Fig. 7, it is the distance between robot's current position and the next desired point.

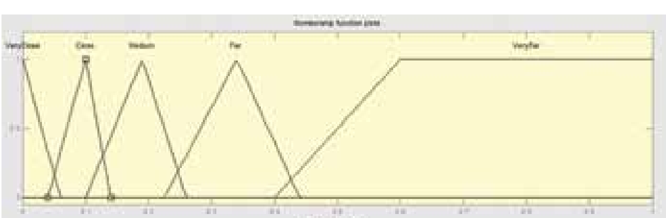

Figure 7: Membership function of $D_{rp(i)}$

The membership function of the input α_i is shown in Fig. 8. it is the error in orientation of robot from the next desired point.

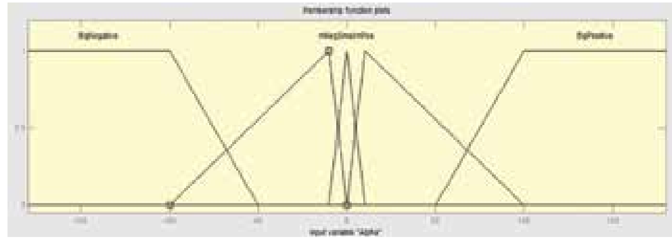

Figure 8: Membership function of α_i

The linear velocity obtained using $D_{rp(i)}$ and α_i is shown in Fig. 9. As can be seen from figure that linear velocity increases as the distance between robot and next sampling point increases and vice versa. However, α_i input has minimal effect on linear velocity.

The angular velocity profile obtained related to the inputs $D_{rp(i)}$ and α_i is shown in Fig. 10, it can be seen that angular velocity is dominated by α_i as the error in orientation increases so does the angular velocity to overcome the error and vice versa.

One of the problems of cooperative path following is that all robots should reach their final goal at the same time. Let us consider a case where the robot is at position $P_i = [x_i, y_i, \varphi_i]^T$has to move from point $Q_{di(n)} = [x_{di(n)}, y_{di(n)}, \xi_{di(n)}]^T$ to $Q_{di(n+1)}$ this means that robot's next desired sampling point is $Q_{di(n+1)}$. If robot passes the point $Q_{di(n+1)}$ and $Q_{di(n+2)}$ then when moving to next step $Q_{di(n+1)}$ is left behind from the actual position of robot or mathematically $(x_i > x_{di} \Rightarrow x_{err(i)} < 0)$. This problem is explained in Fig. 4. To avoid the condition of robot moving backwards we use the input $x_{err(i)}$. The fuzzy rule base contains the following rule to avoid the the above mentioned condition.

Rule: If $x_i > x_{di}$ then robot will stop, until the condition $x_i < x_{di}$ is met

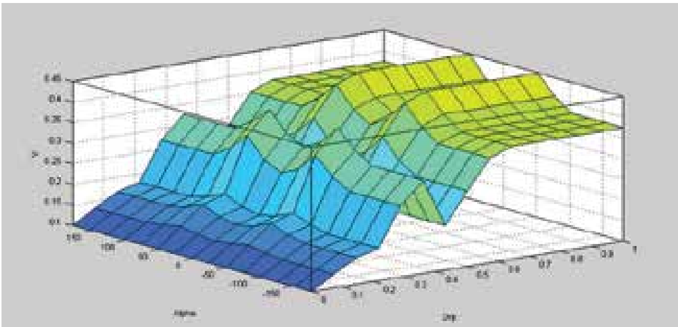

Figure 9: Linear velocity obtained by fuzzy controller

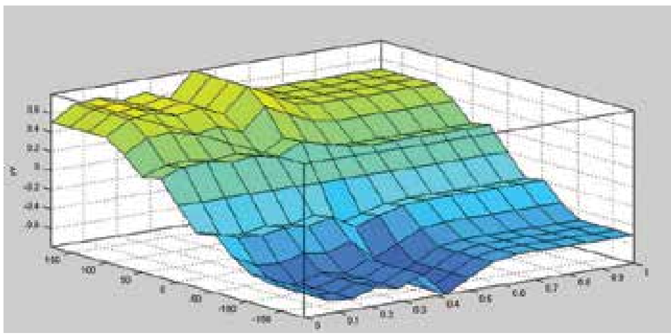

Figure 10: Angular velocity obtained by fuzzy controller

Another problem related to path following that need to be addressed, caused the addition of the input $y_{err(i)}$. If there is an error in the vertical position of robot $y_{err(i)}$ but not in the orientation then robot will travel parallel to the desired path and will never reach it. This can be seen from Fig. 15. The input $D_{rp(i)}$ has minimal effect on the angular velocity therefore it cannot turn robot towards the target point there should be an error in orientation α_i to turn the robot towards the target point.

In order to address above mentioned problem we introduced a new variable λ_i which is angle measured in degrees. λ_i is added to α_i if there is an error in y coordinate,it will help the robot to turn towards target point even if the $\alpha_i = 0$, it will tell the robot to turn towards the target point and will decrease as $y_{err(i)}$ decreases and will be zero when robot catch the desired path.

$$if\left|y_{err(i)}\right| > 0 \Rightarrow \alpha_i(new) = \lambda_i + \alpha_i \qquad (11)$$

The membership function of $y_{err(i)}$ is shown in Fig. 11. The relationship between $y_{err(i)}$ and λ_i is shown in Fig. 12, it can be seen that λ_i increases as $y_{err(i)}$ increases and vice versa, hence it makes sure that robot turn towards the target point if there exist an error in y-coordinate even when the error in orientation is zero.

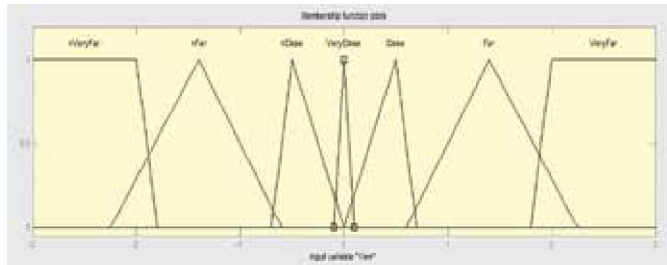

Figure 11: Membership fuction of $y_{err(i)}$

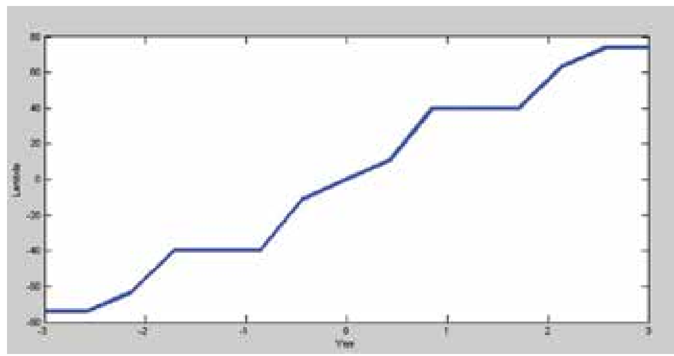

Figure 12: Relationship between $y_{err(i)}$ and λ_i

The path of each robot is divided into equal number of small segment and the parameter ς_i will keep track of the current segment the robot is executing. The robots are required to maintain $\varsigma_i = \varsigma_j$ for all i, j. For cooperation it is necessary that all paths are divided into equal number of segments regardless of their shape and length. If a path is longer than the sampling points will be far from each other or the distance between sampling point will increase and vice versa. Hence the robot will move faster or slower if the sampling points are close or far from each other respectively. Therefore if each robot tracks their respective sampling points then they will be moving in a cooperative behavior and will reach the final point at the same time. If a robot is ahead of its path then it will wait for other robots to catch up and then start following its path. This is achieved by x coordinate error input i.e if $x_{err(i)} < 0$ then robot will stop. The effect of

$x_{err(i)}$ and $D_{rp(i)}$ on linear velocity v_i is shown in Fig. 13 and the obtained angular velocity ω_i from the input $x_{err(i)}$ and α_i is shown in Fig. 14.

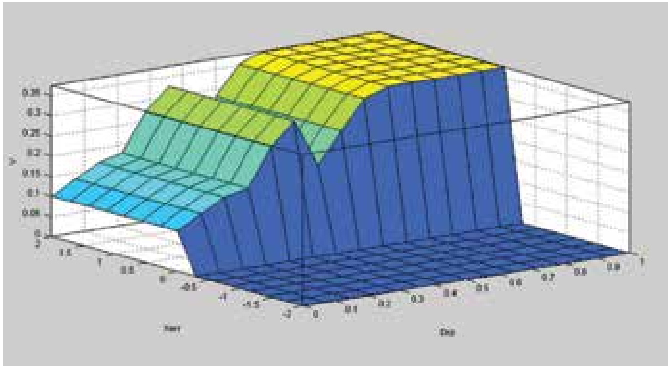

Figure 13: Linear velocity obtained from $x_{err(i)}$ and $D_{rp(i)}$

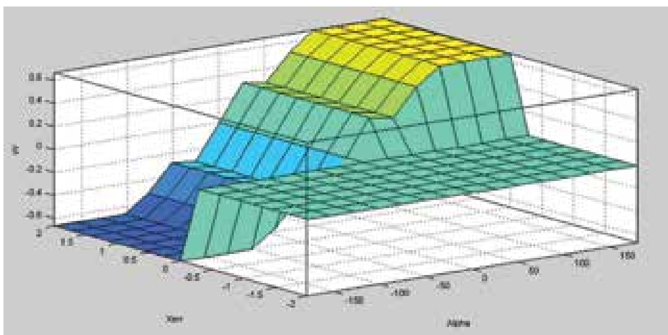

Figure 14: Angular velocity obtained from $x_{err(i)}$ and α_i

The Rule Base of the fuzzy controller is shown in Table 1. On the basis of these rules the fuzzy controller evaluates the inputs and generates the output. All the rules are very much self-explanatory like if the distance between the next sampling point and robot $D_{rp(i)}$ increase the fuzzy controller increases the linear velocity output so that the robot can catch its target. Similarly if the orientation error α_i increases then the fuzzy controller increases the angular velocity output to overcome the orientation error and correct the robot heading direction. Also if the robot is ahead of its path the Fuzzy controller will make both linear and angular velocity outputs zero to stop the robot.

Table 1: Fuzzy rule base

Rule 1	*If $D_{rp(i)}$ is **Very Close** and $X_{err(i)}$ is **Positive** then v_i is **Very Very Slow**, ω_i is **Zero***
Rule 2	*If $D_{rp(i)}$ is **Close** and $X_{err(i)}$ is **Positive** then v_i is **Very Slow**,ω_i is **Zero***
Rule 3	*If $D_{rp(i)}$ is **Medium** and $X_{err(i)}$ is **Positive** then v_i is **Slow**,ω_i is **Zero***
Rule 4	*If $D_{rp(i)}$ is **Far** and $X_{err(i)}$ is **Positive** then v_i is **Fast**,ω_i is **Zero***
Rule 5	*if $D_{rp(i)}$ is **Very Far** and $X_{err(i)}$ is **Positive** then v_i is **Very Fast**, ω_i is **Zero***
Rule 6	*if $X_{err(i)}$ is **Positive** and α_i is **Big Negative** then v_i is **Very Very Slow**,ω_i is **Big Negative***
Rule 7	*if $X_{err(i)}$ is **Positive** and α_i is **Medium Negative** then v_i is **Very Very Slow**, ω_i is **Negative***
Rule 8	*if $X_{err(i)}$ is **Positive** and α_i is **Small** then v_i is **Very Very Slow**, ω_i is **Zero***
Rule 9	*if $X_{err(i)}$ is **Positive** and α_i is **Medium Positive** then v_i is **Very Very Slow**,ω_i is **Positive***
Rule 10	*if $X_{err(i)}$ is **Positive** and α_i is **Big Positive** then v_i is **Very Very Slow**, ω_i is **Big Positive***
Rule 11	*if $X_{err(i)}$ is **Negative** then v_i is **Zero**,ω_i is **Zero***

4. SIMULATION RESULTS

Table 2 shows the parameters of the robot and DC motor model.

The simulation is carried in Simulink with a fixed step size of 1e^{-2}. To test the cooperation problem we use a team of three identical mobile robot models, two different experiments were designed to test the cooperative algorithm. First the robots are tested with paths of different lengths but placed on the path initially, then the robots are given same path but are placed away from the paths, result are collected and discussed below.

Table 2: Parameters of the robot and DC motor model

Parameter	Value	Unit
Robot Model Parameters		
L_i	0.2	m
r	0.045	m
DC Motor Model Parameters		
R	3.07	*ohms*

L	0.04	mh
J	0.0294	$Kg.m^2$
B	0.0141	$N.m.s/rad$
K_e	0.65	$N.m/Amp$
K_t	0.65	$V.s/rad$

4.1 Experiment No. 1

In this experiment, three mobile robots are used each with a different path (different lengths). Robot 1 has the smallest path and Robot 3 has the longest path. The robots are initially placed on the path the initial positions of the robots and path lengths are given below.

$$P_1 = [x_1 \quad y_1 \quad \varphi_1]^T = \left[0.01 \quad 11.4303 \quad -\frac{\pi}{4}\right]^T$$
$$P_2 = [x_2 \quad y_2 \quad \varphi_2]^T = \left[0.01 \quad 6.7207 \quad -\frac{\pi}{4}\right]^T \quad (12)$$
$$P_3 = [x_3 \quad y_3 \quad \varphi_3]^T = \left[0.01 \quad 2.0489 \quad -\frac{\pi}{4}\right]^T$$

The robots are required to follow their respective paths as well as maintain a formation along the journey also they must reach their final destination at the same time regardless of the path lengths.

Fig. 15 shows the cooperation of the mobile robots, as can be seen that robot 1 has the shortest path whereas Robot 3 has the longest path. The round markers are used to highlight the position of each robot at a given time. The first markers on each path will indicate the initial position of the robots at t_0, the second marker will indicate the position of each robot at t_1 and so on. These markers are distributed equally with respect to time. As can be seen that the robot are placed vertically above each other initially, the successive markers shows that the robots are moving along their path but are also maintaining an inter robot formation throughout the journey, and reach their final destination at the same time.

Fig. 16 shows y_{err} or the tracking error, it can be seen that the robots quickly covers the initial tracking error due to the difference in initial orientation and then follows the path with minimal error.

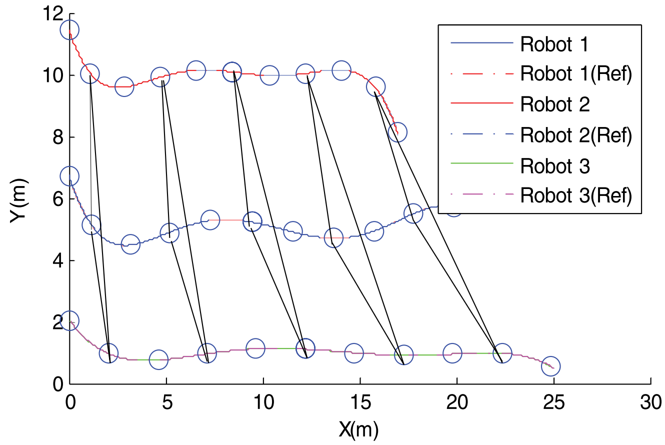

Figure 15: Cooperative path following (Experiment 1)

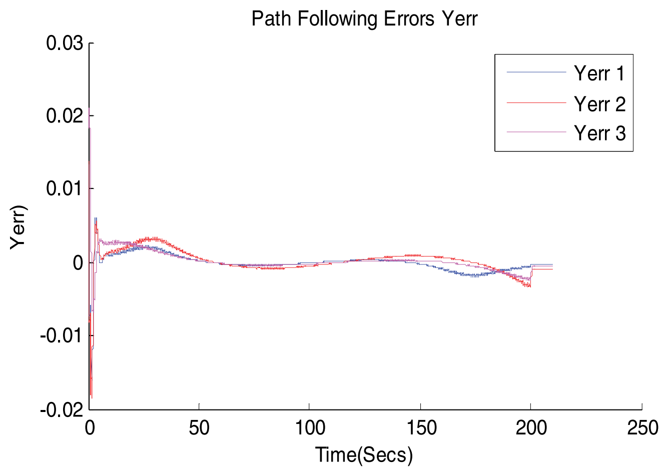

Figure 16: Tracking error

Fig. 17 and 18 shows the linear and angular velocities respectively. It can be seen that robot 1 has the lowest while robot 3 has the highest linear velocity. This is due to the fact that robot 1 has the smallest while robot 3 has the longest path. The angular velocity profiles shows the robots turning with respect to their path curves.

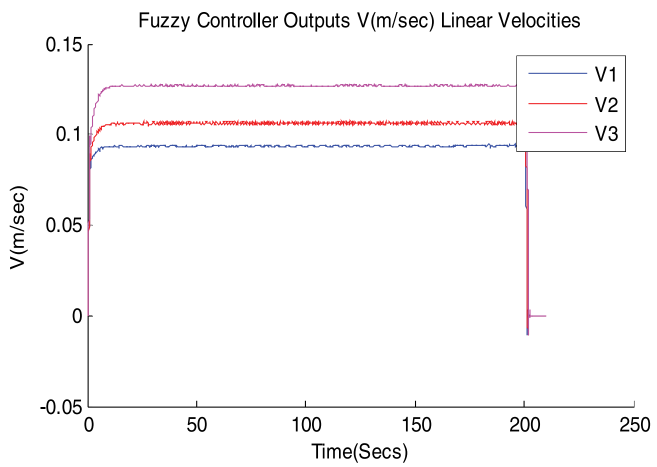

Figure 17: Linear velocity

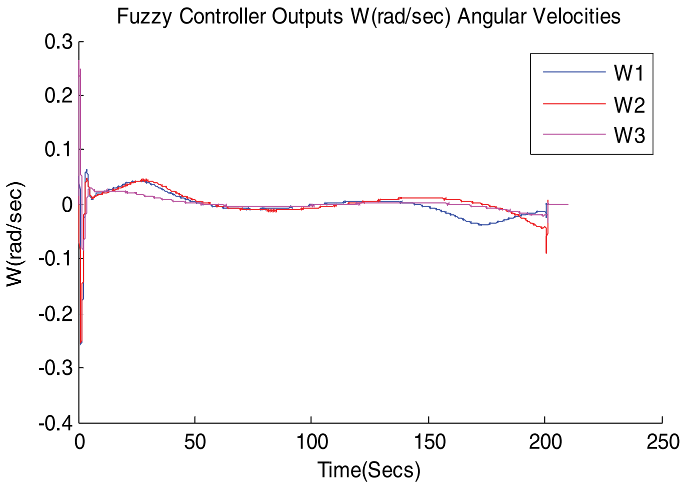

Figure 18: Angular velocity

4.2 Experiment No.2

In this experiment three robots are used, each of which is provided with the same path, but they are placed away from their respective path initially. Robot 1 and robot 3 are placed ahead of their trajectory while Robot 1 is placed behind its trajectory. The robots initial positions are given below.

$$\begin{aligned} P_1 &= [x_1 \quad y_1 \quad \varphi_1]^T = \left[1.0 \quad 11.0 \quad -\tfrac{\pi}{2}\right]^T \\ P_2 &= [x_2 \quad y_2 \quad \varphi_2]^T = [-0.5 \quad 8.0 \quad 0]^T \\ P_3 &= [x_3 \quad y_3 \quad \varphi_3]^T = [1.5 \quad -1.0 \quad 0]^T \end{aligned} \qquad (13)$$

The robots are required to follow their respective as well as maintain an inter robot formation. Since the robots are not placed on their respective paths, therefore first they need to catch the trajectory, and they must reach their respective end points at the same time. Fig. 19 shows the cooperation of robots in this experiment, it can be seen that Robot 1 and Robot 3 are placed ahead of their respective paths, while Robot 2 is placed behind the trajectory. Note that Robot 2 starts immediately as soon as the simulation starts while Robot 1 and 3 remains idle waiting for the trajectory to move forward. This is because of the assumption that if a robot is ahead of its path then it will wait for other robots to catch up.

The markers on the paths shows that around 3 meter mark, the robots achieve synchronization (formation), then maintains the formation as they move forward along their respective paths and reach their final destination at the same time.

Fig. 20 shows the tracking error y_{err} of the robots. Initially tracking error of Robot 1 and 3 is a function of the trajectory as the robots are standing still. However Robot 2 quickly overcomes its error. It can be seen that as soon as robots starts moving they overcomes y_{err} very quickly. Once the robots achieve formation they follow their respective paths with minimal tracking error.

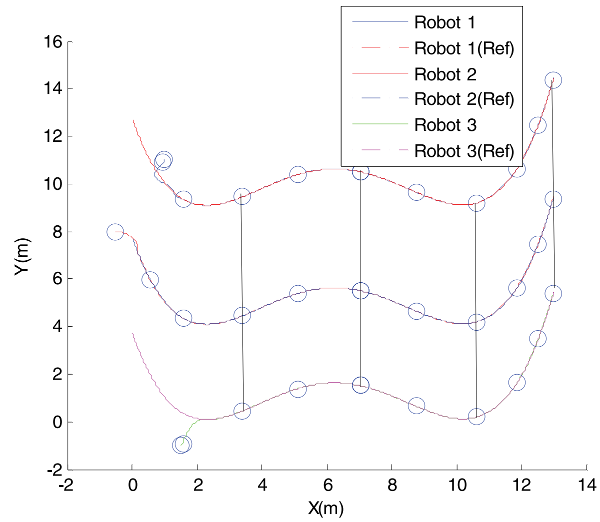

Figure 19: Cooperative path following (Experiment 2)

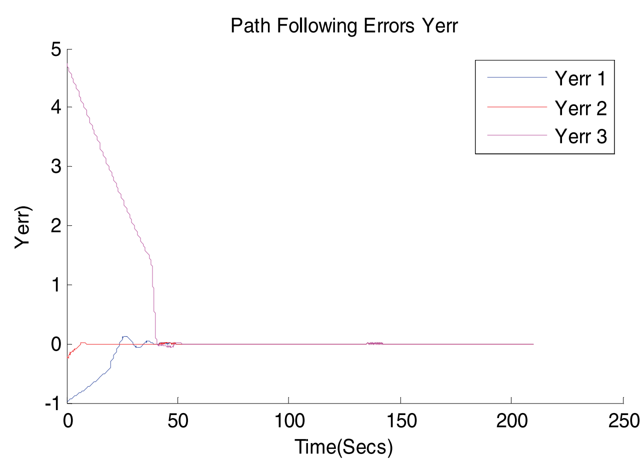

Figure 20: Tracking error

Fig. 21 shows the linear velocities of robots. From figure it can be seen that initially only Robot 2 (RED) is moving (has non zero linear velocity). This is because, Robot 2 is placed behind its trajectory so it has to move fast to catch the trajectory. After about 60 secs Robot 2 starts moving as its trajectory passes its initial position, similarly Robot 3 starts moving at about 90 secs. All three robots have to cover some distance as soon as they start moving to catch the trajectory therefore an initial peak can be seen for all three linear velocities. After catching the trajectory all the robots linear velocities becomes same, this is due to the fact that all the robots have same path similarly all the robots stop (Linear velocity zero) at the same time.

Fig. 22 shows the angular velocities of the robots. As discussed above initially only Robot 2 is moving (non zero angular velocity). The initial peaks in angular velocities represent the controller effort to correct the heading of the robot with respect to the trajectory. Once the robots achieve formation their angular velocities become similar because of same paths.

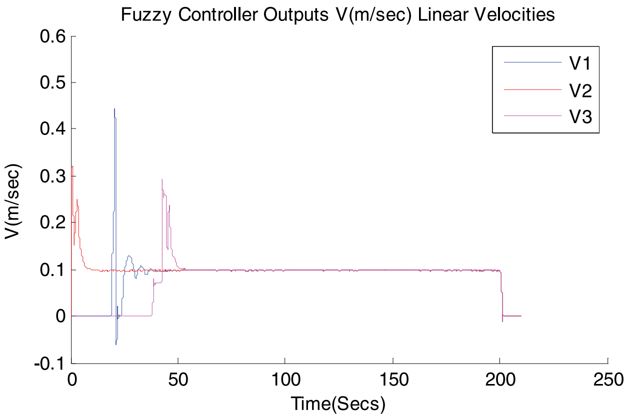

Figure 21: Linear velocities

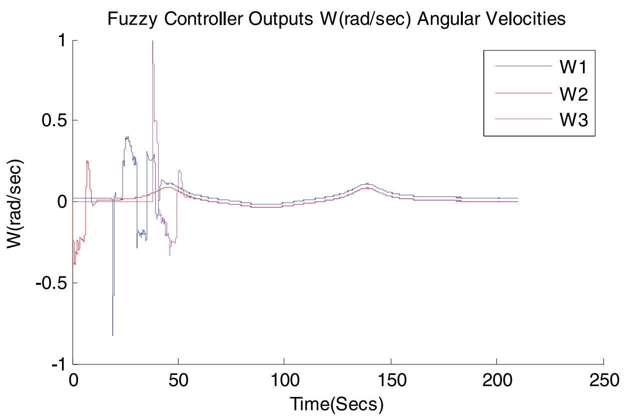

Figure 22: Angular velocities

5. CONCLUSION

This work covers the formation control of mobile robots. The proposed design consists of a hierarchal control architecture a low level PID controller and high level fuzzy cooperative controller. The PID controller tracks the reference speed of the robot's wheel motors; it was tuned for the motor parameters to effectively track the reference speed with minimum tracking time and steady state error.

The fuzzy controller is where the path following and cooperation is done. The cooperative behavior was testedusing a team of three identical robots were used. Different simulation experiments were conducted in which the robots were subjected to different initial conditions and they wer supposed to follow their respective paths and maintain a formation amongst them. The results shows that the Fuzzy Cooperative Controller effectively achieves its goals of individual path following and group cooperation, it has been shown that the robots tracks their respective paths with minimal error and maintain the formation while travelling.

This work is a small effort towards the Formation control of mobile robots. Recommended future work will be to improve the fuzzy controller by incorporating obstacle avoidance and the ability to move in known as well as unknown environments.

REFERENCES

[1] Beard, Randal W., Jonathan Lawton, and Fred Y. Hadaegh. "A coordination architecture for spacecraft formation control." IEEE Transactions on control systems technology 9, no. 6 (2001): 777-790.

[2] Seanor, Brad, Yu Gu, Marcello R. Napolitano, Giampiero Campa, Srikanth Gururajan, and Larry Rowe. "3-aircraft formation flight experiment." In Control and Automation, 2006. MED'06. 14th Mediterranean Conference on, pp. 1-6. IEEE, 2006.

[3] Beard, By Randal W., Timothy W. McLain, Derek B. Nelson, Derek Kingston, and David Johanson. "Decentralized cooperative aerial surveillance using fixed-wing miniature UAVs." Proceedings of the IEEE 94, no. 7 (2006): 1306-1324.

[4] Wu, Naiqi, and MengChu Zhou. "Modeling and deadlock control of automated guided vehicle systems." Mechatronics, IEEE/ASME Transactions on 9, no. 1 (2004): 50-57.

[5] Howard, A., L. Parker, and G. Sukatme. "Experiments with a large heterogeneous mobile robot team." Int. J. Robotics Research 25, no. 5-6 (2005): 431-447.

[6] Healey, Anthony J. "Application of formation control for multi-vehicle robotic minesweeping." In Decision and Control, 2001. Proceedings of the 40th IEEE Conference on, vol. 2, pp. 1497-1502. IEEE, 2001..

[7] Bevly, David M., and Bradford Parkinson. "Cascaded Kalman filters for accurate estimation of multiple biases, dead-reckoning navigation, and full state feedback control of ground vehicles." Control Systems Technology, IEEE Transactions on 15, no. 2 (2007): 199-208.

[8] Han, Soonshin, HyungSoo Lim, and JangMyung Lee. "An efficient localization scheme for a differential-driving mobile robot based on RFID system." Industrial Electronics, IEEE Transactions on 54, no. 6 (2007): 3362-3369.

[9] Purvis, Keith B., Karl J. Åström, and Mustafa Khammash. "Estimation and optimal configurations for localization using cooperative uavs." Control Systems Technology, IEEE Transactions on 16, no. 5 (2008): 947-958.

[10] Balch, Tucker, and Ronald C. Arkin. "Behavior-based formation control for multirobot teams." Robotics and Automation, IEEE Transactions on 14, no. 6 (1998): 926-939.

[11] Li, Hao, and Simon X. Yang. "A behavior-based mobile robot with a visual landmark-recognition system." Mechatronics, IEEE/ASME Transactions on8, no. 3 (2003): 390-400.

[12] Gu, Dongbing, and Huosheng Hu. "Integration of coordination architecture and behavior fuzzy learning in quadruped walking robots." Systems, Man, and Cybernetics, Part C: Applications and Reviews, IEEE Transactions on37, no. 4 (2007): 670-681.

[13] Huang, Jiangyang, Shane M. Farritor, Ala´ Qadi, and Steve Goddard. "Localization and follow-the-leader control of a heterogeneous group of mobile robots." Mechatronics, IEEE/ASME Transactions on 11, no. 2 (2006): 205-215.

[14] Lewis, M. Anthony, and Kar-Han Tan. "High precision formation control of mobile robots using virtual structures." Autonomous Robots 4, no. 4 (1997): 387-403.

[15] Ghommam, Jawhar, Hasan Mehrjerdi, Maarouf Saad, and FaiçalMnif. "Formation path following control of unicycle-type mobile robots." Robotics and Autonomous Systems 58, no. 5 (2010): 727-736.

[16] Chang, Yeong-Chan, and Bor-Sen Chen. "Robust tracking designs for both holonomic and nonholonomic constrained mechanical systems: adaptive fuzzy approach." Fuzzy Systems, IEEE Transactions on 8, no. 1 (2000): 46-66.

[17] Li, Tzuu-Hseng S., Shih-Jie Chang, and Wei Tong. "Fuzzy target tracking control of autonomous mobile robots by using infrared sensors." Fuzzy Systems, IEEE Transactions on 12, no. 4 (2004): 491-501.

[18] Maalouf, Elie, Maarouf Saad, and HamadouSaliah. "A higher level path tracking controller for a four-wheel differentially steered mobile robot."Robotics and Autonomous Systems 54, no. 1 (2006): 23-33.

[19] Antonelli, Gianluca, Stefano Chiaverini, and Giuseppe Fusco. "A fuzzy-logic-based approach for mobile robot path tracking." IEEE Transactions on Fuzzy Systems 15, no. 2 (2007): 211-221.

[20] Mbede, Jean Bosco, Xinhan Huang, and Min Wang. "Robust neuro-fuzzy sensor-based motion control among dynamic obstacles for robot manipulators." Fuzzy Systems, IEEE Transactions on 11, no. 2 (2003): 249-261.

[21] Zhu, Anmin, and Simon X. Yang. "Neurofuzzy-based approach to mobile robot navigation in unknown environments." Systems, Man, and Cybernetics, Part C: Applications and Reviews, IEEE Transactions on 37, no. 4 (2007): 610-621.

CONTROL OF VERTICAL SPINDLE SURFACE GRINDING FROM A MULTI-AXIS NUMERICALLY CONTROLLED MACHINE

Authors: Sheikh Abdullah[1], Syed Irtiza Ali Shah[1], Malik Muhammad Awais[1], Aman Sarwar[1]

[1]Department of Mechanical & Aerospace Engineering Air University Islamabad, Pakistan,
engrshabdullah@gmail.com (Sheikh Abdullah), irtiza@mail.au.edu.pk (Syed Irtiza Ali Shah),
malik.awais19@gmail.com (Malik Muhammad Awais), 170982@students.au.edu.pk (Aman Sarwar)

Received: 22-April-2022 / Revised: 24-June-2022 / Accepted: 06-July-2022
Karachi Institute of Economics and Technology || Technology Forces Journal, Volume 4, Issue 1, 2022

ABSTRACT

Due to the increasing need for components comprised of hard and brittle materials such as glasses, steel alloys, and sophisticated ceramics, standard grinding and polishing techniques are no longer able to meet the expectations of today's precision manufacturing community. Grinding machines' functional capabilities, control systems, and peripheral process monitoring equipment have all improved during the last 20 years. Process enhancement technologies such as touch detection, wheel balancing, and in-process gauging may be incorporated into higher-end grinding machines based on specific customer requirements; however, due to the differing features and functionality of equipment from different suppliers, this requires significant customization work by the manufacturer. Moreover, the execution of long-proposed optimization strategies such as adaptive and intelligent control has not progressed significantly beyond specific research programs tied to a specific machine and controller, frequently using non-industrial equipment for key process data monitoring.However, it is vital and absolutely necessary to carry out such activities using a scientific approach, i.e., the process should be quantitatively controlled and optimized rather than done by trial and error. There is also a need to produce innovative and modern control system for controlled vertical spindle surface grinding multi-axis Computer Numerical Control (CNC) machine.Theoretical modelling and instrumentation for controlled vertical spindle surface grinding multi-axis Computer Numerical Control (CNC) machine are provided and addressed in depth in this study. During the grinding process, a method in which controlling of surface parallelism by changing the depth of cut is done, is applied. The achievable single pass tolerances in vertical spindle surface grinding are frequently restricted by machine compliance and also, the grinding wheel. The approach presented here involves precisely altering the depth of cut during grinding to maximize dimensional precision without the need for additional spark out passes. In this stage, the projected deflection from the simulated compliance and the measured vertical force are utilized to perform the correction. Two distinct methodologies are compared to determine the system's compliance. A controller of multi-axis commercial Computer Numerical Control (CNC) is altered to process the measurement of dynamometer in real-time, calculate controlling commands, and actuate servo loops. Because the system's deflection fluctuates with force of grinding, using depth of cut manipulation, a tracking controller tracks the expected deflection of the wheel, cancelling out part form defects. The results from experiments are shown for a variety of process settings, demonstrating the efficiency in terms of ground part parallelism, of the compensation system. It also resulted in significant improvement in quality of surface grinding.

Keywords: Deflection, Grinding, Depth of cut.

1. INTRODUCTION

Grinding machines are a category of machine tool that performs specific finishing operations on machined components to create a high-quality surface finish and a certain profile. Grinding is the final process done on a component, and it could be done manually for individual components or automatically for manufacturing batches of (similar) components. Conventional hand operated machines needed the operator to rotate control handwheels to move the axes and set numerous switches and limitations to manage mechanically automated features such as axis incremental and reversal infeed or down feed. Their efficiency as well as productivity are virtually entirely determined by the operator's ability and expertise, who will select appropriate increments and speeds based on dimensions and materials, as well as check grinding wheel condition and component quality. Once started, these machines can run semi-autonomously, with the operator changing parts and repeating the cycle as needed. During the 1980s, more sophisticated and complex grinding machines using Computer Numerical Control (CNC) were widely introduced; these allowed full electronic control of axis movements via servo drives, control of machine safety, interfacing to other electronic equipment, and, most importantly, the ability to generate and run complex part-programs that defined the machining operation [1]. Numerical control is a sort of programmable automation in which the process is controlled by numbers, letters, and symbols. Computer Numerical Control (CNC) machining is a manufacturing process that involves the use of computers to control machine tools such as grinders, mills, and lathes.

The most prevalent type of grinding process is surface grinding. It is a common sight in heavy industry, where various metal and nonmetal objects must be refined and smoothed as part of the finishing process.

A surface grinder is made up of a table that holds the abrasive wheel above it. A chuck is a device that holds the item being worked on, known as a workpiece, in place. Surface grinders are classified into three types: vertical spindle, horizontal spindle, single disc grinders, and double disc grinders.

Horizontal spindle grinders: They are ideal for high-precision work on slanted or tapered surfaces, as well as slots or sunken surfaces. They are also known as peripheral grinders.

Single-disc and double-disc grinders: They are available in spindle configurations of both vertical and horizontal directions. These grinders have a greater contact's surface area among the grinding surface and the workpiece and may grind both sides simultaneously. Disc grinders can accept rotors, plates, spacers, gears, and washers.

Vertical-spindle grinders: These grinders also known as wheel-face grinders, and are commonly used for rapid material removal. The face of grinding wheel is lowered onto the workpiece under it. These grinders are best suited for spacers, stops, stators, gears, inner plates, gears and inner rings, as well as wafers and rotors.

The goal of the work presented here is to intelligently control a vertical spindle surface grinding from a multi axis Computer Numerical Control machine.

2. LITERATURE REVIEW

2.1 Prediction T-S Fuzzy Control Method for Prediction of Workpiece' Rotation Speed on grinding machine of Camshaft

Through the studies on non-circular grinding, the manufacturing industry has made a huge breakthrough. This non-circular grinding model is mostly applied on camshaft by China's automobile industry. Through this research we analyze a grinding mathematical model. This mathematical model will help us determine the workpiece's reduction ratio in non-circular section. It can also help us determine the maximum speed of feeding, jerk along with the acceleration of grinding wheel. Through the analysis of feed displacement and acceleration curves of grinding wheel, a linear approximation fuzzy control model of cam rotation was established. Consequently, a rule parameter of fuzzy table was designed, which helped to predict and optimize the cam rotation speed.

Fig. 1 shows the mathematical model of camshaft CNC grinding. The cam's rotation, along C axis, of camshaft grinding machine and grinding wheel's feeding on X axis during the rotation of grinding wheel are controlled by the commands given through CNC.

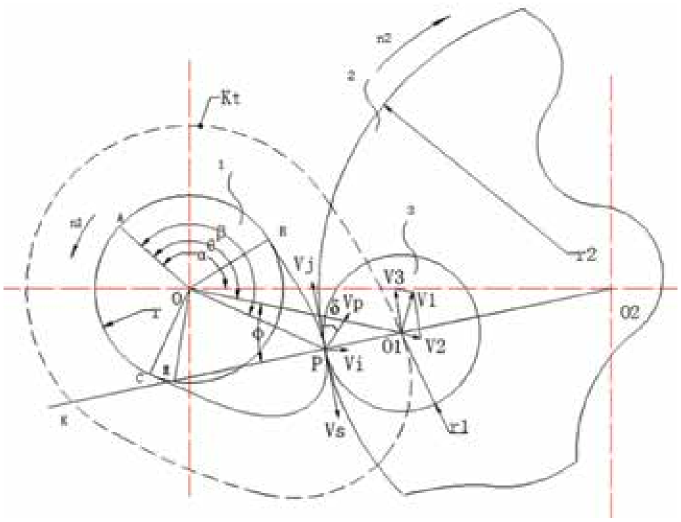

Figure 1: Mathematical model representing CNC camshaft grinding [21].

Here O represents the center of cam base circle's center, O_1 represents the roller measuring head's center. Similarly, O_2 represents the center of grinding wheel.

Here,

Angular velocity at point P =

Angular velocity when the cam rotates to base circle $= w_0$

Radius of cam base circle is OA = r

Radius of roller measuring head is $PO_1 = r_1$

Radius of grinding wheel is $O_2P = r_2$

Angle of roller measuring head ÐAOO1 = θ

Angle of cam ÐAOO2=$\alpha(\theta)$

Angle between cam and grinding wheel tangent P is DAOP = $\beta(\theta)$.

Similarly, ÐOO1M = φ.

$$X(\theta) = OO_2 - r_2 - r \qquad (1)$$

where

$$OO_2 = \sqrt{OO_1^2 + O_1O_2^2 + 2OO_1 \times \cos(\varphi)}$$

Here X(θ) represents feed displacement of grinding wheel.

$O_1O_2 = r_2 - r_1$

$OO_1 = r_2 + H(\theta) + r_1$

Lift value of cam is represented by $H(\theta)$.

$$\varphi = \text{arctg}\frac{OM}{OO_1} = arctg\frac{\frac{dH(\theta)}{d\theta}}{OO_1}$$

$$\alpha(\theta) = \theta - \angle O_2OO_1 = \theta - \arcsin\left(\frac{\sin(\pi-\varphi)\times O_1O_2}{OO_2}\right) \qquad (2)$$

Similarly when the cam rotates to a (q) the cut-in depth ap is given as

$$a_{ep} = a_p \times \frac{v_j}{v_s} = \frac{Q_{W'}}{v_s} \qquad (3)$$

Here linear velocity is being represented by v_s.

On the basis of above equations we proceed further as

$$\omega(\theta) = \frac{\omega_0 \times r}{\sqrt{(\frac{d\rho(\theta)}{d\beta(\theta)})^2 + \rho(\theta)^2\frac{d\beta(\theta)}{d\alpha(\theta)}}} \qquad (4)$$

$$F(\theta) = 360 \times n(\theta) = \frac{10800 \times \omega(\theta)}{\pi} \qquad (5)$$

$$where\ v_0 = \omega_0 r \quad , \quad \omega(\theta) = \frac{d\alpha(\theta)}{dt}$$

$$v_s = \omega(\theta)\sqrt{\frac{d\rho(\theta)}{d\beta(\theta)} + \rho(\theta)^2}\,\frac{d\beta(\theta)}{d\alpha(\theta)}$$

$$\beta(\theta) = \theta + \angle O_2OP = \theta + \arcsin\left(\frac{\sin(\varphi)\times PO_1}{OP}\right)$$

$$OP = \rho(\theta) = \sqrt{OO_1^2 + PO_1^2 + 2 \times OO_1 \times PO_1 \times \cos(\varphi)}$$

F(θ) and a (θ) they can fit into Eq. (2) and (5) respectively.

The second, third and fourth derivative of the pairs obtained in Eq. (1) are

$$v(\theta) = \frac{d(X(\theta))}{d\theta} \qquad (6)$$

$$a(\theta) = \frac{d(v(\theta))}{d\theta} \qquad (7)$$

$$j(\theta) = \frac{d(a(\theta))}{d\theta} \qquad (8)$$

Here $v(\theta)$, $j(\theta)$, and $a(\theta)$ represent the feeding speed, the jerk, and the acceleration of the grinding wheel, respectively.

Simulations representing connection of Eq. (1), (5), (6), and (7) with Eq. (2) are shown in the graphs below

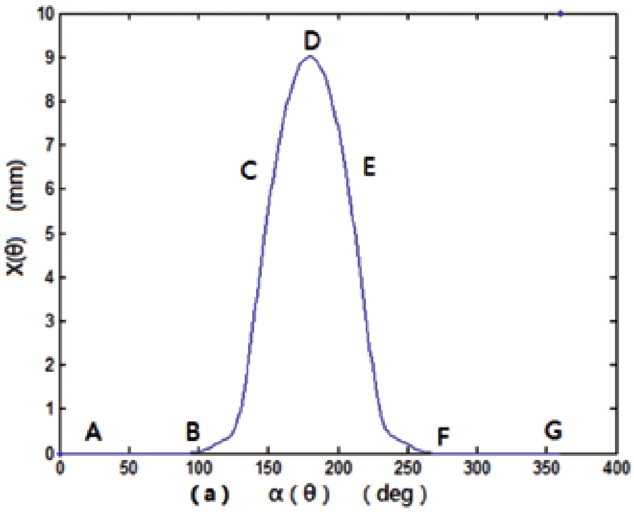

Figure 2(a): Grinding wheel' feed displacement X(θ) curve [21].

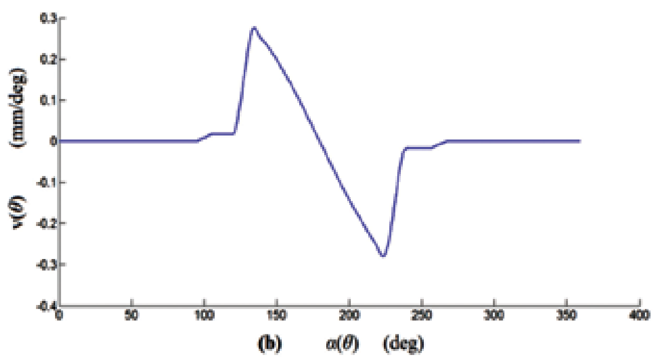

Figure 2(b): Grinding wheel's Feeding speed v(θ) curve [21].

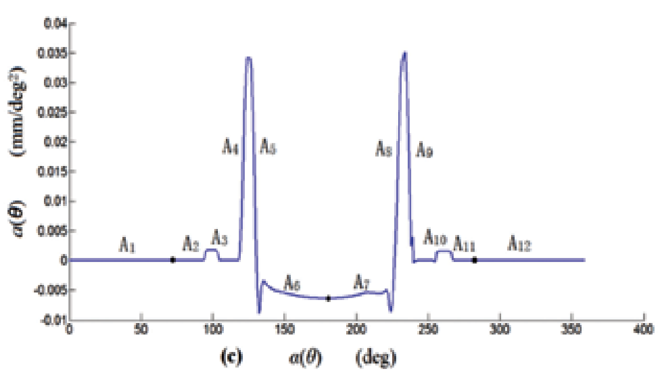

Figure 2(c): Horizontal feeding acceleration a(θ) curve of the grinding wheel [21].

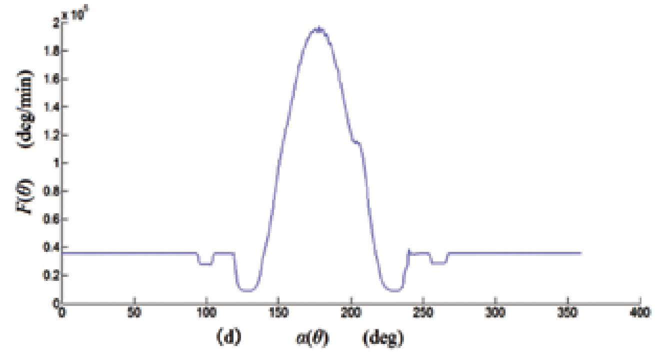

Figure 2(d): Cam's Rotation speed curve [21].

Control method for S shaped acceleration and deceleration is being implemented to counteract the effects of grinding wheel acceleration. For this purpose, the limiting parameters are

$$\begin{cases} v(\theta_i) \leq v_{max} \\ a(\theta_i) \leq a_{max} \\ j(\theta_i) \leq j_{max} \\ k = \frac{\omega_{max}}{1.2\omega_0} \end{cases} \tag{9}$$

$v(\theta i)$, $a(\theta i)$, and $j(\theta i)$ represent the ith interpolation period of feeding speed, acceleration and jerk respectively. Similarly, v_{max}, a_{max}, and j_{max} represent the maximum of feeding speed, acceleration and jerk respectively. Using the displacement curve of feed segmentation of grinding wheel is carried out, which helps to decompose the system into 5 modes of deceleration and acceleration.

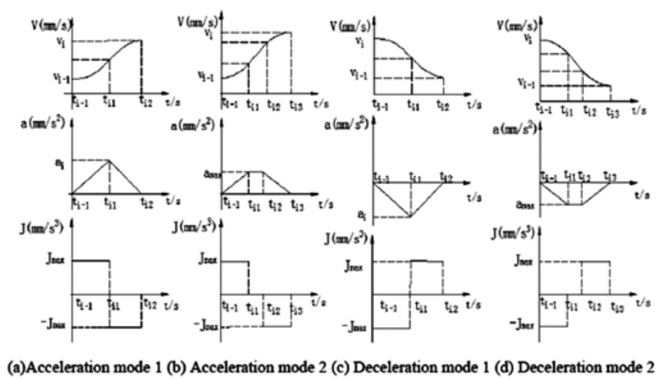

Figure 3: Modes of S-shaped acceleration and deceleration [21].

Here Accleration Mode 1:

$$\begin{cases} s_i(t_{i1}) = v_{i-1}t_{i1} + \frac{1}{6}j_{max}t_{i1}^3 \\ v_{i1} = v_{i-1} + \frac{1}{2}j_{max}t_{i1}^2 \\ t_{i1} = t_{i2} = \frac{T_{si}}{2} \\ s_{i2}(t) = v_{i1}t_{i2} + \frac{1}{2}a_i t_{i2}^2 - \frac{1}{6}j_{max}t_{i2}^3 \\ a_i = \frac{1}{2}j_{max}T_{si} \\ v_{i2} = v_{i1} + a_i t_{i2} - \frac{1}{2}j_{max}t_{i2} = v_{i-1} + \frac{1}{4}j_{max}T_{si}^2 \\ \Delta x_i = s_{i1}(t) + s_{i2}(t) = v_{i-1}T_{si} + \frac{1}{8}j_{max}T_{si}^3 \end{cases} \quad (10)$$

Here s_{i1}(t), s_{i2}(t) are feed displacement in t_{i1} and t_{i2} respectively.

Here s_{i1}(t), *ai*, v_{i1} are the feed displacement, accelerated speed and speed in t_{i1} respectively. Similarly, s_{i2}(t), a_i, v_{i2} are the feed displacement, accelerated speed and speed in ti1 respectively. Interpolation period is represented by T_{si}. Δx_i represents the feed displacement in one interpolation period.

T_{si} is derived with the help of Eq. 10.

Mode 2 of Acceleration:

$$\begin{cases} s_i(t_{i1}) = v_{i-1}t_{i1} + \frac{1}{6}j_{max}t_{i1}^3 \\ v_{i1} = v_{i-1} + \frac{1}{2}j_{max}t_{i1}^2 \\ t_{i1} = t_{i3} = \frac{a_{max}}{j_{max}} \\ v_{i2} = v_{i1} + a_{max}t_{i2} \\ s_{i2}(t_{i2}) = v_{i2}t_{i2} + \frac{1}{2}a_{max}t_{i2}^2 \\ s_{i3}(t_{i3}) = v_{i2}t_{i3} + \frac{1}{2}a_{imax}t_{i3}^2 - \frac{1}{6}j_{max}t_{i3}^3 \\ v_{i3} = v_{i-1} + a_{max}t_{i3} \\ \Delta x_i = s_{i1}(t) + s_{i2}(t) + s_{i3}(t) \\ a_{max}t_{i2}^2 + (j_{max}t_{i1}^2 + 2a_{max}t_{i1} + 2v_{i-1})t_{i2} + \\ 4v_{i-1}t_{i1} + j_{max}t_{i1}^3 + a_{max}t_{i1}^2 - 2\Delta x_i = 0 \\ T_{si} = t_{i1} + t_{i2} + t_{i3} = 2t_{i1} + t_{i2} \end{cases} \quad (11)$$

Uniform acceleration stage's time is represented by t_{i2}. s_{i3}(t) and v_{i3} are feed displacement and speed at t_{i3}.

Eq. (11) can be used to calculate T_{si}.

Similarly,

$$T_w = T_{si} \quad (12)$$

From rotating lift of cam *Tw* and period of interpolation of reciprocating base circle of cam T_0 the rotation speed Ƒ'''' (θ) is calculated as:

$$F''''(\theta) = \frac{T_0}{T_W} \times 36000 = \frac{\frac{1}{600}}{T_w} \times 36000 = \frac{60}{T_w} \quad (13)$$

With this all the acceleration modes are simplified into two acceleration modes.

The feeding acceleration curve and the lift are determined with the help of linear model for the prediction of the rotation of cam.

Once this mathematical model is established a fuzzy control is developed.

The membership function is selected to be a triangle function. The cam's rotation speed curve is modelled and optimized.

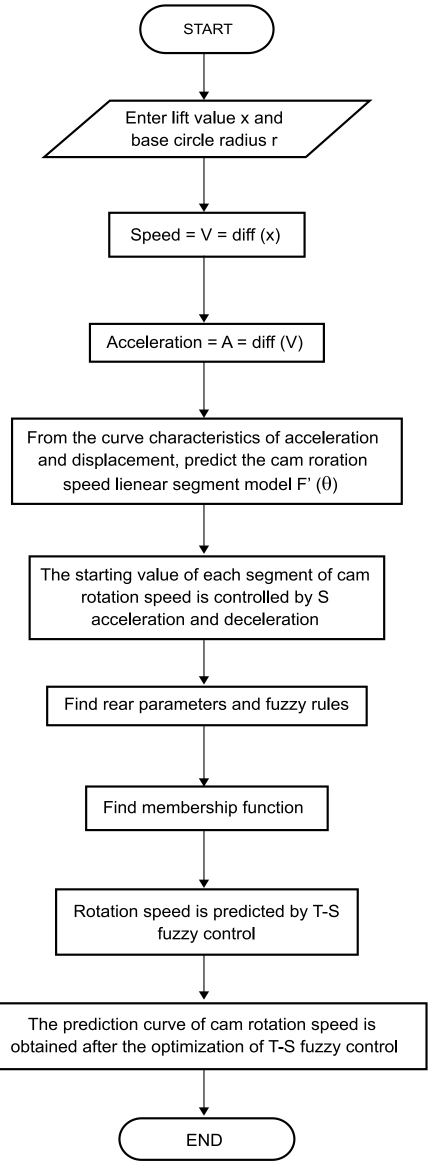

Figure 4: Algorithm representing the process of prediction of rotation speed of cam.

2.2 Grinding's Intelligent Control System

A very intelligent control system for spindle surface grinding machine is proposed here. A schematic of such a control system, which is very intelligent, is shown in Fig. 5.

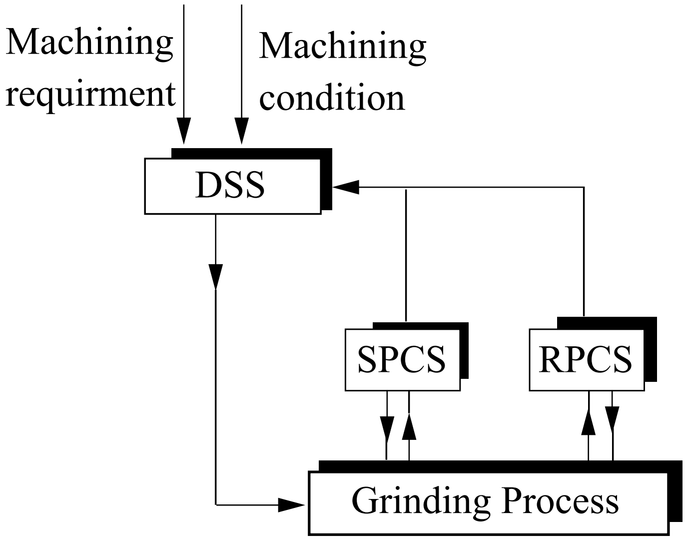

Figure 5: Intelligent control systems schematic diagram [4].

In this process the user enters all the data including workpiece material, dimensional accuracy, machining conditions, spindle type, dimensional accuracy, surface roughness, etc. into DSS.

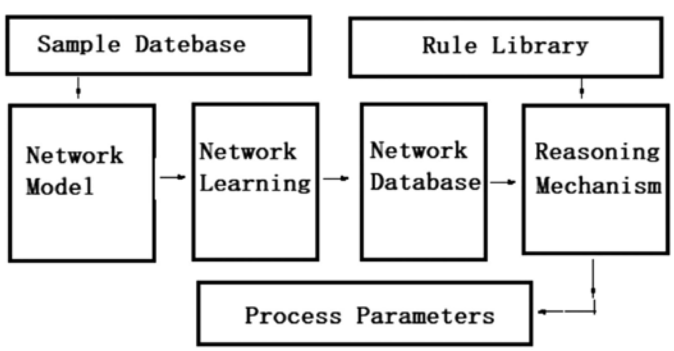

Figure 6: Grinding process parameter DSS construction [4].

A Decision Support System (DSS) is an intelligent system that selects optimal grinding parameters from its expert's library depending on the data provided.

One of the most crucial features of a workpiece is its size. Before the spark-out stage, we construct a size prediction control system (SPCS) to regulate the deformation and size accuracy of workpieces. As shown in Fig. 7, the size prediction control system (SPCS) is made up of three subsystems: deformation control, size prediction, and fuzzy control. In the deformation control subsystem, the optimal adaptive control approach is employed, whereas in the size prediction subsystem, the Elman network with memory is used. First, the grinding parameter decision support system (DSS) determines the best V_f and u for the grinding operation and applies them. Second, the size prediction subsystem is subjected to t (n-1), t'(n-1), t"(n-1), u(n-1) and V_f(n-1). Then t_p(n) can be calculated and fed into subsystem of fuzzy control. The error e and the error change rate e_c can then be calculated using the formulas below:

$$t'_{(n-1)} = t_{(n)} - t_{(n-1)} \quad \text{---(16)}$$
$$t''_{(n-1)} = t_{(n)} - 2t_{(n-1)} + t_{(n-2)} \qquad (14)$$

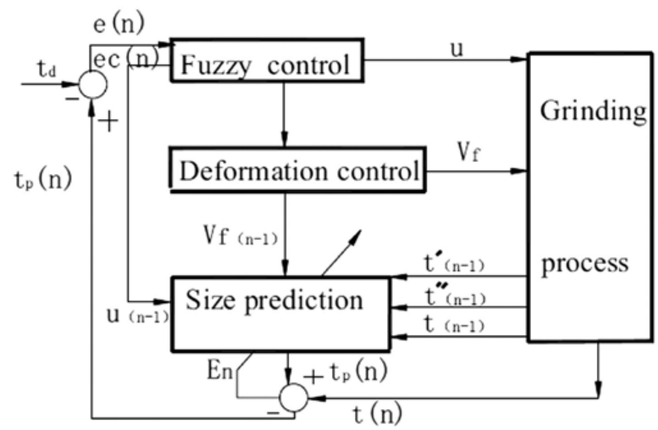

Figure 7: Schematic Diagram of Size Prediction Control System (SPCS) [4].

In the step of spark-out, control of roughness is mostly implemented.

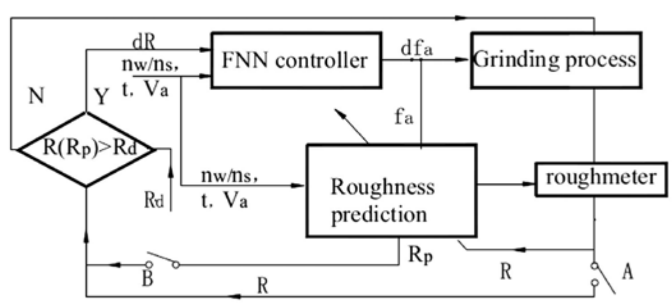

Figure 8: Schematic Diagram of Roughness Prediction Control System (RCPS) [4].

The controller is comprised of a fuzzy neural network (FNN), a prediction subsystem of prediction of surface roughness, and a measurer of roughness. The surface roughness prediction subsystem is a fuzzy neural network-based intelligent system. The amount of workpiece removed is equal to t, the amplitude signal of grinding vibrate is Va, the feed of table is fa, the revolution of workpiece is nw, the revolution of grinding wheel is ns, the roughness that is measured is R, the subsystem for output's prediction of roughness is Rp, the roughness that is desired is Rd, and the change in roughness is dR in Fig. 8. We start by turning on A and turning off B. The rough meter measures the surface roughness of the workpiece and compares it to the desired roughness. The above data is fed into the subsystem for prediction of roughness as the training data of neutral network of fuzzy. As the amount of train data increases, so does the prediction subsystem's accuracy. Switch B is turned on and switch A is turned off when the prediction accuracy meets the criterion. The prediction subsystem of roughness is activated. If roughness does not meet standards, the FNN controller restarts the grinding process. The above-mentioned procedure cycle is repeated again and again until the roughness that is desired is obtained.

2.3 Remote Control's Effectiveness for a Machine of Surface Grinding

It has been observed that automation helps increase effectiveness. Studies conducted on remotely controlled machine have shown that these processes are way more time efficient and provide much more dimensional accuracy. Surface Grinding can also be improved by using a remotely controlled mechanism following a path planned by the operator. To plan a path the operator uses a CAD-based software such as AutoLISP of AutoDesk Co. A semiautomated feature for remotely controlled surface grinding is added to the machine. This basically develops a Man-Machine Interface (MMI).

The MMI works in the following steps:

Firstly, a path that has to followed is designed on the CAD software. The machine uses this path as a guide. This path is used as an optimum position for the machine to either start or to stop. The machine can follow four approaches in terms of directions: a) one-way vertical direction b) two-way vertical direction c) one-way horizontal direction, and d) two-way horizontal direction. For the path designing a relative coordinate system is used rather than an absolute coordinate system. Since the relative coordinate system, when displayed on the computer screen of the machine is difficult for the operator to understand, it has to be converted into absolute coordinate system to make it user-friendly. The Relative Coordinate System can be changed into Absolute Coordinate System by two methods: a) coordinate transposition and b) angle rotation. Coordinate transposition is found by comparing the distance between basis points of both the coordinates. In Eq. 15, dX denotes the distance in horizontal plane and dY denotes the distance in vertical plane. The value of X and Y are obtained using the GPS. Similarly, the angle rotation is found by calculating the angle θ between the axis of both the coordinates. The angle is also estimated using the GPS. After finding the coordinate transposition and angle rotation, their values are fed in the following two equations to convert relative coordinate system to absolute coordinate system:

$$\begin{aligned} Xr &= (x-dX)\cos(\theta) - (y-dY)\sin(\theta) \\ Yr &= (y-dY)\sin(\theta) + (x-dX)\cos(\theta) \end{aligned} \quad (15)$$

During the operation, the actual position of the spindle of the machine is located using a GPS. The data of the GPS is compared with the data of the path planned on the CAD software. This helps us to verify whether the machine follows a controlled path or not. In case the spindle deviates from the planned path during grinding the remotely controlled machine brings it back to the planned path. Actually, the trajectory of the spindle of grinding machine is being displayed on the computer screen, where it is being compared with the actual path. In this way the operator can make certain decisions to make the machining process precise and keep the system controlled.

Once the grinding process is completed the spindle returns back to its starting position.

Even if the most accurate GPS is used there might still be some error left. This might affect our dimensional accuracy a bit, but still, it is negligible. This machining process accompanied by remote control and path planning from GPS data provides much more dimensional accuracy than a simple spindle surface grinding machine.

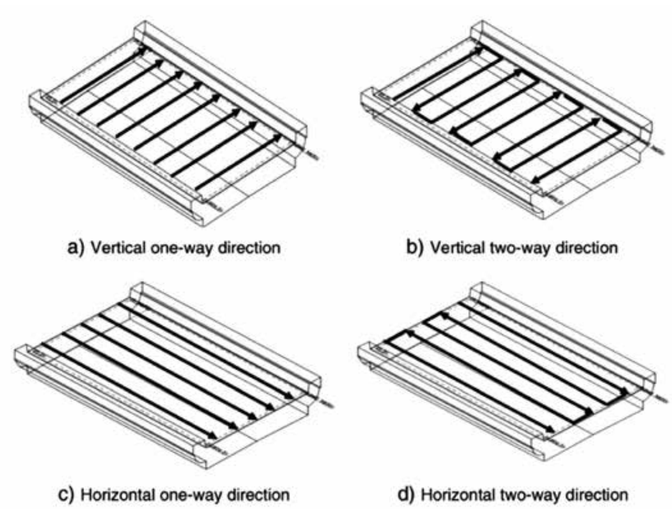

Figure 9: Movement direction in surface grinding [3].

2.4 Study of Control Organization's Study along with the Analysis of Performance for a Top Surface Grinding Machine

The system of control for a top surface grinding machine is now described, which is based on a Programmable Logic Controller (PLC). A brief description of PLC is show in Fig. 9.

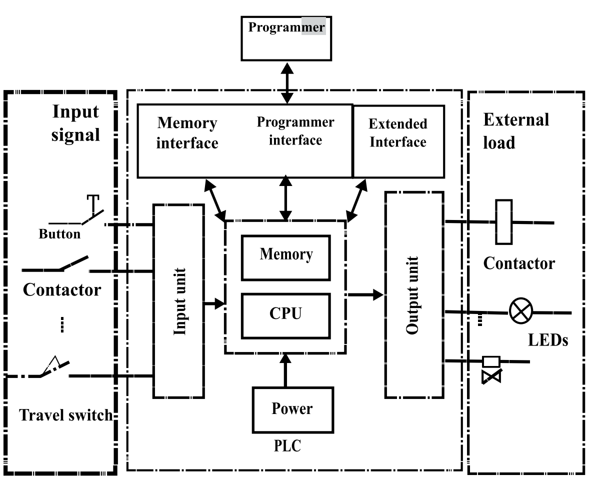

Figure 10: Working principle and composition Programmable Logic Controller (PLC) [7].

Grinding with precision is done on a machine equipped with units of mechanical and a controller. The machine comprises of chucks that is being mounted on an indexing table that firmly grips the workpiece under consideration while it is being operated. Two induction motors are used to rotate these chucks. Variable frequency drives control the speed of these motors.Initially, input pieces are added into the system through the belt of conveyor controlled by solenoid valves. The process of grinding is then divided into two phases: the pre-finishing phase and the finishing phase. Both of these phases use a similar grinding technique; the only difference is that the grinding wheels used at each station are different. The working principle of grinding consists of grinding wheels that are mounted on a spindle that is revolving, the motion of which is controlled by servo motors and sensors. The parts that operate the servo motor in the grinding system are known as servo drives. By continuously monitoring the feedback signal from the servo mechanism, a servo drive adjusts for variations from desired performance. This drive accepts a commanding signal from a system of control, then makes it amplified, after that sends servo motor an electric current to generate some sort of motion proportionate to the commanding signal. Some sensors of proximity are therefore installed; they provide input on the slide's movement. To grind, both the workpiece holding chuck and the grinding wheel spin. In-process gauging is performed during grinding at both stations, allowing the machine to impulsively adjust to the parts fluctuating length. Self-gauging of the workpiece is done, along with measured values are provided as a data for the system to control the machine for grinding purposes, provides for exact grinding of the workpiece. Human Machine Interface is connected to PLC and displays the information for operator there. The operator can make control decisions on the basis of this information. For this, the operator gives commands to PLC logic through HMI which in turn controls the system.

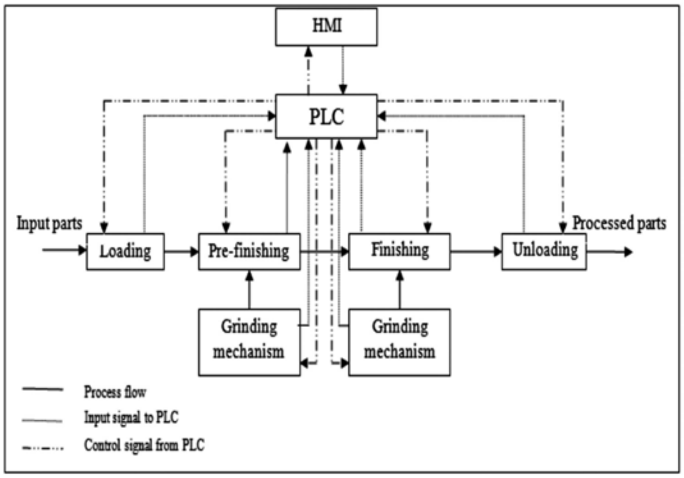

Figure 11: Schematic of control organization of surface grinding machine [7].

3. PROPOSED APPROACH

Control System of Compliance Feedback in Grinding for Part Parallelism

Certain models of grinding have indeed been developed for the sole purpose of planning trajectory in the vertical direction in order to improve vertical compliance. . Parallelism might improve if the track was followed in an open loop, according to numerical simulations. To increase the parallelism and provide a superior surface finish, a control system for feedback force and power are being used. However, there are some disadvantages in this open loop manner. The forces in grinding fluctuate greatly, the function of open-loop ramp becomes impossible to predict. Another drawback of the control system for open-loop function is that the path for each type of workpiece must be specified separately. This approach, however, can certainly be improved by setting the control system in a closed-loop manner. The method, discussed in this article, depends mostly on constantly changing the depth of cut of workpiece to accommodate for machine compliance fluctuations.

The force of vertical grinding force is measured with the help of a dynamometer. To track the projected deflection of the wheel, a tracking controller is utilized. The following section outlines the basic methodology, which is trailed by the evaluation of the compliance of machine, an investigation of the stability of system, an explanation of the facilities, and experimental procedure, along with the outcomes.

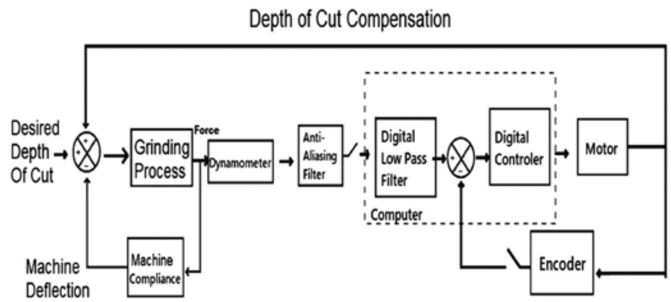

Figure 12: Controller's block diagram.

3.1 Compensation Methodology

It is known that grinding force and material removal rate have a direct relation. However, the material removal rate is inversely proportional to the cut's depth. So, force of grinding can reduce by decreasing the depth of cut. Another factor that effects the grinding force is the contact area among grinding wheel and workpiece, the more the area, the greater the force and vice versa. Since all the above-mentioned factors fluctuate during a machining process, the grinding force may vary owing to machine compliance. This lowers the finished workpiece's parallelism.

3.2 Compliance Modelling

Fig. 12 shows the block diagram of a controller which comprises of table of machine and the both compliances i.e., that of grinding wheel and the spindle's compliance. Here two models have been used to model compliance. The initial method involved bringing down a stationary grinding wheel over the workpiece and carrying out measurement of force produced using dynamometer. Fig. 13 shows the graph of the resulting connection as a dotted line. Here a compliance value of 7.1 x 10^{-5}mm N^{-1} was given in the form of a line equation as x = cmF.

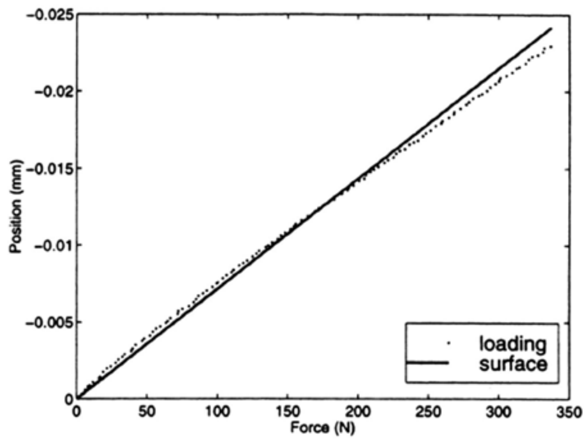

Figure 13: Measured compliance [1].

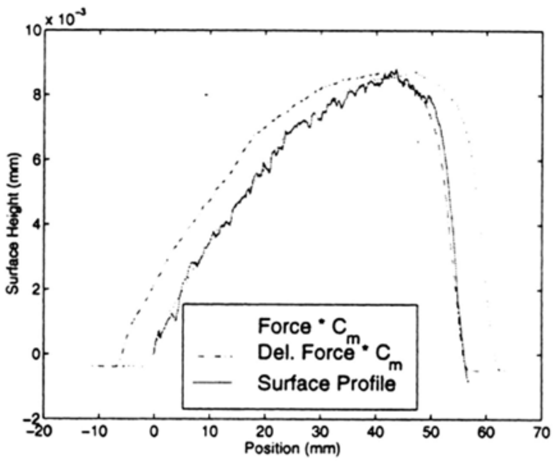

Figure 14: Force profile relationship. 0.0254 mm (0.001 in) nominal depth of cut. 762 (30 in min-1) feed rate. 7.31 x 10^{-5} mm N^{-1} compliance. The workpiece was a 57.15 mm (2.25 in) diameter 1018 steel cylinder [1]..

One method of measuring the machine's compliance independently was to correlate the force measured with the surface profiled workpiece. For the experiment, only the front half of the grinding wheel was run over the workpiece. Fig. 14, that depicts the relationship between surface profile and grinding force, clearly illustrates the surface profile that is measured by an LVDT by a solid line. Both the inside and the outside force lines indicate the wheel's edges of the wheel at the time the force was measured. A delayed force is produced by the inside edge. Compliance of Machine has been used to scale the force. About 21 experiments for numerous rates of feed and cut's depth, the value of compliance was determined to be 7.17 x 10^{-5}mm N^{-1} using the method least squares minimization of the surface that was being observed and the force that was scaled due to compliance.

3.3 Analysis of Stability

When a control system loop is used, the steady system of grinding can become wobbly. Therefore, to make the system stable, we have to adjust the cut's depth. The feed in horizontal direction is mostly the primary feed. The force generated by this feed is

$$F = \frac{AV_f}{K_g'} d_c \tag{16}$$

Here V_f, V, d_c, A, K'_g represent the rate of feed,velocity of the grinding machine's wheel relative to workpiece under observation, depth of cut, contact's area among the workpiece and grinding wheel of the grinding machine, and constant of proportionality respectively. The feed owing to raising the depth of cut is the other direction of feed. This feed direction produces a force of

$$F = \frac{A}{K_g V} \dot{d}_c \tag{17}$$

Here, $\dot{d}_c$ and K_g represent the rate at which the feeding of wheel into the workpiece is done and the proportionality constant, respectively. Now the transfer function is given by

$$\frac{F(s)}{d_c(s)} = \frac{A}{K_g V} s + \frac{AV_f}{K_g' V} = K_c(Rs+1) \tag{18}$$

$$where\ R = \frac{A}{K_g V} and\ K_c = \frac{AV_f}{K_g' V} \tag{19}$$

Grinding stiffness is what the term Kc stands for. A second-order dynamic function with effective mass m, effective stiffness k, and the effective damping co-efficient b is now employed for stability analysis. In Fig. 15, K_f represents the positive feedback gain and T is the first-order filter with constant time. The depth of cut and force in this model can stated in the form a relationship as transfer function as:

$$G(s) = \frac{K_c K_f (Rs+1)(Ts+1)(ms^2+bs+k)}{a_0 s^3 + a_1 s^2 + a_2 s + a_3} \tag{20}$$

$$where \quad a_0 = K_f T_m - K_c R_m$$
$$a_1 = K_f(m + bT) + K_c(R(K_f T - b) - m)$$
$$a_2 = K_f(b + kT) + K_c(R(K_f - k) + K_f T - b)$$
$$a_3 = kK_f + K_c(K_f - k)$$

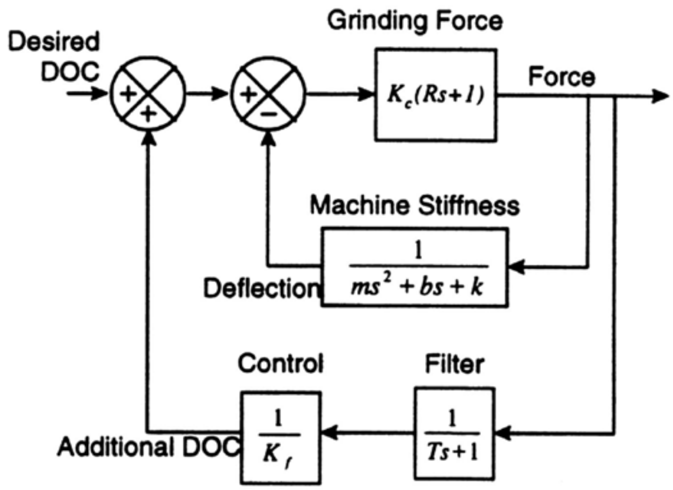

Figure 15: Model for stability analysis of grinding system [1].

Table 1: Parameters calculated through experiments

k	2.1 x 10^4 N m^{-1}
b	0.78 Ns m^{-1}
m	1.2 x 10^{-4} Kg
K_c	1.5 x 10^4 N mm^{-1}
T	0.044 s

For the control scheme to work and to get a positive value for a3, Kf is set approximately k. Also, for stability requirements we require positive a0. This causes Eq. (19) to become as follows:

$$\frac{A}{K_g V} < kT \qquad (21)$$

Another stability requirement for depends on the size of R. In this requirement there is a condition that $a1$ must always be positive.

Assuming k>>m and k>>b.

The limit on K_c as R approaches zero is determined by

$$\frac{K_c}{K_f} < 1 + \frac{bT}{m} \qquad (22)$$

Another requirement for stability is have a positive $a2$ as well as a positive $a_1a_2–a_0a_3$ term. This leads to equation where

$K_f = k$.

$$\frac{K_c}{K_f} < \frac{bT}{2m}\left(1 + \sqrt{\left(1 + \frac{4m}{bT}\right)}\right) \qquad (23)$$

Various parameters in Table 1 were found experimentally.

3.4 Experimental Procedure

To verify the controller's capacity, twenty-one experiments were conducted with two distinct workpiece materials at varying feed rates and depths of cut. One of the workpieces was a 1018 steel cylinder with a diameter of 57.15 mm (2.25 in) while the other was a 4015 steel cylinder with a diameter of 49.0 mm (1.93 in). A vertical spindle surface grinding Computer Numerical Control machine was used for testing purposes.

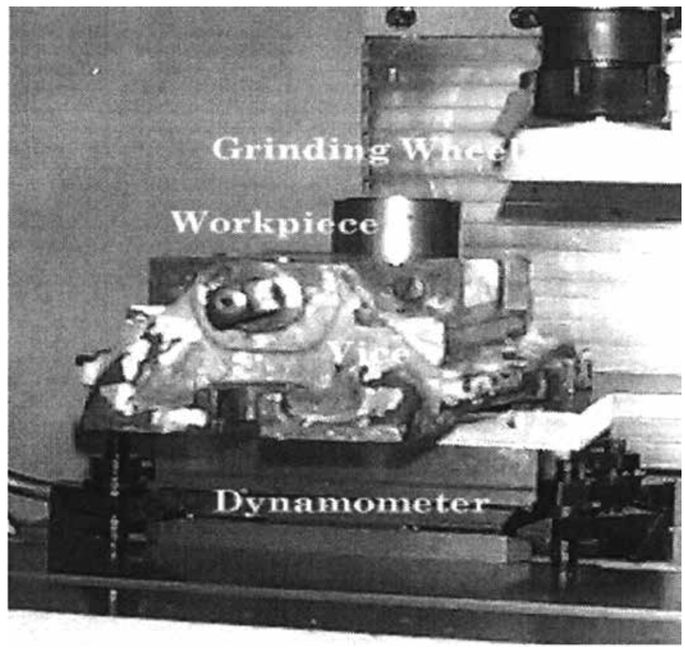

Figure 16: Setup configuration of grinding [1].

Figure 17: LVDT measuring surface profile of ground workpiece [1].

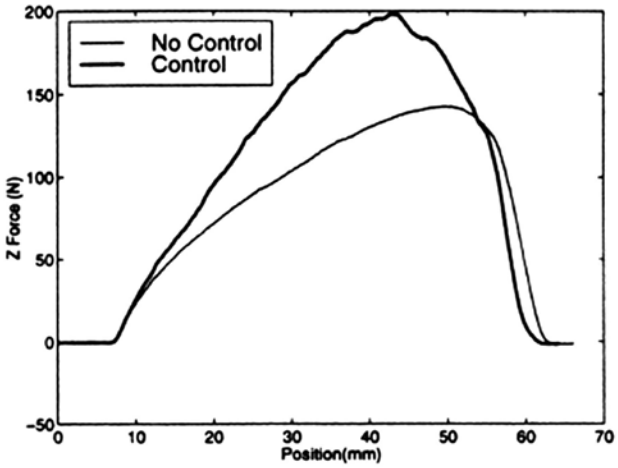

Figure 18: Comparison of measured force with respect to position with and without control. For second workpiece, depth of cut was 1016 mm min^{-1} (40 in min^{-1}), 0.0254 mm (0.001 in), spindle speed was 3000 r.p.m. [1].

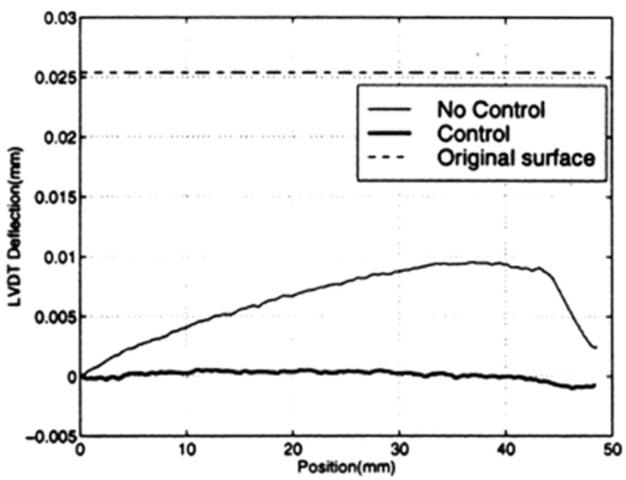

Figure 19: Improvement in surface profile with respect to LVDT Deflection and Position. For second workpiece, depth of cut was 1016 mm min^{-1} (40 in min^{-1}), 0.0254 mm (0.001 in), spindle speed was 3000 r.p.m. [1].

Tool path for closed-loop control system at a set feedrate is provided by commercial CNC machine tool controllers. This specified path, however, can just be selected off the path and will show no reaction to fluctuating cutting situations or the input sensor receives while machining. As a result, the circuitry of controller (Bridgeport Troq-Cut 22) utilized in the research was upgraded for the machine tool to be controlled by an external PC controller. For each and every axis of the grinding machine, a switch for multipole rotary was added. This switch can convert the output from the matching motor's encoders from being sent into the controller circuitry to being fed through an outside port of the grinding machine. The switch operated a relay, which switched the motor input from the controller circuitry's amplifier to an additional changing amplified breadth of pulsation. The input of amplifier's signal came from the similar outer connection. An external computer with a controller card may control the machine axis by axis using this port. Many other sensors can be read with the machine built in this way, for the sole purpose of monitoring process and improve the control system by giving extra information. For example, using the dynamometer to measure the force and using the force to derive the trajectory. The controller may also be utilized to synchronize position, force, and LVDT readings.

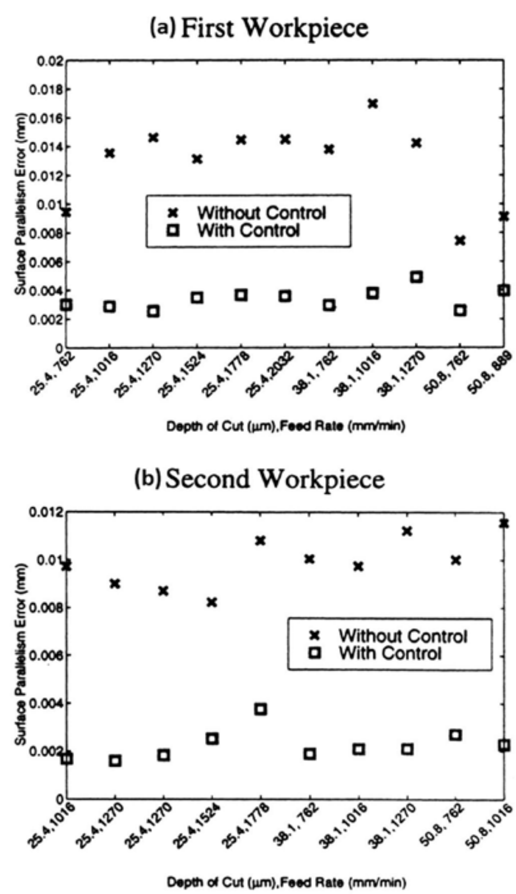

Figure 20: (a)Parallelism's comparison of first workpiece with and without control with respect to depth of cut and feed rate

(b)Parallelism's comparison of first workpiece with and without control with respect to depth of cut and feed rate [1].

Fig. 18 depicts force measured under control and without any control. The peak grinding force increases as the depth of cut increases, as expected.

Fig. 19 depicts an example of workpiece parallelism enhancement under the influence of control. As the grinding wheel exits the workpiece, the control system becomes more effective. Before this point the grinding wheel exits the workpiece, control system becomes greatly effective. This is due in part to the shifting cutting dynamics that occur when only the rear of the wheel removes material rather than the entire cup rim. The phase delay in the force measurement filter, which occurs when the wheel leaves the component and the force quickly changes, is another element to consider. Fig. 20 (a) and (b) depicts the resulting surface parallelism at various cut depths and feed rates. As the rate of feed and rate of material removal enhanced, so did parallelism enhance. In general, a surface having less error in parallelism error were obtained for the controlled workpiece, and with minimum accumulation on grinding wheel during the process of grinding.

First workpiece when controlled, the improvement in parallelism in terms of average was 72.5 % and for controlled second workpiece was 77.3 %. Surface Parallelism's improvement for first workpiece was greatly affected the material removal rate. Both had an inverse relation. Second workpiece's improvement falls as both feed rate of feed and the cut's depth rise. Similarly, when rate of material removal increases, the overall increase decreases.

4. METHODOLOGY

Grinding machine's functional capabilities, control systems, and peripheral process monitoring equipment have all improved during the last 20 years. Process enhancement technologies such as touch detection, wheel balancing, and in-process gauging may be incorporated into higher-end grinding machines based on customer requirements. The achievable single pass tolerances in vertical spindle surface grinding are frequently restricted by machine compliance and also the grinding wheel. The approach presented here involves precisely altering the depth of cut during grinding to maximize dimensional precision. It also resulted in a significant improvement in the quality of surface grinding.

A technique for controlling surface parallelism during the grinding process is offered by altering the depth of cut. Grinding wheel and machine compliance usually restrict single-pass tolerances in vertical spindle surface grinding. The proposed approach entails precisely changing the depth of cut during grinding to improve dimensional precision without the need for additional spark out passes. The correction is made in this situation based on the expected deflection from the simulated compliance as well as the observed vertical force.

Surface grinding's goal is to remove material quickly while maintaining the ideal workpiece size and form. The efficiency of surface grinding is mostly determined by the depth of cut (DOC). In surface grinding, the amount of grinding force is critical. A large depth of cut will result in a strong grinding force. Grinding chatter, burns, and exploding grinding wheels are all possible outcomes of unvaried grinding force. The variation of normal grinding force is seen in a surface grinding operation due to the unevenness of the component surface or of the grinder wheel. Also, increased depth of cut control may increase grinding force. Only a lesser average Force can be applied to the part surface to avoid scorching the work piece or injuring the grinder. If the grinding force is controlled to a constant value, the system will be able to achieve stability. The construction of the models and design of the controllers in this thesis is based on several key principles and results from control theories. For instance, transfer function, root locus, and so on. A transfer function is a mathematical depiction of the relationship between an LTI (linear time-invariant) system's input and output.

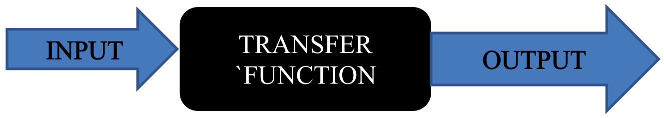

The Laplace transform is a valuable mathematical tool that helps solve and evaluate linear differential equation models with less effort. The root locus is the path traced out in the s-plane by the roots of the characteristic equation as a system parameter (usually a gain) is modified.

A method for enhancing surface parallelism in vertical spindle cup grinding is described in this paper. The strategy focuses on actively changing the depth of cut to compensate for the system's fast deflection. A dynamometer is positioned between the workpiece and the machining table to measure the vertical grinding force. Based on an off-line system compliance model, this force component is utilised to anticipate system deflection. The deflection is then tracked in real time using a tracking controller. When compared to when no control is employed, the approach provides a surface with reduced parallelism error. As a result of the feedback force control, the finished product has better consistency and tolerances.

The system's block diagram is provided by

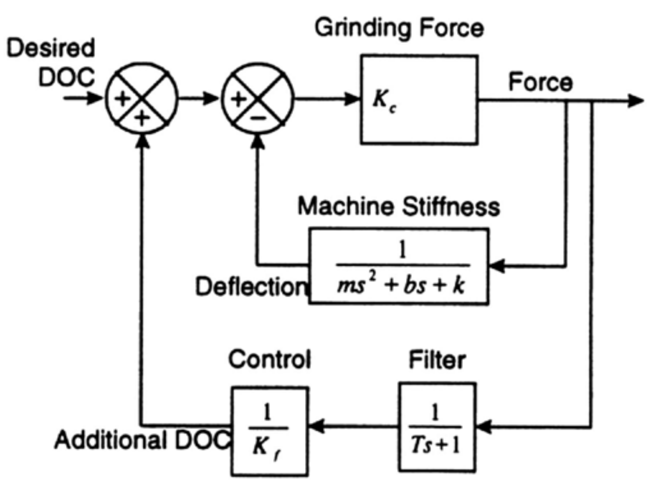

Figure 21: Block diagram of grinding system

The transfer function which was derived in the approach Compliance Feedback Control for Part Parallelism in Grinding is given by

$$G(s) = \frac{K_c}{1\,\frac{K_c}{ms^2+bs+K} - \frac{K_c}{K_f}\left(\frac{1}{Ts+1}\right)}$$

$$G(s) = \frac{K_f K_c(ms^2+bs+k)(Ts+1)}{K_f(ms^2+bs+k)(Ts+1) + K_f K_c(Ts+1) - K_c(ms^2+bs+k)} \quad (24)$$

$$G(s) = \frac{K_f K_c(ms^2+bs+k)(Ts+1)}{K_f(mTs^3+(bT+m)s^2+(kT+b)s+k) + K_f K_c(Ts+1) - K_c(ms^2+bs+k)}$$

Here K_c represents grinding stiffness, m represents effective mass, b represents effective damping coefficient, k refers to effective stiffness, T refers to time constant and K_f represents positive feedback gain.

From experiments, the measured values of the unknown parameters are

$K_c = 1.5\times10^4$ N/mm
$K_f = 1410$
$m = 1.2\times10^{-4}$ kg
$b = 0.78$ Ns/m
$k = 2.1\times10^4$ N/m
T = 0 004 s

Substituting the values of parameters in Eq. (24), our transfer function becomes,

$$G(s)=\frac{10152s^3+68526000s^2+1793097000000s+444150000000000}{0.007448s^3+46.7604s^2+222839.8s+2250000} \quad (25)$$

The block diagram is then reduced, using Eq. (25), as follows

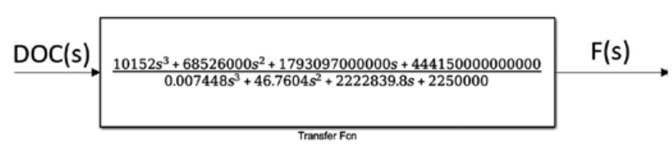

Figure 22: Reduced block diagram

This transfer function is converted into state space using MATLAB. Converting from state space to transfer function is straight forward since the transfer function form is unique. It's more harder to convert from transfer function to state space, owing to the wide number of state space forms that may be used to represent a system. The following is the code that was used for this:

Code 1: Transfer function

```
clc
clear all
close all
s=tf('s')
G=((10152*(s^3))+(68526000*(s^2))+(1793097000000*s)+444150000000000)/((0.007448*(s^3))+(46.7604*(s^2))+(2222839.8*s)+2250000)
Gss=ss (G) % this command is used to convert transfer function to state space.
```

The result obtained is as follows:

```
s =

s

Continuous-time transfer function.

G =

 10152 s^3 + 6.853e07 s^2 + 1.793e12 s + 4.442e14
  ----------------------------------------------
  0.007448 s^3 + 46.76 s^2 + 2.223e06 s + 2.25e06

Continuous-time transfer function.

Gss =

A =
             x1          x2          x3
   x1      -6278  -1.822e+04        -144
   x2  1.638e+04           0           0
   x3          0         128           0

 B =
            u1
   x1  2.621e+05
   x2          0
   x3          0

 C =
             x1          x2          x3
   y1      2453  -3.866e+04   1.077e+05

 D =
            u1
   y1  1.363e+06

Continuous-time state-space model.
```

5. IMPLEMENTATION

The suggested grinding force controller is designed in MATLAB and verified in Simulink in this thesis. The following is a basic description of MATLAB and Simulink. MATLAB is a computer language used in scientific computing. It provides an intuitive interface that combines computation, visualisation, and programming with problems and solutions written in standard mathematical notation. Simulink is a MATLAB-integrated software tool for modelling, simulating, and analyzing dynamic systems. It provides a graphical environment in which dynamic systems can be designed, simulated, implemented, and tested.

Now the control system is tested with different types of inputs and is verified.

5.1 Step Input

The block diagram of step input is given by

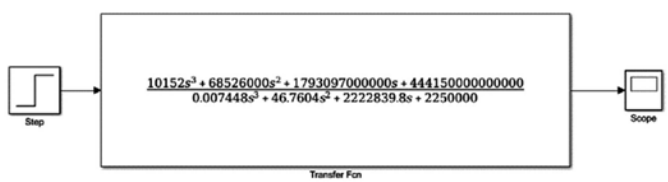

Figure 23: Block diagram of step Input

The graph of step input is given by

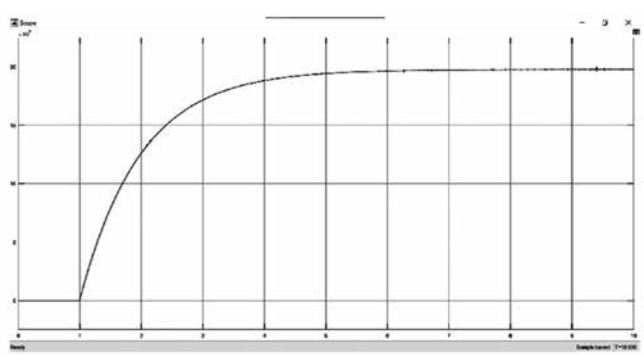

Figure 24: Graph of step input

From the graph, it is clearly observed that the system is quite stable. There are no overshoots in the system. The system gives a very good response to the step input. The graph shows that the system achieves stability after 6s. The system stays stable once the stability is achieved. This is indeed a good system.

5.2 Ramp Input

The block diagram of ramp input is given by

Figure 25: Block diagram of ramp

The graph of ramp input is given as

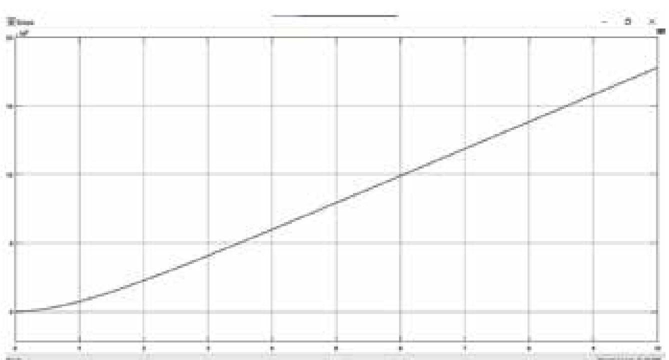

Figure 26: Graph of ramp

The ramp function is a one-dimensional unary real function with a ramp-like graph. The name "ramp" can also refer to various functions that are created by scaling and shifting, and the unit ramp function is the one discussed in this article (slope 1, starting at 0). The ramp function is also known as the positive portion in mathematics. The control system in the case follows the ramp in a quite good manner. This verifies that the system is a good system.

5.3 Parabolic Input

The block diagram of parabolic input is given as

Figure 27: Block diagram of parabolic input

The graph of parabolic input is given by

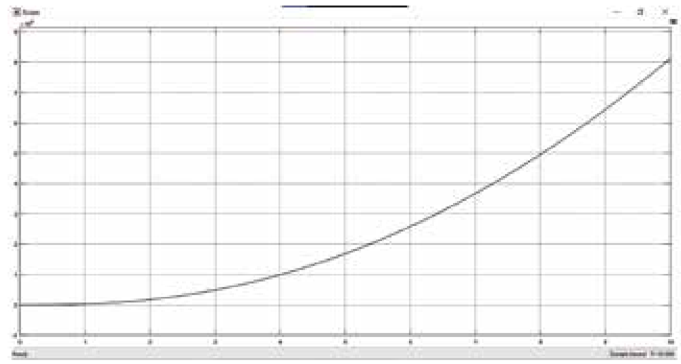

Figure 28: Graph of parabolic input

A signal is characterized as a parabolic signal or parabolic function when it gives a continuous acceleration differentiation from the real input signal. Unit acceleration signal is another name for it. At t = 0, the unit parabolic signal begins. Once again, the system follows a parabolic path without any disturbance in the system. Thus, it is evident that this is a good system.

5.4 Stability

The gain of the system is varied to check the stability of the system at various gains. This can also help the user to vary gains according to their needs. The transfer function of the system is given by

$$G(s) = \frac{10152s^3 + 68526000s^2 + 1793097000000s + 444150000000000}{5.28 \times 10^{-6} K_f s^3 + [0.003444K_f - 1.8]s^2 + [1584.78K_f - 11700]s + [22500K_f - 3.15 \times 10^6]}$$

Here K_f is the gain. Now to check the range of gain, K_f Routh Table is used.

The system's characteristic equation is provided by

$$5.28 \times 10^{-6} K_f s^3 + [0.003444K_f - 1.8]s^2 + [1584.78K_f - 11700]s + [22500K_f - 3.15 \times 10^6]$$

Now the Routh Table is given as

Table 2. Routh Table

s^3	$5.28 \times 10^{-6} K_f$	$1584.78K_f - 11700$
s^2	$0.003444K_f - 1.8$	$22500K_f - 3.15 \times 10^6$
s	$5.28 \times 10^{-6}[22500K_f - 3.15 \times 10^6] - [1584.78K_f - 11700][0.003444K_f - 1.8]$	
1	$22500K_f - 3.15 \times 10^6$	

It is necessary to do the following in order to get positive numbers in the first column:

$5.28 \times 10^{-6} K_f > 0 \Rightarrow K_f > 0$
$0.03444K_f - 1.8 > 0 \Rightarrow K_f > 52.26K_f$
$22500K_f - 31.5 \times 106 > 0 \Rightarrow K_f > 1400$
$[1584.78K_f - 11700][0.03444K_f - 1.8] - 5.28 \times 10^{-6}[22500K_f - 31.5 \times 10^6] > 0$
or
$54.52K_f^2 - 402.48K_f - 2852.6K_f + 21060 > 0.1188K_f^2 - 166.32K_f$
$54.4K_f^2 - 3088.76K_f + 21060 > 0$
or

$K_f^2 - 56.8K_f + 387.1 > 0$

or
$(K_f - 7.92)(K_f - 48.88) > 0$
So either $K_f < 7.92$ and $K_f < 48.88 \Rightarrow K_f < 7.92$
or >7.92 *f K* and >48.88⇒>7.92

The fourth row stipulates the most dominant condition.

We now conclude requiring $K_f > 1400$.

5.5 Steady State Errors

As time goes to infinity, the steady-state error is the difference between the desired and actual value of a system output in the limit (i.e. when the response of the control system has reached steady-state). In this situation, the steady state errors are as follows:

$$\lim_{s \to 0} G(s) = \frac{4.4415 \times 10^{14}}{2250000} = 197.4 \times 10^6$$

$$e_{step(\infty)} = \frac{1}{1 + \lim_{s \to 0} G(s)} = \frac{1}{1 + 197.4 \times 10^6} = 5.066 \times 10^{-9}$$

$$e_{ramp(\infty)} = \frac{1}{\lim_{s \to 0} sG(s)} = \frac{1}{0} = \infty$$

$$e_{parabola(\infty)} = \frac{1}{\lim_{s \to 0} s^2 G(s)} = \frac{1}{0} = \infty$$

Hence, from the above calculations, it is evident that the error in step input is negligible and that the errors in ramp and parabola are infinity.

5.6 Root Locus

By varying system gain K from zero to infinity, the Root locus is the location of the roots of the characteristic equation.

The root locus of the system is calculated using MATLAB and the graph of the root locus obtained is as follows:

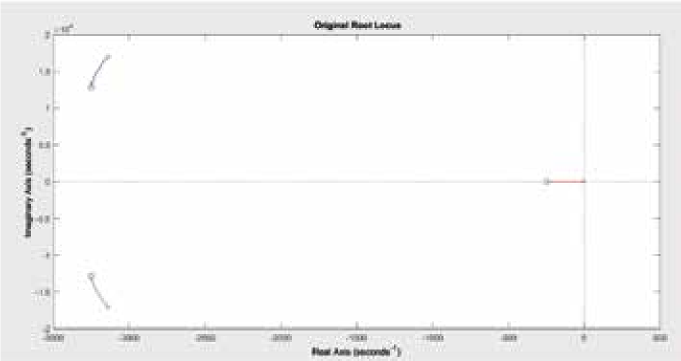

Figure 29: Root locus of system

The MATLAB code of root locus is given by:

Code 2: Matlab code for root locus

```
clc
clear all
close all
s=tf('s')
G=((10152*(s^3))+(68526000*(s^2))+(1793097000000*s)+444150000000000)/((0.007448*(s^3))+(46.7604*(s^2))+(2222839.8*s)+2250000)
rlocus(G)
```

The graph shows that all of the system's poles and zeros are located on the system's left half plane, indicating that the system is stable. One of the poles is quite close to but not at the origin, indicating that the system is extremely stable. The system becomes unstable if the poles are in the right half plane.

The controller's resilience to disturbances and parameter modifications should be determined since it remained stable across a wide range of settings.

6. RESULTS

The transfer function of the system which is shown in Eq. (25) was in third order.

$$G(s)=\frac{10152s^3+68526000s^2+1793097000000s+444150000000000}{0.007448s^3+46.7604s^2+222839.8s+2250000}$$

To solve the system easily and to find its characteristics, it is reduced to second order system using MATLAB using balred command.

$$G(s)=\frac{2.665 \times 10^6 s^2+6.264 \times 10^{10} s+1.555 \times 10^{13}}{s^2+7.781 \times 10^4 s+7.7876 \times 10^4} \quad (26)$$

Upon resolving the system to second order, its rise time, settling time, natural frequency and damping frequency can easily be found.

For this system Settling time Comes out to be 0.00876s

Rise time comes out to be 0.0158s

$\omega_n = 3.943 \times 10^6$
$\zeta = 7.99428 \times 10^3$

Since the value of ζ is greater than 1, our system is overdamped.

The MATLAB code used for finding the above parameters is as follows:

Code 3: For finding parameters

```
clc
clear all
close all

num=[10152 68526000 1793097000000 444150000000000];
den=[0.007448 46.7604 2222839.8 2250000];
G=tf(num,den);
T=balred(G,2)
 G1=feedback(T,1);
  [numt,dent]=tfdata(G1,'v');
omegan=sqrt(dent(3))
  zeta=dent(2)/(2*omegan)
```

The system's response without any controller was as follows

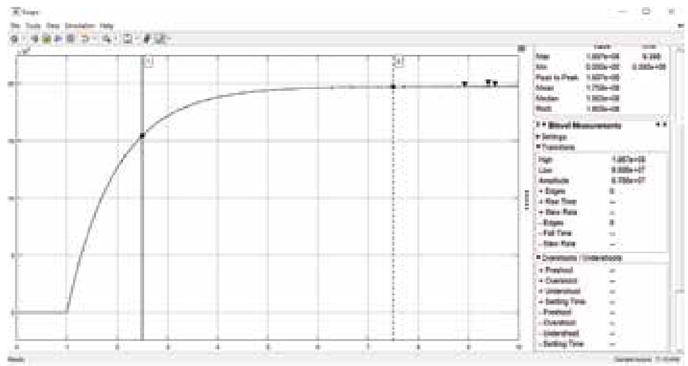

Figure 30: System's response without any controller

A controller is a component in a control system that attempts to close the gap between a system's actual value (i.e. the process variable) and its desired value (i.e. the setpoint). All modern control systems need controllers, which are an integral aspect of control engineering.

Controllers may be used for a number of different purposes, such as:

- By minimizing steady-state error, controllers increase steady-state accuracy.
- Improvement of steady-state accuracy leads to improvement of stability.
- Furthermore, controllers assist in the eradication of unneeded offsets in the system.
- Controllers can be used to regulate the system's maximum overrun.
- Utilizing controllers can serve to minimize noise signals in a system.
- An overdamped system's delayed response can be sped up by using controls.

When the plant's performance isn't matching the system's standards, a closed loop control system, rather than a new plant, might be beneficial. The controller was derived from the difference between the actual and necessary outputs. This controller, in turn, causes the plant to take the appropriate corrective steps, bringing the actual output closer to the desired one.

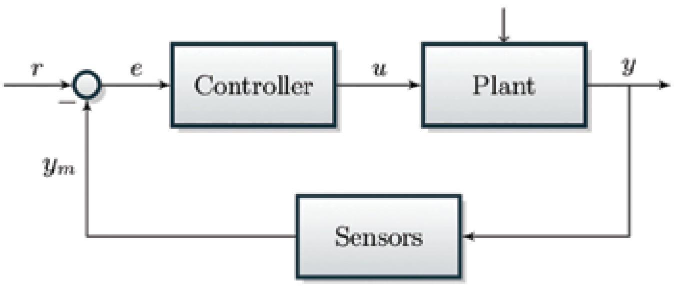

Figure 31: Schematic of a controller

Errors are of two types

- Transient Error
- Steady State Error

The most basic way is to create an actuating signal u proportionate to the error, with the actuating signal's magnitude growing as the error grows. This allows the real output to correspond to the required output. This is the proportional controller. This controller is beneficial when the error is below a specified threshold. If the error exceeds a certain threshold, a proportional controller is insufficient to handle it.

The plant's reaction to the input when it is applied is delayed as a result of the reluctance. When the gain of the proportional controller is increased to reduce the delay, the controller overshoots, resulting in oscillations at the output. A transient error is what it's called. It's now time to think about how much the rate of change in error has changed as a result of the control operations.

Overshoot and oscillatory behavior can be regulated if the rate of change of error at the point of crossing the final value is utilized to manage the plant's output. The derivative controller is based on this concept. This controller should be used with caution when the signal contains noise, which is very typical. The noise is amplified by the derivative controller, which causes the plant to become unstable.

However, because to some intrinsic constraints, the plant may never reach the designated point. The steady state mistake is the result of this. For detecting this steady state error, the integral of the error will yield a superior response. The steady state error can then be reduced using the error integral. An Integral controller is based on the concept of employing a constant error across time. This controller improves the plant's performance in noisy environments.

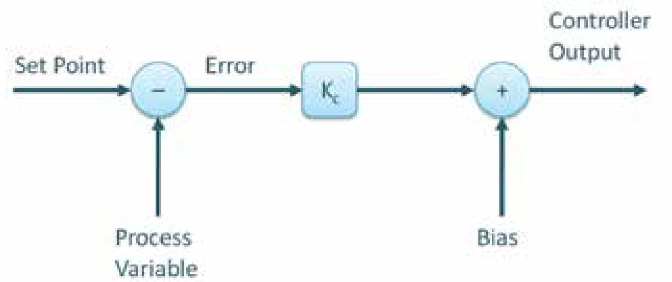

Figure 32: Schematic of P controller

To reduce the rise time and increase response speed, a proportional controller is used. The phase response of the plant is not influenced by this controller.

Here K_p=25

The graph of the system is plotted using Simulink on MATLAB

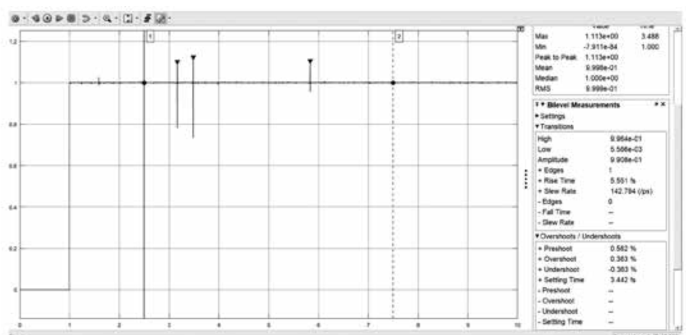

Figure 33: System's response with P controller

6.1 PI Controller

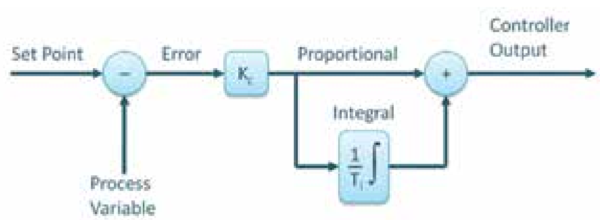

Figure 34. Schematic of PI Controller

This comes in handy when proportional control is needed to speed up settling and integral control is needed to decrease error that is constant throughout time. PIC (Proportional Integral Control) is a controller type (PI controller). The rising time and steady state errors of a system can be reduced with the use of a PI controller. When you need to modify magnitude and phase at the same time, this tool will come in helpful.

Here K_p= 25

K_i = 20

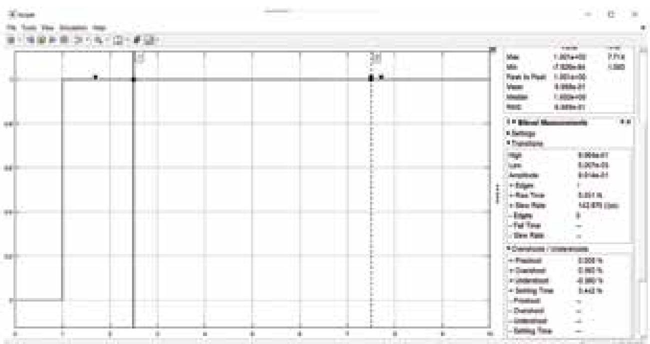

Figure 35: System's response with PI Controller

6.2 PID Controller

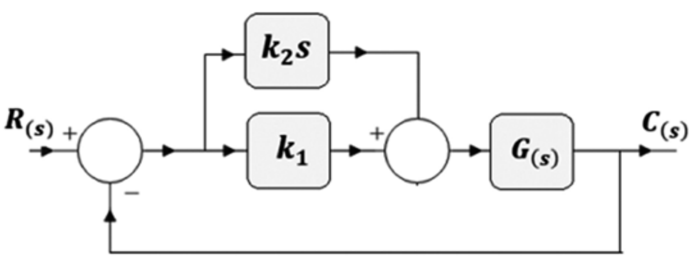

Figure 36: Schematic of PD controller

In practice, no one controller is capable of completing the job. Many controllers must work together to meet the criteria. When we need to speed up the transient time, we utilize proportional control, and for overshoot and oscillation difficulties, we use derivative control. As a result, a proportional-derivative controller is required (PD Controller). The signals must be noiseless; otherwise, the derivative actions would exacerbate the noise, causing the plant to lose stability. The PD controller reduces output transients such rising time, overshoot, and oscillations. This is handy when altering magnitude and wishing to add phase led to the output.

Here K_p= 25

K_d = 0.00001

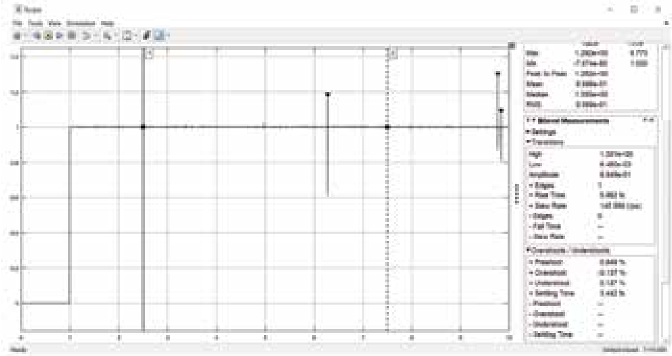

Figure 37: System's response with PD controller

6.3 PID Controller

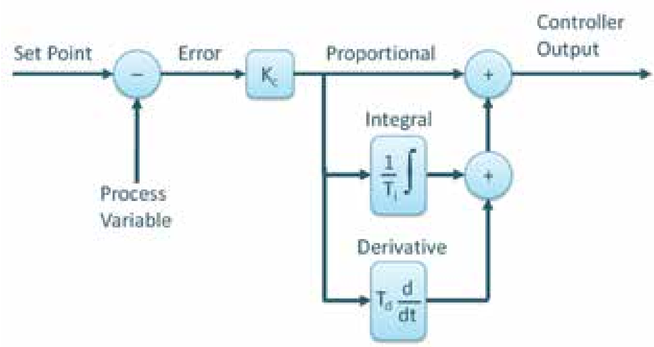

Figure 38: Schematic of PID controller

Solving all of the difficulties listed above with a single solution is a more broad example. In this case, all three controllers are utilized in conjunction with appropriately determined gains. By changing these gains, any combination of P, I, D controllers may be obtained, resulting in a more robust controller. A PID controller is a type of controller that may be applied to a wide range of applications. By modifying the gains of the three control actions, any controller may be created. This wide type of controller may produce a magnitude change as well as a lead or lag in phase in the output.

Here K_p= 25

K_i = 20

K_d = 0.00001

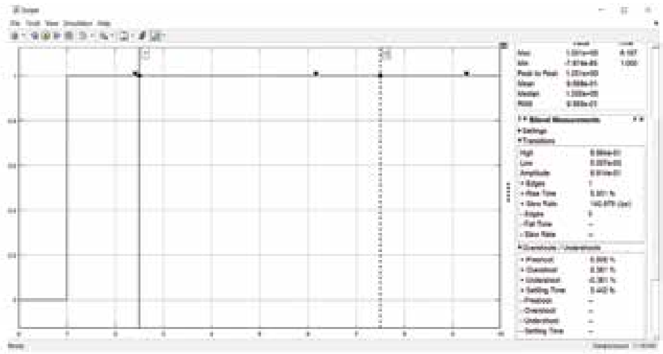

Figure 39: System's response with PID controller

7. CONCLUSION

Grinding classification is a common complicated system, and regulating the grinding and classification system for automated concentrators has proven to be a challenging and time-consuming operation. Grinding classification is a critical component of the mineral processing industry's production processes and product size management, and its effects have a direct impact on the quality and efficiency of flotation concentrate product recovery operations. As a result, using advanced intelligent control technology to ensure its product size qualified premise of improving grinding and classification production efficiency, lowering production costs for enterprises to improve beneficiation economic efficiency and market competitiveness in the grinding and classification process has significant practical significance.Control of unattended production processes and machinery, as well as automatic counselling to inexperienced employees, are becoming increasingly important in today's manufacturing environment. This research looks at the design and performance of an autonomous process controller for traverse grinding, with an emphasis on decreasing chatter vibration-induced waviness on the machined surface. This was accomplished by employing a range of model-based wheel regeneration chatter monitoring and mitigation tactics, which has been highlighted as the most challenging problem to handle in big industrial roll grinding machines during roughing and semi-finishing processes. Low labor skills, a labor scarcity, and poor quality can all have a negative impact on operational performance when it comes to surface grinding. A method for enhancing surface parallelism in vertical spindle cup grinding is described in this paper. The strategy focuses on actively changing the depth of cut to compensate for the system's fast deflection. A dynamometer is positioned between the workpiece and the machining table to measure the vertical grinding force in this method. Based on an off-line system compliance model, this force component is utilised to anticipate system deflection. The deflection is then tracked in real time using a tracking controller. The technique produces a surface with less parallelism error as compared to when no control is used. To demonstrate the compensating technique, grinding tests were carried out. The results demonstrate that the approach is effective at a variety of feed rates and cut depths. The most noticeable parallelism gain is around five times, with effectiveness dropping somewhat when the federate and cut depth were increased. Parallelism was improved in all circumstances, with a minimum of a 50% improvement. The findings of this study open up the possibility of improving machine tolerance or throughput by minimizing the number of sparkout passes required.

8. RECOMMENDATIONS

A surface grinder's principal function is to remove material from a flat surface in order to finish the workpiece to the desired size and finish with a fine surface finish. They're also used to sharpen cutting tools, grind small flanges, as well as large cylinder blocks, machine bases, and a variety of other products. Any engineering industry would be incomplete without a Surface Grinding Machine. Your machine has gotten more accurate and productive since CNC Controls were introduced. Surface Grinding Machines are necessary in every business, whether it is the car, consumer goods, or machine tool manufacturing.

To support the exploitation of the solution industry, the controller can be upgraded by adding more diagnostic functions to control the mechanical confusion that may interfere with control functions. In addition, speeding operations should include not only the stability of the cutting process, but also other technical limitations and competency features such as roughness and appearance, as well as the production and cost of the entire system. The controller can also be customized to work with various grinding machines due to the flexibility of the design.

REFERENCES

[1] Hekman, K. A., & Liang, S. Y. (1999). Compliance Feedback Control for Part Parellelism in Grinding. The International Journal of Advanced Manufacturing Technology, 15(1), 64–69. doi:10.1007/s001700050040 J. Clerk Maxwell, A Treatise on Electricity and Magnetism, 3rd ed., vol. 2. Oxford: Clarendon, 1892, pp.68–73.

[2] A. K. Srivastava and M. A. Elbestawi, "Control strategy formultipass robotic grinding", International Journal of Robotics andAutomation, 10 (3), pp 114–119, 1995

[3] Moon, S., Yang, B., Kim, J., & Seo, J. (2010). Effectiveness of remote control for a concrete surface grinding machine. Automation in Construction, 19(6), 734–741. doi:10.1016/j.autcon.2010.03.001

[4] Ning, D., Jingsong, D., Chao, L., & Shuna, J. (2019). An Intelligent Control System for Grinding. 2019 IEEE 3rd Information Technology, Networking, Electronic and Automation Control Conference (ITNEC). doi:10.1109/itnec.2019.8729268

[5] Manoj Kumar,Jyoti Raman,Priya Priya , "Particle Swarm Optimization: Intelligent Neural Network System (PSOINNS) Based Multi-Objective Optimization of Surface Grinding Operations" , International journal of materials forming and machining processes;2334-4563; vol.2; no.1; p.54-87, 2015

[6] X. Shuqin, "Application of PLC in Computer Numerical Control Machine", International Conference on Industrial Electronics and Applications (IEA), 2015.

[7] Shital A. Dhatrak, Vitthal J. Gond, "Study of Control Organization of a Top Surface Grinding Machine with its Performance Analysis", International Research Journal of Engineering and Technology, 2016.

[8] Li, Y., & Zhou, S. (2018). Sensorless balance method for the spindle system of computer numerical control gear grinding machine. Measurement and Control, 002029401880271. doi:10.1177/0020294018802715

[9] Shih YP and Chen SD. A flank correction methodology for a five-axis CNC gear profile grinding machine. Mech Mach Theory 2012; 47: 31–45.

[10] Yue C, Ren X, Yang Y, et al. Unbalance identification of speed-variant rotary machinery without phase angle measurement. Shock Vib 2015; 2015: 11.

[11] LUO Fuyuan,YOUYoupeng,YIN Juan. Research on the Algorithm of NURBS Curve Bidirectional Optimization Interpolation with S-type Acceleration and Deceleration Control [J].Chienes Journal of Mechanical Engineering,2012,48(5):147-156

[12] S.Bououdena, M.Chadlib,H.R.Karimic.An ant colony optimizationbasedfuzzy predictive control approach for nonlinearprocesses[J].Information Sciences,2015.4(299):143-158

[13] Mukherjee I, Routroy S. "Comparing the performance of neuralnetworks developed by using Levenberg–Marquardt and Quasi-Newton with the gradient descent algorithm for modelling a multipleresponse grinding process". Expert Systems with Applications, vol.39,No.3,pp.2397-2407, 2012.

[14] Jiang, X., Guo, M., & Li, B. (2017). Active control of high-frequency tool-workpiece vibration in micro-grinding. The International Journal of Advanced Manufacturing Technology, 94(1-4), 1429–1439. doi:10.1007/s00170-017-1015-5

[15] Chen F, Liu G (2017) Active damping of machine tool vibrations and cutting force measurement with a magnetic actuator. Int J Adv Manuf Technol 89:691–700

[16] Guo M, Li B, Yang J, Liang SY (2016) Influence of dynamic force on vibration of micro-machine tool spindle. Proceedings of the International Conference on Advanced Materials, Structures and Mechanical Engineering, 217–222

[17] Parenti, P., Leonesio, M., & Bianchi, G. (2016). Model-based adaptive process control for surface finish improvement in traversegrinding.Mechatronics,36,97-111. doi:10.1016/j.mechatronics.2016.04.001

[18] Michael, E. H. C., & Andre, B. D. (2017). Development of Control System for Vibratory Grinding Process. Procedia Engineering, 174, 1093–1099. doi:10.1016/j.proeng.2017.01.262

[19] Li, Y., & Zhou, S. (2018). Sensorless balance method for the spindle system of computer numerical control gear grinding machine. Measurement and Control, 002029401880271. doi:10.1177/0020294018802715

[20] Yixu, S., Hongjun, Y., & Hongbo, L. (2013). Intelligent Control for a Robot Belt Grinding System. IEEE Transactions on Control Systems Technology, 21(3), 716–724. doi:10.1109/tcst.2012.2191587

[21] WANG, H., LIU, J., DUAN, H., PAN, Y., ZHANG, Z., & YUE, S. (2019). Prediction Method of Rotation Speed of Workpiece on Camshaft Grinding Machine based on T-S Fuzzy Control. 2019 IEEE 3rd Advanced Information Management, Communicates, Electronic and Automation Control Conference (IMCEC). doi:10.1109/imcec46724.2019.8983936

VELOCITY CONTROL USING TORQUE INPUTS TO THE MOTOR OF A TEXTILE CROSS-LAPPER MACHINE

Authors: Abdullah Nadeem[1] , Dr. Syed Irtiza Ali Shah[1], Sheikh Muhammad Ammad[1], Malik Muhammad Awais[1]
[1]Department of Mechanical and Aerospace Engineering, Air University Islamabad, Pakistan
190574@students.au.edu.pk (Abdullah Nadeem), 190590@students.au.edu.pk (Sheikh Muhammad Ammad)

Received: 16-April-2022 / Revised: 15-July-2022 / Accepted: 15-July-2022
Karachi Institute of Economics and Technology || Technology Forces Journal, Volume 4, Issue 1, 2022

ABSTRACT

The main purpose of our research is to present modeling and control of a nonwoven textile cross lapper machine. The cross lapper machine is primarily based on pulley block structure mechanism order to make consistent web having suitable width and thickness. This is achieved mainly by pulleys' reciprocating motion for moveable rack system. The mechanism is based on attaining stable speed for carriages while moving back and forth. In this way the machine has ability of stopping at precise re-entry position during reciprocating process. Traditionally, systems inherit a large attenuation of the input; thus, systems tend to be sluggish. However, the system possesses stability. The significance of this study is to present a realizable controller and to discuss the corresponding properties of a dynamic system for controlling horizontal type cross-lapper machines. This not only deals with the achievement of meaningful design objectives but also makes the closed-loop system efficient for good tracking properties. This study is primarily focused on theoretical analysis, aiming to dynamically arrive at a model which can mathematically express the functioning of a cross- lapper machine. The nonlinear dynamic equation for the system is driven by applying the Lagrange equation. During the controller design phase, first the high order transfer function of the linearization system is obtained. Then, a corresponding system having a transfer function of lower order is reached by the application of an approximation criterion with the primary goal of having the analysis; and thus the effort of design is minimized. The control system design involves the application of pole-placement design, in addition to realizable proportional and integral control through state feedback. Application of this model is an initial step towards designing a controller working on a closed loop principle, a moveable rack determining speed and position simultaneously. The importance of such work is that, with the help of a vigilant input system, steady state errors will come to an end and outclass oriented tracking properties will be obtained. The final result of our research is to achieve a dynamic mathematical model through which overall stability of the system is ensured. This control scheme would also meet the needs for the engineering process of the card web, would reduce the vibration of the cross lapper machine, and in turn, the dynamic overloading is also reduced.

Keywords: Cross - Lapper Machine, Torque.

1. INTRODUCTION

There has been very rapid growth in non-woven products in the polymer industry during recent years. This is due to their wide application and as non-woven goods are being widely consumed in a variety of applications, including but not limited to textile, biomedical, and geo-technical engineering. The production process for non-woven products can be further subdivided as web finishing, web reinforcing, and web manufacturing. In view of this importance, in recent years, a number of studies have begun to examine the effect that web needle piercing and the subsequent completion process have had on the material of an uncircumcised product.

As illustrated earlier, non-woven fabrics have wide application areas as their goods are being used in numerous fields, not limited to medical treatment industries and daily necessities. The nonwoven fabrics are manufactured through a continuous process involving passing cotton fibers through a cross lapper, a card, and a needle punch in order to be processed into nonwoven fabrics. The nonwoven cross lapper machine is used in to-and-fro motion after carding. This process necessitates the consistency of reciprocal motion as it is necessary for the overall physical properties of nonwoven fabrics. Usually, cross lapper machines are mainly of two different categories, i.e., vertical and horizontal types. The vertical cross-lapper machine type uses gravity for the falling of the card web, and then layers of the web are made by a swinging arm. In the process of the to-and-fro motion of the vertical cross lapper machine, air resistance makes it become a non-uniformed broken web. From the complete mechanical structure of the vertical cross lapper type machine, its height arises as a problem due to the increased width of card web, which results in a longer swing arm. Therefore, the vertical type machines have already been replaced by the cross- lapper machines of the horizontal type as the preferred nonwoven cross-lapper machines for mainstream production, which have a to- and-fro motion on a movable rack. Stadnik applied the Lagrange's equation in order to derive the mathematical model of the traditional horizontal type cross-lapper machine and applied the optimization of driving torque for simulation of the reversal motion. Moreover, Kou implemented the Hamilton's Principle, also known as Newton's second law, for deriving the cross-lapper machine's mathematical model.

Due to the need for the conveyor belt high speed motions of card web and in order to overcome the classical problems of broken up production, mainly caused by web breakage, for the cross lapper machine's new horizontal type, a double belt layering system has already been designed. Meanwhile, the control of the speed of the machine as well as its position for movable racks is being carried out by a controller having an open-loop and through the use of limit switches, indirectly. However, the resulting web uniformity is inferior, mainly due to the lack of reverse feed info by movable racks. This is a property which is normally available, particularly at the finish points of the movable racks in to and fro motion. The movable racks vibrate under the influence of the inertia force and control the overall lapping of the web.

For a simple model of the control system, the input to the controller is the spinning torque. This shows the amount of power needed to overcome the conflict to move a piece of work through the arc you want. The output of this controller is an angular change in position, which also provides a change in the velocity of the controlled work part. Normally, the controller will compare the control inputs, in this case the spinning torque, to the desired value. This could be a continuous speed or a reference signal generated elsewhere. Converting the spinning torque into an angular area of velocity control is a mechanical or electrical device called an integrator. The simple compiler method takes the maximum amount of input and uses it as a subtraction with minimal delay. This focuses most of its errors on faster exits than accumulated errors over time. In many cases, this works well, especially for applications with low-velocity inputs and slow responses to machine tools such as screw jacks and cross-lapper equipment.

1.1 What does Velocity Mean?

Your idea of speed may be similar to its scientific definition. You know that a large migration in a short period of time means a great deal of speed and that the velocity has sub divisional units, such as miles per hour or KM Per hour. Medium speed is defined as a change in the state separated by travel time.

$$V_{avg} = \frac{d}{dx}\left(\frac{\partial x}{\partial t}\right) \quad (1)$$

1.2 What is Torque

Torque is a quantification of the force which causes an object to rotate about an axis. It is similar to a force that causes an object to accelerate in terms of kinematics, torque is the property that causes an object to attain an angular acceleration. Torque is also known as moment and it is a vector value. The torque vector's direction is mainly dependent on the direction of force about the axis. In daily life the example of opening / closing a door can be utilized for accurate understanding of torque

1.3 Torque can be Static or Dynamic Torque

Vertical torque is one thing that does not result in the production of any angular acceleration. A person who presses a closed door puts static torque on the door as it does not rotate with its hinges, without power input. A person who pedals a bicycle at a constant speed, and uses static torque because it is not fast. The drive shaft in a fast race car from the first lane has a strong torque since it is necessary for production of angular acceleration of its wheels because the car is fast following the track. This is the same thing used in Cross Lapper machines

Keeping in view the theoretical analysis, the research primarily focus on the dynamic derivation of a mathematical model for the latest horizontal cross lapper machine type, and in turn to apply subject model as the initial stage towards design of a closed-loop controller intended to monitor the position along with the speed of movable racks. This would ultimately result in reduction of vibrations, thus, overall consistency for the lapping of web could be enhanced.

2. LITERATURE REVIEW

The invention of the Cross-lapper machine proved to be an absolute blessing for industrialists because it solved the problem of making quilts, pillows, and so on from the time it was invented. The machine has changed many-fold and enormous changes in using basic problem-solving skills also proved useful for the modification process of this machine. Plenty of research papers have been published illustrating the dynamic modeling and control of the subject cross lapper machine, horizontal type, and control of the carriage speed in the cross lapper by adapting various methods. Some examples of such academic and research work independently carried out by prestigious academic institutes are described below:-

2.1 Research carried out by Department of Polymer Engineering, NTUST

During research conducted by graduates of the National Taiwan University of Science and Technology, the problem of input optimization in order to steer an open loop cross lapper was observed. This not only included modeling and cross-lapper machine control, but it also derived the controlling mechanism for the system's inputs. As a result, the control criteria for an accurate time optimization control for the cross lapper system were proposed in order to follow the required cross rack velocity profile with a preset damping ratio and the un-damped natural frequencies. The derived controller was aimed so that it could minimize time for settling of cross-lapper moveable rack velocity by lowering power consumption while moving. Such a control approach is achieved by manipulation of input to the servomotor, which drives the lower pulley, and therefore, driving of the carriage by utilization of the driving belt can therefore be implemented with ease. This paper achieved the goal of deriving a mathematical formula as well as the development of a tool for computation that could lead to the design of a controller for real time.

2.2 Research carried out by Intelligence Control and Simulation Laboratory

Another study conducted by Taiwan's National University of Science and Technology on the dynamic modeling and control of the current horizontal cross lapper machine revealed that the width and web thickness required for the finished product are dependent on the control of constant movable racks steady velocity. Deliberations for the latest cross-lapper horizontal type machine were infrequent in the studies.

Therefore, this paper introduces the model and deliberates the corresponding elements of the cross-lapper machine's new horizontal type system. The compact order system of the controller design was formed with a rating scale, and its understanding was confirmed. Both parallel and inaccessible controls, as well as the design of the pole-bearing in response to the state, have been used to build a control mechanism. The controls can result in a solid speed of moving rack having high-quality tracking positions and can abolish fixed position errors. The consistent velocity of a moving rack may ensure web consistency and maintain machine performance. Similarly, the cross-lapper is usually operated by microprocessors. The control system will fulfill the requirements of the process for web card engineering, reduce machine oscillations, and reduce power overload.

3. MATHEMATICAL MODELING

The mechanism of a cross-lapper machine of the horizontal type is illustrated by Fig. 1. A movable rack with a motor drive system is its major component. The movable rack system consists of a conveyor belt supported by a pulley, which is present for transferring the web to the roller module of the movable rack. A positive torque is exerted by the motor drive system on the transmission pulley in order to tug the rack along with the conveyer belt. Through rollers' rotation along with racks' movement, it reaches the re-entry point in order to attain the desired width.

The servo motor is the main source of torque for the rotation of the transmission pulley in order to reach the re-entry position with the assistance of the conveyor belt. The horizontal type of cross lapper machine is initiated-continual movement at constant speed, with reversal of re-entry point, positioning at another turn around re-entry point, to and fro motion to keep the racks at a stable speed, allowing line to travel by the roller module of the movable rack in order to fold up in a Z–shaped pattern and layer the final web into the specified thickness and width.

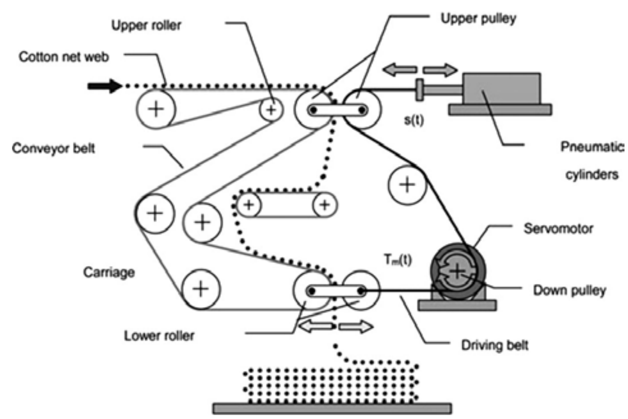

Figure 1: Working mechanism for the new cross-lappe r machine of horizontal type [21]

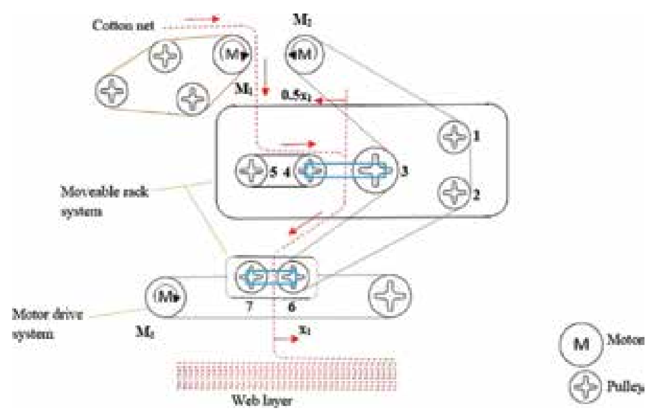

Figure 2: Current new horizontal type cross lapper [22]

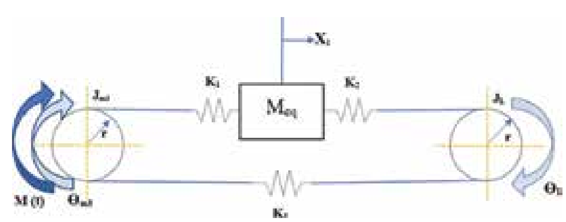

Figure 3: Equivalent design for new cross lapper of horizontal types [2]

3.1 System of Movable Racks

Movable racks, conveyor belt and the pulley get their driving power from motor for taking the web towards the mobile rack through roller module for the complete process of the web. The kinetic energy for this system is expressed as T1 and is shown as [23]

$$T_1 = \frac{1}{2}J_{M_2}\dot{\theta}_{M_2}^2 + \frac{1}{2}J_1\dot{\theta}_1^2 + \frac{1}{2}J_2\dot{\theta}_2^2 + \frac{1}{2}J_3\dot{\theta}_3^2 + \frac{1}{2}J_4\dot{\theta}_4^2 + \frac{1}{2}J_5\dot{\theta}_5^2 + \frac{1}{2}J_6\dot{\theta}_6^2 + \frac{1}{2}J_7\dot{\theta}_7^2 \quad (2)$$

and

$$x_1 = 2r_1\theta_1 = 2r_2\theta_2 = 2r_3\theta_3 = 2r_4\theta_4 = 2r_5\theta_5 = r_{M_2}\theta_{M_2} = r_6\theta_6 = r_7\theta_7$$

where

r_i: the pulley radius i = 1, 2, 3, 4, 5, 6, 7.

θ_i: displacement of the pulley i = 1, 2, 3, 4, 5, 6, 7. J_{M2}: the inertia of the motor equivalent moment M_2. □M2: the motor shaft angular velocity M2.

J_i: the inertia pulley moment i = 1, 2, 3, 4, 5, 6, 7.

□i: the angular velocity for the pulley i = 1, 2, 3, 4, 5, 6, 7.

x_i: the movable rack displacement.

r_{M2}: the motor shaft radius M2.

θ_{M2}: the motor shaft angular displacement M2.

Substituting the values from equation of x_1 into the kinetic energy T_1 comes out to be [23]

$$T_1 = \frac{1}{2}J_{M_2}\left(\frac{\dot{x}_1}{r_{M_2}}\right)^2 + \frac{1}{2}J_1\left(\frac{0.5\dot{x}_1}{r_1}\right)^2 + \frac{1}{2}J_2\left(\frac{0.5\dot{x}_1}{r_2}\right)^2 + \frac{1}{2}J_3\left(\frac{0.5\dot{x}_1}{r_3}\right)^2 + \frac{1}{2}J_4\left(\frac{0.5\dot{x}_1}{r_4}\right)^2 + \frac{1}{2}J_5\left(\frac{0.5\dot{x}_1}{r_5}\right)^2 + \frac{1}{2}J_6\left(\frac{\dot{x}_1}{r_6}\right)^2 + \frac{1}{2}J_7\left(\frac{\dot{x}_1}{r_7}\right)^2 \quad (3)$$

3.2 System for Driving the Motor

For system for driving the motor, the source of both forward and reverse torques is servo motor responsible for the motion of driving belt for pulling the racks that provides velocity and displacement. The corresponding cross lapper machine free-body diagram of horizontal type is illustrated by the Fig 2 above. Three degrees of freedom are possessed by this system, for which the coordinates which are independent are x 1, θ m3, and θ L. This mechanism, has rigid belts for conveying that are provided in static stretch operation. On the other hand, the flexible driving belts having much more elasticity than that of the conveyor belts are used [2].

$$K_1 = \frac{2EA}{L_1 - x_1} K_2 = \frac{2EA}{L_2 - x_1} K_3 = \frac{2EA}{L_3 - x_1} \quad (4)$$

Where the Young's modulus is **E**, the cross-sectional area of the driving belt is A is, the spring initial length is Li is, i = 1, 2 and 3. The kinetic energy for the springs can be expressed as follows [24]:-

$$T_{k_1} = \frac{1}{2}\left(\frac{1}{3}m_{k_1}\dot{x}_1^2\right) T_{k_2} = \frac{1}{2}\left(\frac{7}{12}m_{k_2}\dot{x}_1^2\right) T_{k_3} = \frac{1}{2}\left(\frac{1}{12}m_{k_3}\dot{x}_1^2\right) \quad (5)$$

4. SYSTEM LINEARIZATION

4.1 System Equilibrium Positions

In order to have the horizontal cross lapper machine instate of steady equilibrium, the following conditions need to be fulfilled:-

1. Movable rack velocity $\dot{x}_1 = 0$
2. Linear acceleration $\ddot{x}_2 = 0$
3. Motor Drive System motor axle equivalent angular velocity $\theta_{m3} = 0$
4. Equivalent angular acceleration of motor axle $\theta\theta_{m_{33}} = 00$
5. The load axle Angular velocity is $\theta_L = 0$
6. The load axle angular acceleration is $\theta\theta_L = 0$,
7. Variable input of the angular movement is **M(t)** = 0.

When all the above conditions are attained at the state of stable equilibrium, following equation set is achieved:

$$-\left(\frac{2EA}{L_1 - x_1} + \frac{2EA}{L_3 - x_1}\right) r^2\theta_{m_3} + \frac{2EA}{L_1 - x_1} r x_1 + \frac{2EA}{L_3 - x_1} r^2\theta_L = 0$$

and (6)

$$\left(\frac{2EA}{L_1 - x_1} + \frac{2EA}{L_2 - x_1}\right) x_1 - \frac{2EA}{L_1 - x_1} r\theta_{m_3} - \frac{2EA}{L_2 - x_1} r\theta_L + EA\left[\frac{1}{(L_1 - x_1)^2}(x_1 - r\theta_{m_3})^2 + \frac{1}{(L_2 - x_1)^2}(r\theta_L - x_1)^2 + \frac{1}{(L_3 - x_1)^2}(r\theta_{m_3} - r\theta_L)^2\right] = 0$$

4.2 The Linear Equation of the System

For the new cross lapper machine of horizontal type, the dynamically liberalized equation for system may be written as follow:-

$$\dot{X}_1 = \frac{-1}{M_{eq}}\left\{\left(\frac{2EA}{L_1}+\frac{2EA}{L_2}\right)X_2 - \frac{2EA}{L_1}rX_5 - \frac{2EA}{L_2}rX_3\right\}$$

$$\dot{X}_2 = X_3$$

$$\dot{X}_3 = X_4$$

$$\dot{X}_4 = \frac{-1}{J_L}\left[B_L X_4 + \left(\frac{2EA}{L_2}+\frac{2EA}{L_3}\right)r^2 X_3 - \frac{2EA}{L_2}rX_2 - \frac{2EA}{L_3}r^2 X_5\right] \quad (7)$$

$$\dot{X}_5 = X_6$$

$$\dot{X}_6 = \frac{-1}{J_{m_3}}\left[M(t) - B_{m_3}X_6 - \left(\frac{2EA}{L_1}+\frac{2EA}{L_3}\right)r^2 X_5 + \frac{2EA}{L_2}rX_2 + \frac{2EA}{L_3}r^2 X_3\right]$$

$$Y = X_1$$

4.3 System Controllability

The current cross lapper machine of horizontal type is under control, at a first stage, if it is likely through the utilization of an unrestrained control in order to move the system from any original condition to an alternate estate during a limited time gap. If the system is entirely controllable, then the rank of the controllable matrix at any original given state is equal to **n** i.e.

$$\mathbf{Q_c} = [BABA^2B \ldots A^nB] = \mathbf{n}$$

4.4 Approximation of High-order System through Low-order System

Assuming closed loop transfer function for higher order system is given by

$$M_{high}(s) = k\,\frac{1 + b_1 s + b_2 s^2 + \cdots + b_m s^m}{1 + a_1 s + a_2 s^2 + \cdots + a_n s^n},\ n \geq m \quad (8)$$

The gain k is to remain the same when subjected to zero frequency (direct current) for both transfer functions, to maintain the steady performance of the higher order system into the corresponding lower order system. The state ofdiscovering the low-order Mlow(s) requires under mentioned connection to be fulfilled as straight as possible:

$$M_{low}(s) = k\,\frac{1 + c_1 s + c_2 s^2 + \cdots + c_q s^q}{1 + d_1 s + d_2 s^2 + \cdots + d_p s^p},\ n \geq p \geq q \quad (9)$$

By application of this approximation standard, the transfer function of high order systems may be transformed to corresponding lower order system as expressed in following equation:

$$\left(\frac{2EA}{L_2 - x_1} + \frac{2EA}{L_3 - x_1}\right)r^2\theta_L - \frac{2EA}{L_2 - x_1}rx_1 - \frac{2EA}{L_3 - x_1}r^2\theta_{m_3} = 0 \quad (10)$$

Therefore, open-loop transfer function of the first low-order system is:

$$G_{p\ low} = \frac{z_0}{s + p_0}$$

5. CONTROL SYSTEM DESIGN

Fig. 4 illustrates the realizable design of a proportional and Integral (PI) controller which can mathematically also shown as

$$G_{cl}(s) = K_{P_1} + \frac{K_{I_1}}{s}$$

Then, after adding the controller the closed-loop transfer function is shown in fig3:

$$\frac{Y(s)}{R(s)} = \frac{G_{cl}(s)G_{p\ low}(s)}{1 + G_{cl}(s)G_{p\ low}(s)}$$

$$\frac{Y(s)}{R(s)} = \frac{z_0 K_{P_1}(s) + z_0 K_{I_1}}{s^2 + \left(p_0 + z_0 K_{P_1}\right)s + z_0 K_{I_1}} \quad (11)$$

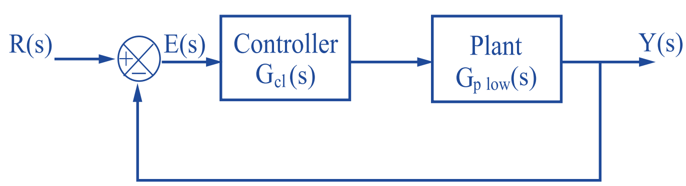

Figure 4: Horizontal cross lapper machine feedback control system [25-26]

The state feedback designs are used for the determination of the necessities with respect to each condition. The feed-back post of each constant gain, variables conditions then additionally change positions of their respective poles for the closed-loop. This methodology of design is employed during the feedback design of various control system operations and is popularly known as the pole placement design. It is pertinent to know that the system condition variables are fully and completely controllable. This means that all pole positions of may be arbitrarily arranged within system.

For the latest cross lapper machine of horizontal type, in the state equation the closed-loop system is determined by reverse feeding condition variables by means of a fixed feedback gain K matrix, as shown in Fig. 4, and is

$$\mathbf{u}(t)=\mathbf{r}(t)-\mathbf{K}\underline{\mathbf{X}}(t)$$

and then (12)

$$\dot{\underline{X}}(t)=(\mathbf{A}-\mathbf{BK})\underline{\mathbf{X}}(t)+\mathbf{Br}(t)$$

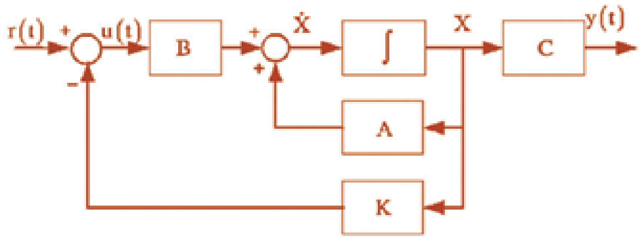

Figure 5: New current lapper machine horizontal type having state feedback

The placement of the poles is designed utilizing concepts of the state feedback. Main design aims determining the gain K matrix feedback which would give the certain prescribed values for all the characteristic values of the closed-loop system. As mentioned earlier, since the states of the system can be fully controlled, therefore, the condition of closed loop system, after designing of the state feed-back, also possess the property of complete controllability. The respective values within BK state matrix defined above may therefore be employed for the gain matrix K. This enables us to determine the pole positions for the controlling the cross lapper machine of horizontal type.

6. SIMULATION RESULTS AND DISCUSSIONS

6.1 Simulation without Controller for Linear and nonlinear System

Fig. 6 and 7 illustrated the linear and nonlinear system models for new cross lapper machine of horizontal type when it is fed with motor angular moment in the form of a unit step and with a sine function as the input. The figures depict the transient responses for the corresponding movable rack velocity of linear as well as the non-linear systems. As illustrated, both responses tend to be sluggish having large errors in their steady state. The achieved results are in cognition with anticipated results there for ere valid ate accuracy of the concept of equilibriumposition.

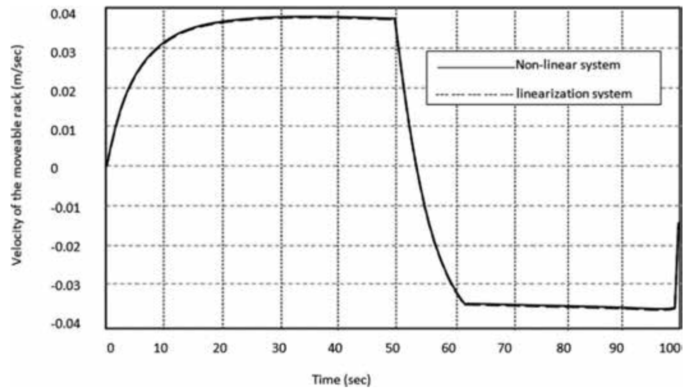

Figure 6: Response of velocity the moving rack with motor torque Inputs

$$\textbf{\textit{unit step}}\ \boldsymbol{u}(\boldsymbol{t})=\begin{cases}\mathbf{1} & \mathbf{0}\le\boldsymbol{t}<\mathbf{50}\\ \mathbf{-1} & \mathbf{50}\le\boldsymbol{t}<\mathbf{100}\end{cases}$$

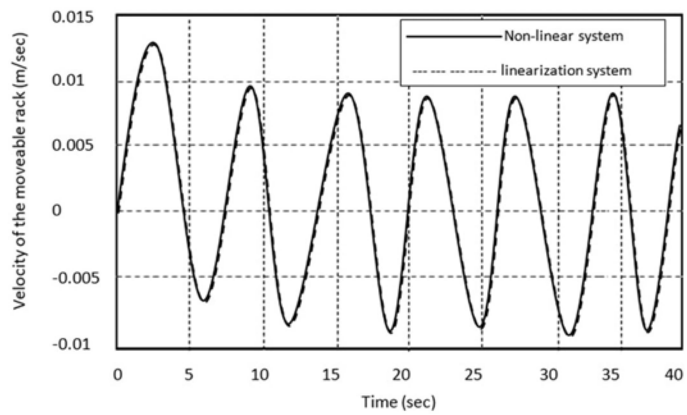

Figure 7: The response of velocity for the moving rack with motor torque input as sine function M (t) = sin t

6.2 Discussion on the open loop system types

An open loop system, commonly known as a non-response system, is a category of continuous control system where the output has no effect or does not affect the control action of the input signal. In other words, in the open source control system, the output is not measured or reversed compared to the input. Therefore, an open loop system is expected to faithfully follow the installation command or set point regardless of the end result. Also, the open system has no knowledge of the release status and therefore cannot correct itself for any errors that may occur when the present value goes up, even if this causes a significant deviation from the pre-set value. Another disadvantage of open-loop systems is that they are well- designed to manage disruptions or changes in conditions that may reduce their ability to complete the task. Such a type of "open-loop motor control" has the inherent advantage of being potentially cheap and simple in its implementation. As a result, such systems are ideal for use in well-defined systems where the input-output relationship is direct and unaffected by external disturbances.

Fig. 5 depicts the velocity response of a moving rack. Input torque is applied to the motor of one of the movable racks and embedded in a feedback loop. It is observed from above Fig. 5 Because the system output displays a nonzero steady state error for the given step input u(t), the open loop system type is Type 0. Therefore, we can say that for the above response of the velocity for the moving rack with motor torque input applied as a unit step, the open loop system has a type of Type 0 system.

6.3 Error in Steady State

Error in the Steady state may be expressed in terms of measure of difference of the desired value from that of actual values. Error in steady state is an inherited characteristic of the ratio of input to output for all linear system. Generally, control system with a low errors of steady state regarded as a good control system. The response of such a transfer function at steady state is shown in Fig . 8. The figure depicts that the output of the system exactly equals the input, when the system is in the steady-state. Hence, the steady-state error for the system is zero.

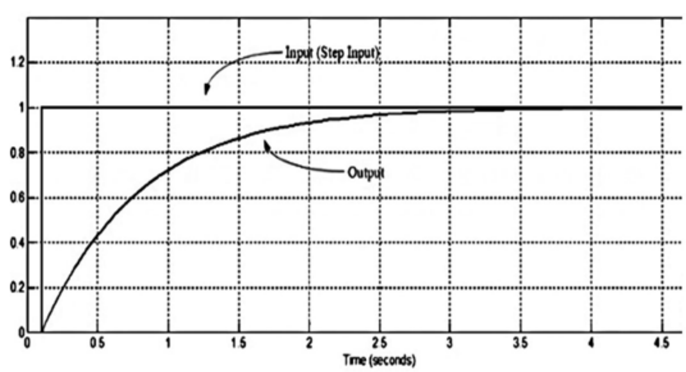

Figure 8: First order transfer function Time response for

$$\boldsymbol{step\ input\ M(t)} = \begin{cases} \mathbf{1} & \mathbf{0 \le t < 40} \\ \mathbf{-1} & \mathbf{40 \le t < 80} \end{cases}$$

From Fig. 5 for velocity response for the moving rack, while input torque is applied to the motor of one of the movable racks and embedded in a feedback loop. The steady state error can be calculated by expression from the basic definition

e(infinity) =input response–output response

Here, the input response is the unit step input and output response is the velocity output response from the Fig. 5. It can be observed from the Fig. 5 that the maximum value of the velocity of the output response for this case obtained must be approximately equal to 0.037 meter per second. By substituting 1 as the input response and 0.037 meter per second for the output response in the basic equation above we can find

e (infinity)=1-0.037=0.963

Therefore, the steady state error obtained is 0.963

6.4 What would be the Steady State Error for the Ramp Input

From Fig. 5 for velocity response for the moving rack, while Torque input is applied to the motor of one of the movable racks and embedded in a feedback loop. The steady state error when the input of the ramp is tu(t) can be expressed as

$$\boldsymbol{e}(\infty) = \frac{\mathbf{1}}{\boldsymbol{K_v}}$$

Where $\mathbf{K_v}$ is the velocity constant,

We know the velocity constant is zero for the ramp input when the Open loop system is Type zero. Therefore $\mathbf{K_v = 0}$ Substituting $\mathbf{K_v = 0}$ in the above relationship the steady state error for a ramp input would be **"∞"**

6.5 Simulation without Controller for the initial Higher-order Linear System along with Reduced System having First-order

The initial high-order equations are reduced to linear system of the first order for the new cross lapper machine of horizontal type. If unit step and sine functions are made as the inputs of a motor torque, transient response for the corresponding moving rack velocity for the lower order as labeled in Fig. 7 and Fig. 8, is quite similar to that of the original system of higher order therefore it can be verified that the reduced first-order model is accurate. The positive and reverse characteristics for the control motor through torque are responsible for reciprocating the moving rack to its position of re-entry. Hence validity of accuracy of the simplification for the complexity of system is prove.

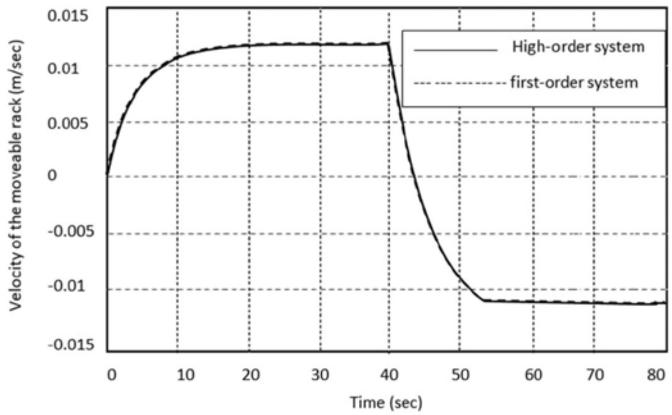

Figure 9: The moving rack's velocity response of first and higher order system with input of motor torque as unit step

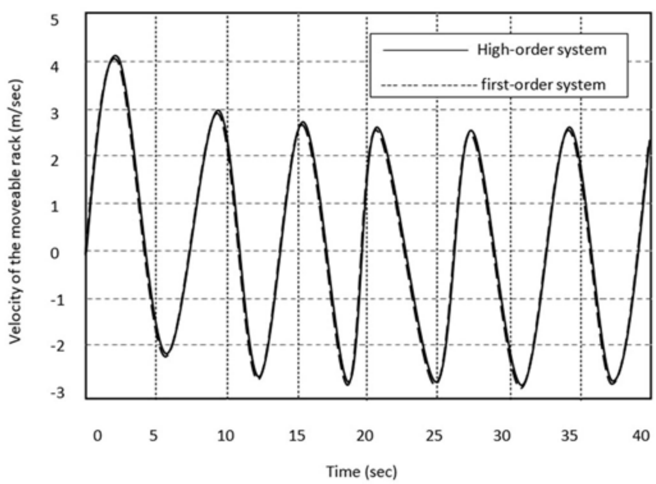

Figure 10: The movable rack's velocity response of first and higher order system with input of motor torque as unit step M(t) = sin t

6.6 Simulation with Controller for Original Linear System having Higher-order along with First-order System

Response of the moving rack velocity of the system is controlled through PI controller. To prevent error in the steady state caused by the transient reaction of the system and to reach to the steady state, design should conform to requirements major poles of closed-loop and the over damping ratio must be kept constant for $\zeta = 1.36$ with natural frequency $\omega n = 0.6$ radian per second.

The major closed loop poles of the reduced first-order system are $-0.816 \pm i\ 0.553$. These conditions of the poles are substituted for obtaining the gain parameters for the PI controller which come out to be of KP and KI = 496. 95. Same is depicted by Fig. 11, stable velocity response of the moveable rack can be kept stable, if the input is controlled at the moment of unit step. The significance of this response is that it is over damped having no steady state error, conforming to the expectations. With the application of the approximation criterion for reduction of a higher order system, resulting first order system which can be used for designing of controller, the response of the output is same as that of the original system of higher order. Hence, accuracy and ease of the designed control scheme is proven. In practical situations, such characteristics of input velocity for moving rack are typically applicable, as in case of the movement of moving rack from any position to another position throughout operating cycle. The three stages of cross-lapper system motion is shown by the diagrams i.e. start up, steady state motion and the reverse stage.

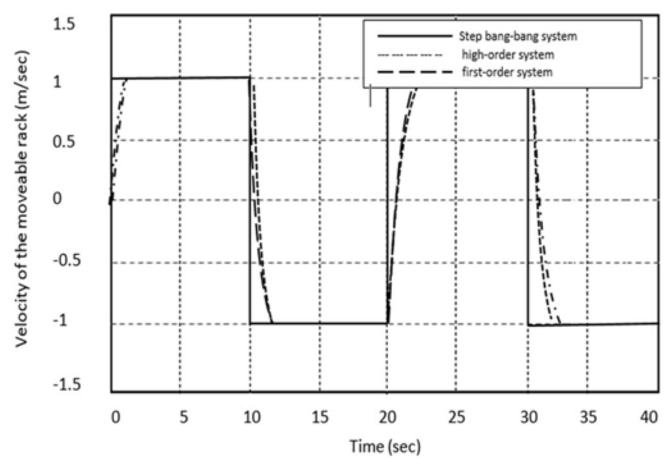

Figure 11: The response of velocity for moving rack for first and higher order system for unit step input as motor torque with PI controller

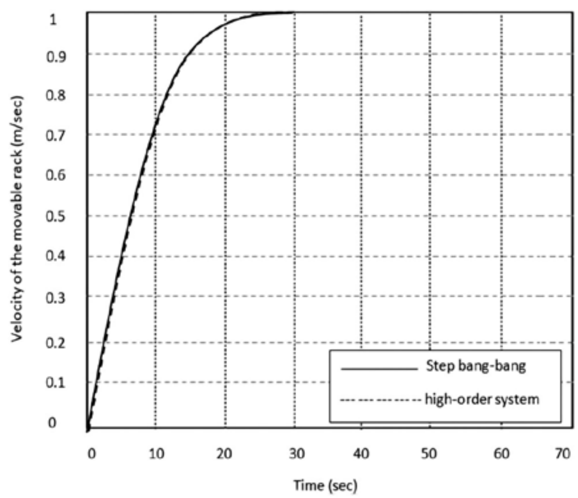

Figure 12: The movable rack's velocity response for higher order system for unit step input as motor torque with state feedback control

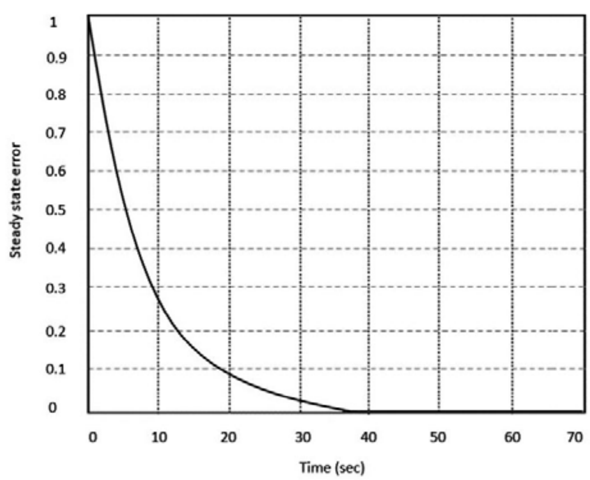

Figure 13: The movable rack's velocity response for high-order system model for unit step input as motor torque with state feedback control

During the start-up stage, the velocities of movement of movable rack is constant. While direction of the drive changes at the commencement of the reverse stage. In the reciprocating motion, it is proved that a good trajectory tracking property as well as the elimination of steady-state errors are achieved by the designed controller. The movable rack possess a smooth steady velocity, therefore it has the major contribution towards achieving the web uniformity and for sustaining the machine's operational life.

7. CONCLUSIONS

The new horizontal cross lapper machine plays a very important function in the unconventional production procedure. The density and the width of the web, as needed for the product, depend on the fast and stable speed control of the mobile storage. Conversations related to the current horizontal cross lapper are not uncommon in the study. Therefore, this paper offers a model and deliberates on the optimal alignment of the current horizontal machine system of the cross-lapper machine type. The lower order system of control design is achieved on the condition of authorization, and the accuracy of the system is guaranteed. Both coordinated as well as co-operative governance, along with the formulation of political inclusion in response to the state,are used in the construction of the system for effective control. The controls can result in a solid speed for the moving rack with precise tracking points and can remove fixed position errors. This constant velocity of the moving rack would therefore create some web similarity and support the machine's life. Meanwhile, the cross lapper may also be operated by using microprocessors. Such a control mechanism may be utilized to meet the requirements of web card engineering, reduce the vibrations of the machine, and reduce power overload.

REFERENCES

1) Kuo,C.F.J.andChiang,W.,DynamicControlof aCross Lapper,TextileRes.J.,73,64–68(2003).

2) Stadnik, J., Model for the Optimal Control of the Cross Lapper Drive, J. Textile Mach. Soc.Jap.(EnglishEd.),44(4),69–73(1998).

3) Kuo,C.F.J.andTasi,C.C.,OverallStrategyforFabricFoldingMachineSystemControl,Int. J. Adv. Manuf. Technol., 31, 1198–1208(2007).

4) M.Miao,H.E.Glassey,andM.Rastogi,Text.Res.J.,74(6),485(2004).

5) D.H.MuellerandA.Krobjilowski,J. Ind.Text.,33(10),111(2003).

6) H.Rongand G.S.Bhat,J.Appl. Polym.Sci.,91,3148 (2004).

7) A.Marciniak,D.Gregulec,J,Kaczmarek:Numericalprocedures,Nakom,Poznan1992.

8) ControlSystemEngineering,NormanS.Nise,7thedition.

9) Production Machining. Gardner Publications. Archived from the original (PDF) on 2012-04-25.

10) Mark Irvin, Engis Corporation (February 2011). "Diamond Lapping and Lapping Plate Control" (PDF).

11) English,R.E.(1953)."OpticalFlats".InIngalls,AlbertG.(ed.).AmateurTelescope Making, Book Three.Scientific American. pp.156–162.

12) https://www.electrical4u.com/steady-state-error-analysis/

13) https://www.electronics-tutorials.ws/systems/open-loop-system.html

14) www.khanacademy.org

15) https://www.researchgate.net/publication/318107848_Force_and_torque_of_a_string_on_a_pulley

16) www.baumueller.com

17) https://www.smadent.com/11th-class/physics-textbook.html

18) ocw.mit.edu

19) ModernControlEngineering5thEdOgata2010

20) https://www.wikipedia.org/

21) Chung-FengJeffreyKuo,Cheng-ChihTsai1andHung-MinTu,CarriageSpeedControlofa Cross-lapperSystemforNonwovenWebQuality

22) Chen,P.T.,Flat-bed Cross-LapperMachine, Tayou Machinery Co.Ltd.,Tayou, Taiwan,2009

23) Rao,S.S., Mechanical Vibrations,PrenticeHallInc.,2005.

24) Kelly, S. G., Fundamentals of Mechanical Vibrations, McGraw Hill Inc.,NewYork,1993.

25) Chang, B. C. and Yousuff, A., Pole Placement andthe Observer BasedControllerParameterization,IEEETrans. Auto.Control,35(6),726–729,(1990).

26) Emre, E andKhargonekar, P., Pole Placement for Linear Systems OverBezoutDomains, IEEETrans. Auto. Control,29(1),90–91,(1984).

KARACHI INSTITUTE OF ECONOMICS AND TECHNOLOGY

Main Campus, PAF Airmen Academy, Korangi Creek

Tel: 021-35091114 - 7 | Cell: 0345-4982304-7

Designed & Produced by HAWK